Sediment routing systems of the Eocene Tremp-Jaca basin

Stratigraphic analysis and numerical models

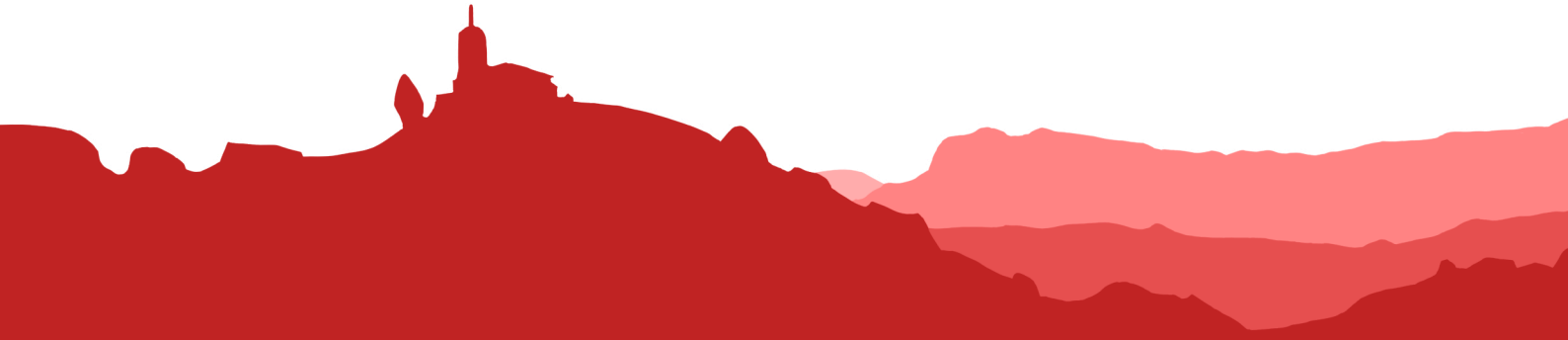

Andreu Vinyoles Busquets

Universitat de Barcelona

Departament de Dinàmica de la Terra i l'Oceà

Sediment routing systems of the Eocene Tremp-Jaca basin:

Stratigraphic analysis and numerical models

Memòria de tesi doctoral presentada per **Andreu Vinyoles i Busquets** per optar al títol de *Doctor en Ciències de la Terra* per la Universitat de Barcelona.

Aquesta tesi que s'inscriu en el programa de doctorat de ciències de la terra de la Universitat de Barcelona ha estat dirigida pels doctors **Miguel López Blanco** i **Miguel Garcés Crespo**.

Andreu Vinyoles i Busquets

Barcelona, Desembre de 2020

Dr. Miguel López Blanco

Dr. Miguel Garcés Crespo

This thesis has been carried out in the *Departament de Dinàmica de la Terra i de l'Oceà* and the *Institut de Recerca Geomodels*. This research was funded by the Spanish project SEROS (CGL2014-55900-P) and the *Ministerio de Economía y Competitividad* (BES-2015-073302). Paleomagnetic measurements were made in the Paleomagnetic Laboratory of Barcelona (CCiTUB-Geo3BCN-CSIC).

Cover illustration: Ainsa basin skyline from *Barranco de la Solana*. Ovidi Pairet Paulet.

Digital supplementary data of this thesis can be found on the CD accompanying the printed version or can be asked to the author on andreu_vinyoles@hotmail.com

Contents

A l'Avipà i a totes les altres persones
que han despertat la meva curiositat

Abstract

The Eocene South-Pyrenean foreland basin provides a continuum of outcrops representing a Source to Sink sediment routing system from subaerial canyons to deep marine environments. On this context, the specific objective of this study is: (a) to contribute to the knowledge of the chronostratigraphy and the basin infill of the study area; (b) to analyze the evolution of the sedimentation rates on the Tremp-Jaca basin; and (c) to generate numerical models to (i) assess the sediment routing and sediment balance and, (ii) to evaluate the basin response to the propagation of climatic and tectonic signals.

Two new magnetostratigraphic sections are built on the Tremp-Jaca basin; the Olsón (Ainsa basin) and the Yebra de Basa sections (Jaca basin). The Olsón section provides a late Lutetian to early Priabonian age for the Escanilla formation in the Ainsa basin, and the same age range is provided on the Yebra de Basa section for the strata encompassed between the Sabiñánigo sandstone and the Santa Orosia formation.

The age constrains provided by these new sections and the data sorted from a systematic review of the literature have been used for an analysis of the sedimentation rates in the Tremp-Jaca basin. The studied sections were decompacted by backstripping to correct the differential burial compactions between the sections. This study shows that sedimentation rates may not show the expected variations related to depozone distribution. This lack of correlation between the depozones and the sedimentation rates are consequence of the lagged response to deformation front shifts and the complexity in the structure of the wedge-top. This complexity result in a widespread subsidence related to the emplacement of basement units in the hinterland. Also underfilled forelands may develop high sedimentation rates in the initial stages of wedge-top as basin gradients are a continuation to those developed in the previous foredeep phase. Sedimentation rates in overfilled areas are controlled by accommodation. In underfilled areas, the main control is clastic supply. During graded shelf regressive stages, maximum sedimentation rates are in foreset areas. In the transgressive stages, maximum sedimentation rates are at the topset. In out-of-grade periods, high sedimentation rates are in deep marine areas.

The results obtained above have been used to feed forward stratigraphic models, using Dionisos software, to test and understand the different parameters affecting the sedimentary infill of the basin. A first model on the sediment routing systems of the Tremp-Jaca basin, based on the data from the sedimentation rates analysis, succeeds

on reproducing the sedimentary routes that can be deduced from the paleocurrent patterns on the Tremp-Jaca basin, validating the inputted data. A second forward stratigraphic model, based on architectural and cyclostratigraphic analysis from previous works, determines that the high-frequency Milankovitch cyclicity of the Belsué-Atarés delta (Sierras Exteriores) is primarily forced from the sediment supply and secondary from the eustasy.

Resum (Català)

A les conques Eocenes Sudpirenaiques d'avantpaís hi ha un continu d'afloraments representatius de les rutes sedimentàries del sistema *Source to Sink*, des de canons subaeris fins a ambients marins profunds. En aquest context, aquest estudi té com a objectiu (a) contribuir al coneixement de la cronoestratigrafia i el reompliment de les conques de l'àrea d'estudi; (b) analitzar l'evolució de les taxes de sedimentació a la conca de Tremp-Jaca; i (c) generar models numèrics per (i) avaluar les rutes sedimentàries i el balanç sedimentari i (ii) avaluar la resposta de la conca a la propagació de senyals climàtics i tectònics.

S'han construït dues noves seccions magnetostratigràfiques a la conca de Tremp-Jaca; les seccions d'Olsón (conca d'Aïnsa) i de Yebra de Basa (conca de Jaca). La secció d'Olsón proporciona una edat Luteciana superior fins a Priaboniana inferior per a la part superior de la formació Escanilla a la conca d'Aïnsa. A la secció de Yebra de Basa s'obté la mateixa franja d'edat pels estrats entre el gres de Sabiñánigo i la formació de Santa Orosia .

Les edats proporcionades per aquestes noves seccions i les dades obtingudes a partir d'una revisió sistemàtica de les dades publicades, s'han utilitzat per a una anàlisi de les taxes de sedimentació de la conca de Tremp-Jaca. Les seccions estudiades han estat descompactades per *backstripping* per corregir l'enterrament diferencial que resulta en estadis de compactació diferents entre les seccions estudiades. Aquest estudi mostra que les taxes sedimentaries poden no mostrar les variacions esperades en relació a la distribució de les depozones. Aquesta manca de correlació entre les depozones i les taxes de sedimentació són conseqüència del retard en la resposta als canvis en la posició del front de deformació al *wedge-top.* Aquesta complexitat resulta en l'expansió de la subsidència relacionada amb l'emplaçament d'unitats basals al *hinterland*. Aquesta complexitat resulta en una major subsidència relacionada amb l'apilament d'unitats basalts al *hinterland*. També les conques d'avantpaís *underfilled* poden desenvolupar altes taxes de sedimentació en els estadis inicials del *wedge-top,* ja que els gradients sedimentaris són la continuació dels desenvolupats a la fase de *foredeep* anterior. Les taxes de sedimentació a les àrees *overfilled* estan controlades per l'acomodació. A les àrees *underfilled,* el control principal és l'aport de sediments. Durant els episodis regressius de les plataformes gradades, les taxes de sedimentació màximes es donen al *topset*. En els períodes no-gradats, les taxes de sedimentació més elevades es troben a les àrees marines profundes.

Els resultats obtinguts s'han utilitzat per alimentar dos *forward stratigraphic models*, utilitzant el software Dionisos, per provar i entendre els diferents paràmetres que defineixen el reompliment de la conca. Un primer model en els sistemes de rutes sedimentàries de la conca de Tremp-Jaca, basat en les dades provinents de l'anàlisi de les taxes de sedimentació, té èxit en reproduir les rutes sedimentàries que es poden deduir dels paleocorrents de la conca de Tremp-Jaca, validant les dades introduïdes. Un segon model, a partir de dades arquitecturals i cicloestratigràfiques de treballs previs, determina que les ciclicitats de Milankovitch d'alta freqüència del delta de Belsué-Atarés (Sierras Exteriores) són primàriament forçats per l'aport sedimentari i secundàriament per l'eustàcia.

Acknowledgements

Una tesi doctoral és un treball en equip que firma una sola persona. Aquí va un petit reconeixement a aquest equip sense el qual aquesta tesi mai hauria pogut arribar a bon port.

Muchas gracias **Miguel López Blanco** por dirigirme, tutorizarme y estar siempre para lo que haga falta. Agradezco mucho haberte tenido de profesor particular de estratigrafía siempre que he necesitado una clase, así como toda la ayuda en los demás aspectos de la tesis. También agradezco que tus correcciones me hayan servido para mejorar científicamente y personalmente. Y agradezco haberte podido tener a "mi lado" virtual durante esos últimos meses, cuando más apoyo he necesitado.

Moltes gracies **Miguel Garcés** per totes les hores compartides al camp, al despatx, al laboratori, a congressos... Amb tu no només he après un munt de geologia, sinó que també he après a moure'm per la jungla de la ciència, des de la recollida de mostres al camp fins als aspectes més avorrits de la gestió.

Muitas gracias **Pau Arbués** pa totas las horas compartidas a lo campo fendo columnas y estudiant la cheolochía d'Aragón. He après molt de tu. He après a trepitjar el terreny que estudio i a estimar-lo. I a més, moltes gràcies per descobrir-me llocs a on estar com si fos a casa sense ser-hi, per la profunditat fins a on pot arribar una conversa amb tu i per descobrir-me la cultura d'Aragó.

Lluis Valero, moltes gràcies per estar al meu costat en tot l'espectre de la tesi, des del punt més estrictament científic fins al punt més estrictament festiu. Les teves empentes m'han ajudat a avançar des del primer fins l'últim dia, sobretot en els moments en els que he estat més baix d'ànims. Molta part de les idees d'aquesta tesi parteixen de parlar amb tu.

Gràcies **Bet Beamud** per tota la companyia i converses al camp, per l'ajuda al laboratori i per aportar bons consells respecte al Pmag i a la ciència en general.

Sébastien Castelltort, ta gentillesse a fait de Geneve une seconde maison pour moi. Merci beaucoup pour les heures passées à discuter de la science derrière la modélisation numérique, du changement climatique et des Pyrénées en général. Merci également pour avoir créé un si bel environnement scientifique au sein du département.

Josep Ma Parés, moltes gràcies per la teva acollida a Burgos, pels passejos per la ciutat, les classes de magnetisme de roques i els bons sopars després de perforar per Olsón.

A més també vull agrair a totes les companyes i treballadores del departament haver-me facilitat la feina en tot el que han pogut. En especial a l'**Alberto Sáez**, coordinador del programa de doctorat de ciències de la terra, per la seva eficiència en les gestions i per sempre estar tan disponible per resoldre qualsevol dubte que plantegi la burocràcia doctoral.

Especialment vull agrair a la gent que han compartit en algun moment amb mi la sala 336, pels cafès, dinars i les converses de sala, en especial al **Rubén** i al **Rayo** que ja no hi treballen i als que van viure-hi els últims mesos que hi vaig estar **Andrea**, **Edu**, **Maria**, **María**, **Helena** i **Sergi**. També vull agrair a la **Judit**, la **Mercè**, el **Marc** i a la gent de

marina en general el que m'hagin adoptat als seus sopars i festes durant tots aquests anys que hem estat convivint.

Merci beaucoup à nos collègues de Genève (**Louis**, **Simon**, **Abdallah**, **Stephen** et **Nikhil**). Vous avez rendu mon séjour très agréable et profitable. I també moltes gràcies **Sabí**, per les sortides boletaires, les excursions al Salève i pels sopars de pizza amb nestea.

I no tota la gent a qui li estic agraïda estan tan vinculats a la geologia, encara que coneguin bé el Buntsandstein. Vull reconèixer el recolzament que m'han donat els meus amics **Ovidi**, **Joan**, **Víctor**, **Guillem** i **Marc** durant els anys que ha durat la tesi, els anys anteriors a la tesi i, espero, els anys que han de venir. Espero poder-vos ajudar als vostres projectes personals tot el que vosaltres heu ajudat al meu.

Amanda, muito obrigado pela vossa paciência, companhia e pela vossa deliciosa comida, estes dias de trabalho intensivo têm sido um pouco mais bonitos graças a si. Obrigado, **Paul**, pela sua linda companhia. **Majo** y **Luisa**, muchas gracias por parchearme, las sesiones de coworking y reír mis chistes, incluso cuando son malos. También te estoy muy agradecido, **Sara**. Me sentí muy arropado por ti en esos meses de estrés y confinamiento; de combinar tortillas de patata con ejercicio; y de escuchar carnaval y a **Oreo** maullar. I també agrair-li a la **Kai** i a l'**Uri** aguantar-me casi des del principi del recorregut i durant pràcticament tota la tesi sencera. Conviure amb vosaltres ha fet les coses molt més fàcils.

Moltes gràcies també a la **Laura**, l'**Ovidi**, la **Laia** i la **Núria** per tot el suport emocional que m'heu donat a aquest tram final de la tesi i durant tot el llarg camí que m'ha dut fins a acabar-la. I també gràcies per ficar les mans en alguna part i ajudar-me a millorar-ne la llegibilitat, alguna figura o la portada.

I finalment vull agrair a la meva família totes les hores que han dedicat a que pogués estar una mica millor per fer aquesta tesi. Moltes gràcies pels mems **Martí**, moltes gràcies per animar-me **Mama**, moltes gràcies pels bons consells **Papa**, moltes gràcies per acollir-me a Mont-roig **Aviamia** i moltes gràcies pels berenars a casa teva **Iaia**. La vostra il·lusió en tot el que feia i explicava i el vostre amor m'han ajudat a tirar endavant amb més força.

Moltes gràcies a tot l'equip! Aquesta tesi també és vostra. Al final ens ha costat una mica més del que havíem previst d'entrada, però amb perseverança al final ens n'hem sortit.

No hi ha pany si és prou l'afany. Roger Mas

1 INTRODUCTION

The Thesis "Sediment Routing Systems: Stratigraphic analysis and models" faces the problem of how the variations in time and space of the tectonic and climatic conditions affect the sediment distribution and its routing systems. To assess this problem, the present research includes a combination of techniques including stratigraphic analysis (*e.g.* field work), magnetostratigraphy and stratigraphic forward modeling using Dionisos. These have been applied to case-studies from the Eocene South-Pyrenean basin since it provides a continuum of outcrops representing a foreland basin system Source to Sink sediment routing system from subaerial canyons to deep marine environments persistent for a long enough time lapse to develop stratigraphic analyses at different space and time scales. Therefore, the main goals of this thesis are (a) contribute to the knowledge of chronostratigraphy and the basin infilling in the study area; (b) study the evolution of the sedimentation rates on the Tremp-Jaca basin; and (c) to generate numerical models to (i) assess the sediment routing and balance and (ii) to evaluate the basin response to the propagation of climatic and tectonic signals.

Thus, the results of this thesis are structured in three main blocks: the ones related to magnetostratigraphic analysis and correlation, the 4D sedimentation rates analysis, and the Forward stratigraphic modeling including both the Belsué syncline and the western South-Pyrenean foreland basin models.

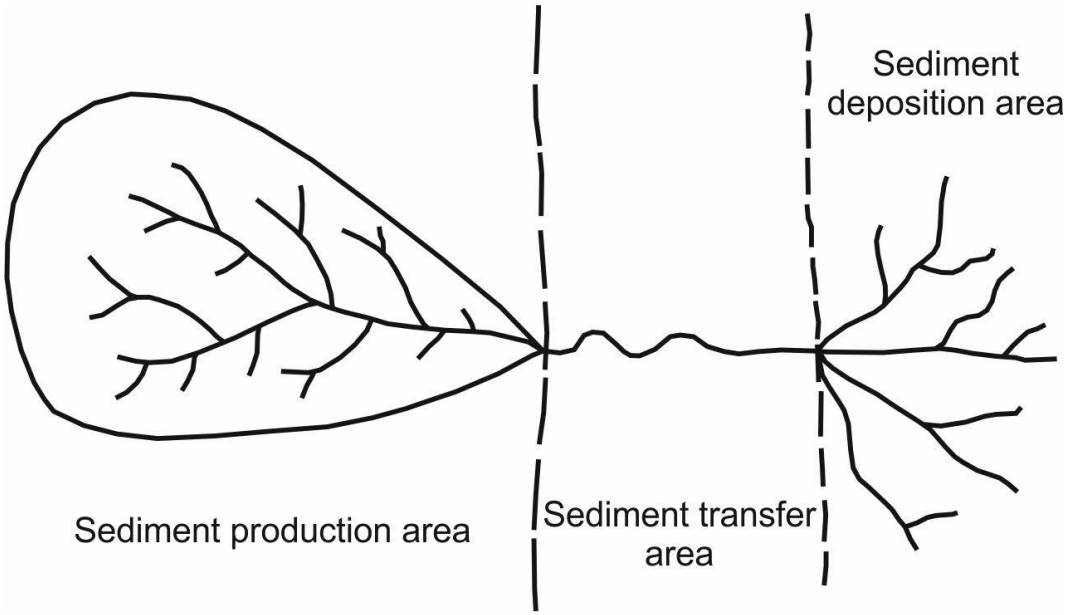

Figure 1.1: Divisions of a basin in Schumm, (1977). The basin into an area dominated by erosion, an area dominated by transport and an area dominated by sedimentation.

1.1 Basin analysis; source-to-sink analysis and sedimentation rates on the foreland basins

1.1.1 Source-to-sink analysis

Source-to-sink systems analysis involves a complete, earth systems model approach from the ultimate onshore drainage point to the toe of related active deepwater sedimentary systems (Martinsen *et al*., 2010). The concept source-to-sink appears on the 2000s, but these have been studied since before. The first relevant reference on the comprehension of the full basin was made by Schumm (1977). There, the basin is divided into three depositional areas: the sediment production area, the sediment transfer area and the sediment deposition area (figure 1.1). But unless the study of the source-to-sink systems started 50 years ago, recently it has grown the interest on studying this topic. Sømme *et al*. (2009), makes a classification of the different parts of a source-to-sink system into geomorphic segments. Those segments are the catchment, the shelf, the slope and the basin floor (figure 1.2). This division assigns different geomorphologic properties to each basin segment, instead of being based only on the erosion/sedimentation proportion. So, this division is useful to make predictions. Until now, many of the studies on the source-to-sink systems has been done in passive margin

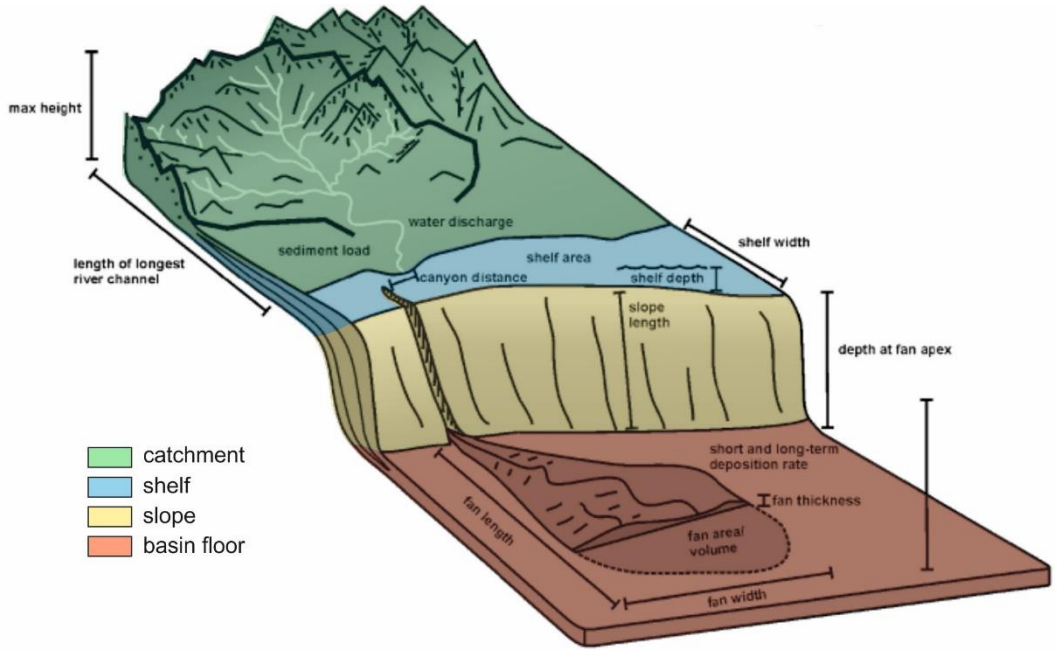

Figure 1.2: Sømme *et al*. (2009) names the parts of the basin in function of the geomorphic segments. Those segments are the catchment, the shelf, the slope, and the basin floor. Those divisions are originally applied in a passive margin, but they can also refer to a foreland basin. Figure modified from Sømme *et al*. (2009).

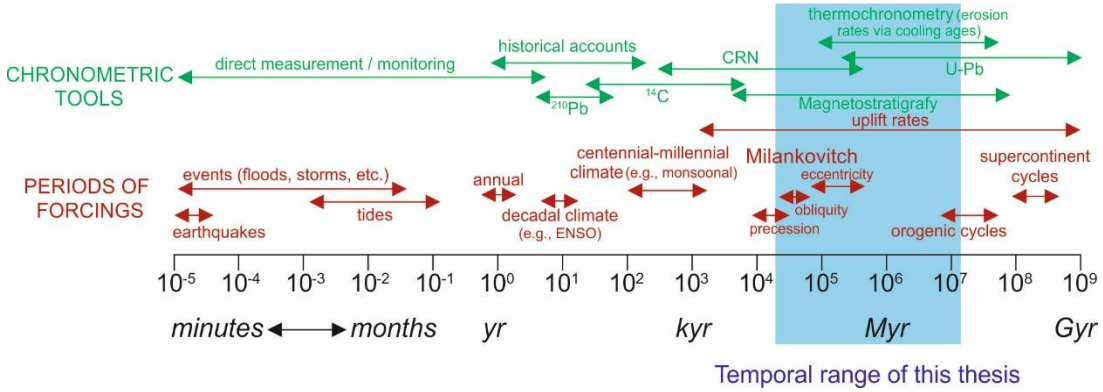

Figure 1.3: Diagram representing the different sedimentary signal action scales, with their equilibrium times. For the ages that can be studied with magnetostratigraphy, see that they are mainly the uplift rates, the Milankovitch cycles, and the orogenic cycles (Romans *et al*., 2016).

settings. But those studies can be easily extrapolated into other regions, such as a foreland basin (Martinsen *et al*., 2010).

Sediment can be catch in all the geomorphologic segments described in Sømme *et al*. (2009). This is because sediment and solutes can be temporally stored during transport (Carvajal and Steel, 2012), affecting the sediment final distribution. So, to understand all the source-to-sink system is necessary to consider the sediment and solutes temporal storages that can blur the sedimentary signal.

There are three different approaches on the source-to-sink study: the full system analysis, the numerical/experimental modelling and the segment analysis. For the ancient systems, usually the full system is not preserved because it is partially eroded or even not exposed, so it must be studied on the preserved segments. Those preserved segments allow to make predictions on the non-preserved areas thanks to knowing how modern systems work and to the uniformitarian principle. Moreover, on ancient systems studies the numerical and analogical simulations to predict the conditions of the unknown areas are also common.

The sedimentary signal on a source-to-sink system that can be studied depends on the temporal scale that we are dealing with. Romans *et al*. (2016) proposes a summary of how the signals can be transmitted in different temporal scales and at which time scale can be registered on the sedimentation, so conditioning the sediment balance in a source-to-sink system. In the time span studied on this thesis, it is expected to found Milankovitch cyclicity, uplift rates and orogenic cycles (figure 1.3) since the studied time span is about 10Myr and magnetostratigraphy gives a resolution sometimes close to 0.1 Myr.

The studied portion of the South-Pyrenean Foreland Basin represents a partial view of a Source to Sink system but includes most of the subdivisions by Schumm (1977) and Sømme *et al*. (2009), just excluding the areas where most of the sediment was produced (catchment area).

1.1.2 Sedimentation rates in foreland basins (from Vinyoles *et al*., 2020)

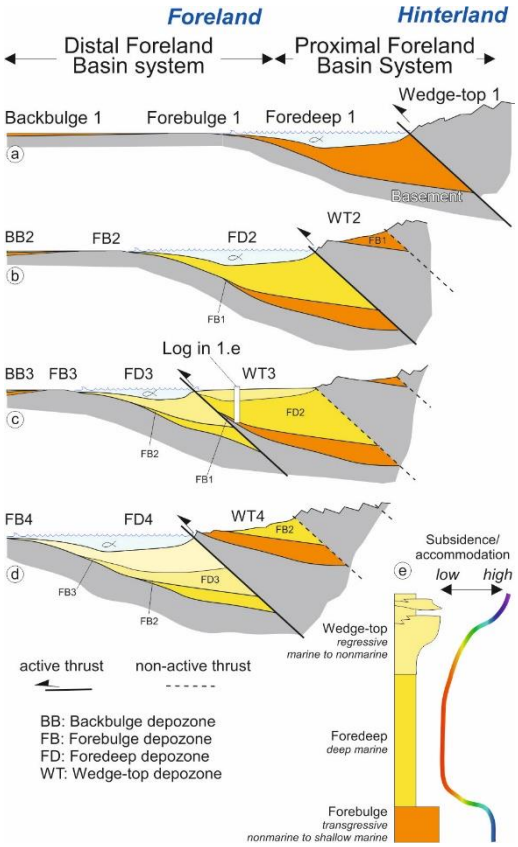

Figure 1.4: Evolution of a Foreland basin system controlled by a piggy-back foreland-directed thrust sequence with the location of Proximal and Distal Foreland Basin Systems, Wedge-top, Foredeep, Forebulge and Backbulge depozones. (a) Initial stage with a foredeep depozone located on the footwall of the active thrust. (b) A second thrust produces a displacement of the subsidence towards the foreland and migration of the forebulge. The original forebulge (FB1) is now buried below the second foredeep depozone associated with the second thrust. (c) Initial movement of a third thrust produces a forelandward displacement of subsidence and migration of the forebulge. Original forebulge (FB1) is now incorporated into the hanging wall of the thrust, while the foredeep sediments associated with the second thrust (FB2) are buried below the wedge-top depozone (piggy-back basin) sediments. (d) Final movement of a third thrust produces foreland displacement of subsidence and migration of the forebulge. Original forebulge (FB1), incorporated into the hanging wall of the thrust suffers from denudation as it becomes part of the uplifted source area. (e) Ideal log showing the vertical superposition of depozones as deformation advances to the foreland as well as sedimentary and accommodation trends. See its representative location in frame (c). Vinyoles *et al*. (2020)

The study of sedimentation rates variations in time and space across a basin give an idea of how the Sediment Routing system developed and a set of numerical values needed to develop the Forward Stratigraphic Models. This kind of analysis will help us to understand the basin dynamics and evolution.

Foreland basin systems can be divided in different tectono-depositional areas (DeCelles and Giles, 1996) depending on their location relative to the main deformation front. These are: 1) the wedge-top depozone, or the thrust-top and piggy-back basins on top of the orogenic wedge; 2) the foredeep depozone, in between the orogenic wedge and the proximal flank of the forebulge; 3) the forebulge depozone, between the foredeep and back-bulge; and 4) the back-bulge, cratonward of the forebulge (figure 1.4).

Many foreland basins develop piggy-back basin sequences, carried by thrust and faults, as a product of forward (*i.e.*, towards the foreland) thrust propagation. This results in a migration of the depocenters and depozones towards the foreland (figure 1.4). When the primary foredeep depozone is incorporated into the wedge-top depozone, it becomes a zone of sediment bypass, and eventually may become the source area for the new adjacent foredeep (Bally, 1984; Cant and Stockmal, 1989; Miall, 1995; DeCelles and Giles, 1996). Similarly, the forebulge and backbulge depozones are progressively incorporated into the foredeep as the basin migrates towards the foreland increasing accommodation space and the resulting infill of clastic sediments. Accordingly, the expected evolution of sedimentation rates at a fixed location would be: (1) An initial progressive increase while the former distal foreland region (backbulge, forebulge and distal foredeep) is incorporated in the proximal foredeep depozone, and (2) a decrease in sedimentation rates when it is finally incorporated into a thrust-top basin in the wedge-top depozone, finally becoming part of the source area (figure 1.4e) (Homewood *et al*., 1986; DeCelles and Giles, 1996). However, this documented sedimentation rates trend in foreland basins may be far more complex, depending on the tectonic evolution and structural control of the wedge-top basins and variability in sediment flux. The structural style of the hinterland may influence different uplift and denudation scenarios, which control both the amount of sediment supply, and the load-related regional flexural subsidence (DeCelles and Giles, 1996; Romans *et al*., 2016). In addition, the emplacement of thrust sheets in the foreland may promote uplift associated with in-sequence thrusts as the former foredeep is incorporated into the wedge-top depozone and drive local accommodation variations alongside the growth of topographic barriers and traps for clastic sediments. Further differences may arise due to the inherited 3D geometry of the foreland basin, and the relative timing of growing structures. Finally, a sediment supply increase may result in a higher sediment load on the basin triggering higher subsidence rates.

Previous works on sedimentation rates for foreland basin settings give average values of 10 to >100 cm/kyr (Einsele, 2000). However, very high values—such as 238 cm/kyr (Maesano and D'Ambrogi, 2015)—have been calculated for the Pleistocene of the Po basin, in the same range that the 270 cm/kyr obtained from the numerical models for the Eocene of the Western Alps (Erdos, *et al*., 2019).

1.1.3 South-Pyrenean foreland: basins and tectonic units (from Vinyoles *et al*., 2020)

This work is based in a series of case-studies from the Eocene South-Pyrenean foreland basin. This area has been chosen because it has been studied since many years as it is an excellent natural laboratory where are exposed the different areas of a foreland basin and its Sediment Routing system. Also, there is a very complete magnetostratigraphic dating of different sections through the whole basin, that allows the study of 4D distribution of sedimentation rates across the source to sink system of the Tremp-Jaca basins (Vinyoles *et al*., 2020), a first step to the stratigraphic forward model of the Source to Sink system and to understand the influence of tectonic and climatic controls at short term frequency through the forward model of the Eocene sediments of the Belsué syncline in southern Jaca basin.

The Tremp-Jaca basin (TJB) represents the central and western part of the South-Pyrenean foreland which evolved from late Cretaceous to Miocene times in response to flexural subsidence related to the growth of the Pyrenees (Zoetemeijer *et al*., 1990). Modern TJB configuration was created by the interaction of several thrusts detached at

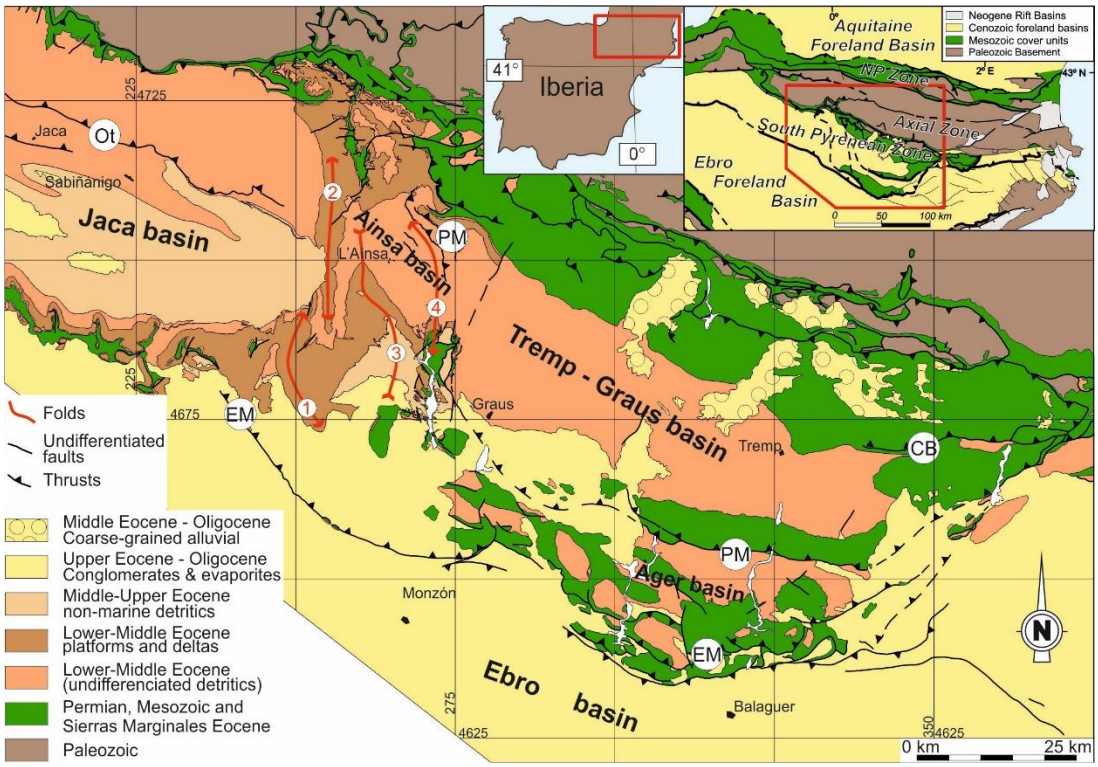

Figure 1.5: Geological map with the location of the main structures, basins. Thrust Sheets: CB: Cotiella-Boixols; PM: Peña Montañesa-Montsec; EM: Sierras Exteriores-Serres Marginals. Thrust: Ot: Oturia thrust. Folds: 1: Balzes; 2: Boltaña; 3: Buil 4: Mediano. This map was modified from the compilation made by Fernández-Bellón (2004) from published 1:50,000, 1:100,000 and 1:200,000 scale maps, and Muñoz *et al*. (2018).

the evaporitic upper Triassic Keuper facies. Three major thrust sheets constitute the South-Pyrenean fold and thrust belt in its central part. From north to south and in order of emplacement they are: The Cotiella-Bóixols, Peña Montañesa-Montsec, and Sierras Exteriores-Gavarnie-Serres Marginals thrust sheets (Figures 1.5 and 1.6), which were emplaced during late Cretaceous, late Paleocene-Ypresian (60.0 to 47.8 Ma) and Lutetian-Oligocene (47.8 to 23.0 Ma) times, respectively. The southward displacement of these thrust sheets was triggered by basement thrusts in the Axial Zone (Seguret, 1972; Cámara and Klimowitz, 1985; Beaumont *et al*. 2000). The distribution of the Keuper evaporitic facies influenced the thrust motion, producing differential displacement which resulted in the Ainsa Oblique Zone (AOZ) (Muñoz *et al*., 2013). The AOZ is characterized by a set of kilometer scale N-S trending folds and thrusts (*e.g.*, Mediano, Olsón, Boltaña and Añisclo anticlines, figures 1.5 and 1.6), originally developed perpendicular to the maximum shortening direction during Lutetian and Bartonian. Their present-day oblique orientation is the result of clockwise vertical-axis rotations (70° to 55°) developed in response to a divergent thrust transport direction because the differential displacement and change in structural style from the central to the western Pyrenees (Muñoz *et al*., 2013).

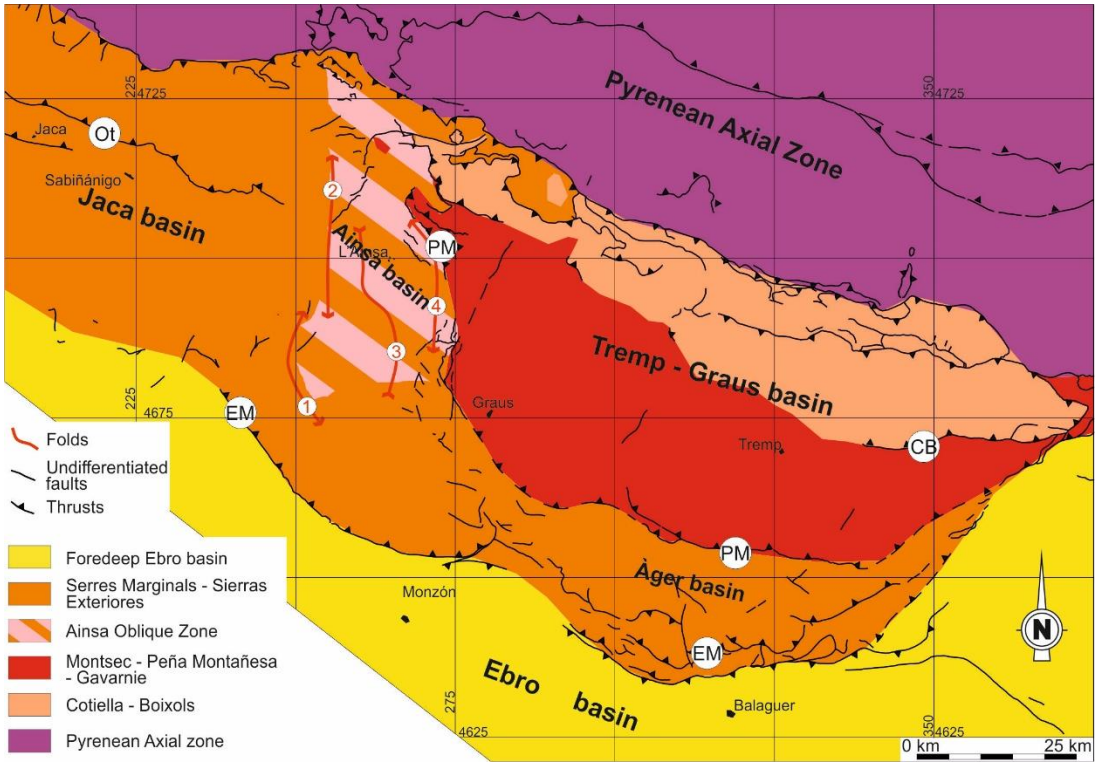

Figure 1.6: Map of the interpreted main tectonic units in the area. The Ainsa Oblique Zone is consequence of the progressive deformation of this area due the differential displacement of the Gavarnie thrust sheet.

The Eocene TJB is an E-W trending ensemble of sub-basins that were bounded by active tectonic structures in specific intervals of the TBJ evolution. The sediments were mostly derived from the inner zone of the axial Pyrenees growing in the north and distributed towards the west into the Atlantic Ocean through an axial drainage system parallel to the chain (Nijman and Nio, 1975; Puigdefàbregas *et al*., 1992; Garcés *et al*., 2020). During early Eocene times, the sediment routing system was divided into two connected sub-basins (figure 1.6); the proximal wedge-top Tremp-Graus basin, on top of the Peña Montañesa-Montsec thrust sheet, and the distal Ainsa-Jaca basin located to the west in the footwall of the Montsec thrust sheet, progressively incorporated on top of the Gavarnie-Sierras Exteriores thrust sheet (Muñoz *et al*., 2013).

During the early Eocene, the wedge-top depozone of the thrust-top Tremp-Graus basin was connected to the west with a foredeep depozone in the Ainsa-Jaca basin. During the middle and late Eocene, the Ainsa basin progressively became part of the wedge-top depozone due to the forward migration of the thrust fronts. The emplacement of the Gavarnie thrust sheet and the growth of the fold and thrust structures of the AOZ from early Lutetian to late Bartonian (47.8 to 37.0 Ma) separated the Ainsa basin to the East from the Jaca-Pamplona basin to the West (figure 1.6) incorporating progressively the AOZ into the wedge-top depozone. This deformation temporally isolated the different depocenters and distorted the paleoflow direction (Dreyer *et al*., 1999; Pickering and Corregidor, 2005; Labourdette, 2011; Moody *et al*., 2012; Muñoz *et al*., 2013; Grasseau, 2016).

1.1.4 Tremp-Jaca basin stratigraphy (from Vinyoles *et al*., 2020)

The studied cases (outcrops) range from Lutetian to Priabonian in age. Thus, this introduction to the stratigraphy of the South-Pyrenean basins will be centered on the middle to late Eocene stratigraphic units relevant for this study (figure 1.7) between Tremp and Jaca meridians (figure 1.5).

The deposition of the sedimentary units during the middle-late Eocene took place in a broadly regressive setting (figure 1.7). Fluvial units were fed from the north and east by coarse-grained alluvial systems with northern provenance (Pyrenean axial zone). Towards the west, the fluvial units grade laterally into transitional detrital units and their prodelta equivalents (figure 1.7). Farther west, the lower part of the succession (Lutetian) grades into deep marine turbiditic systems. Concomitantly, shallow carbonate platforms developed at the southern Jaca and Ainsa basin margin.

Derived from the uplifting **Pyrenean Axial zone** (main catchment area) from east to west, the Pobla de Segur, Gurp, Sis and Santa Orosia coarse-grained alluvial systems

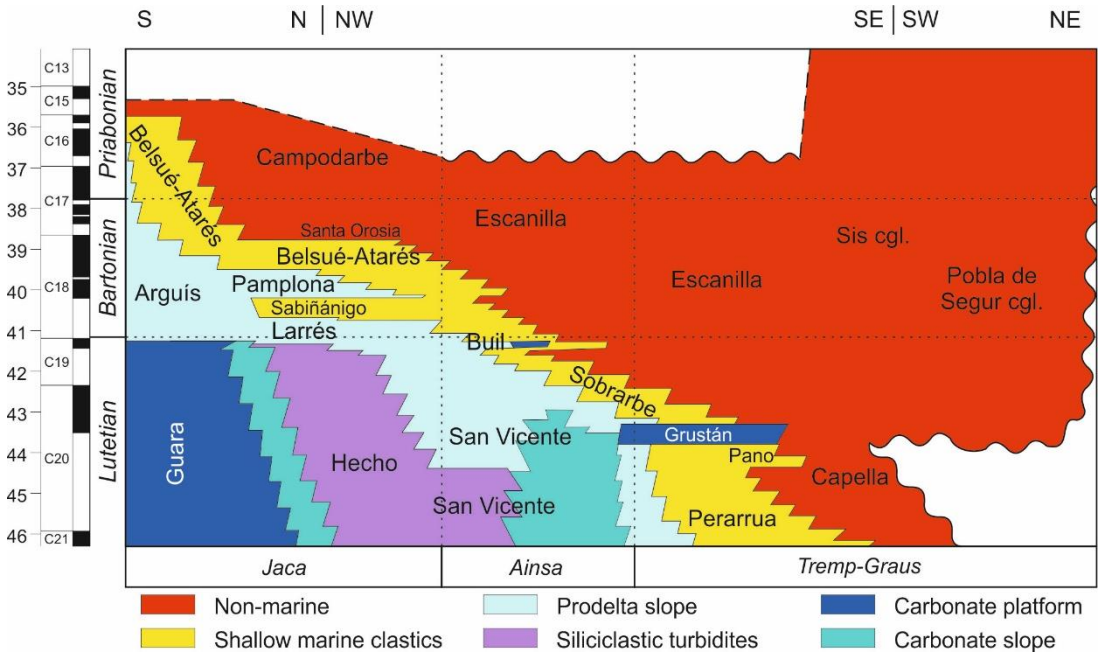

Figure 1.7: Stratigraphic diagram of the Tremp- Jaca basin, with the different stratigraphic units (Vinyoles *et al.*, 2020).

are the most proximal deposits of the basin which evolve distally to distal alluvial and fluvial formations.

Along the axis of the **Tremp-Graus basin**, the middle Eocene sedimentation started with the fluvial Capella formation (Garrido-Mejías, 1968) in the east, grading westwards into the deltaic Perarrúa Formation (Nijman and Nio, 1975). These deltaic units were arranged in a westward regressive trend that was shortly interrupted by a transgressive event represented by the shallow marine Pano Formation (Donselaar and Nio, 1982) and the Grustán Limestone (Garrido-Mejias, 1968). Overlying them, the fluvial Escanilla Formation (Garrido-Mejias, 1968) renewed the long-term regressive trend.

Westwards, the lowermost units of the **Ainsa basin**, correspond to the deposition of the Cuisian to Lutetian (53.0 – 41.2 Ma) San Vicente formation (van Lunsen, 1970), a marly succession that ranges from deep marine turbidite systems to prodelta and carbonate slope facies related to the Guara and Grustán formations. Bathymetry data of the San Vicente Formation suggest upper to mid bathyal depths of 400 to 600 m based in agglutinated foraminifera (Pickering and Corregidor, 2005). However, these isolated data are not applicable to the whole formation since water depths could have varied significantly between sites. Overall, the succession in the Ainsa basin depicts a regressive trend from the carbonate and detrital slope deep-marine San Vicente

Formation, to the shallow-marine deltaic Sobrarbe Formation (de Federico, 1981), and the Lutetian to Priabonian (42 – 37.5 Ma) fluvial Escanilla Formation on top.

The **Jaca basin** forms an E-W trending synclinorium geometry where middle Eocene sediments crop out at both limbs, herein referred to as the Southern and Northern Jaca Basin. Younger (upper Eocene and Oligocene) strata occupy the syncline axis.

The basal units of the Southern Jaca Basin are the carbonate platforms of the Lutetian (47.8 – 41.2 Ma) Guara Formation (Puigdefàbregas, 1975) with estimated paleobathymetry values ranging from 0 to 60 m in the Arguís section (Huyghe *et al*., 2012). Above these platforms, a deltaic sequence with the prodeltaic Arguís marls Formation (Puigdefàbregas, 1975) and the delta front of the Belsué-Atarés Formation (Puigdefàbregas, 1975; Millán *et al*., 1994) were deposited. Vertically, these units are overlain by the non-marine Bartonian to Priabonian (39 - 35 Ma) Campodarbe Group (Soler-Sampere and Puigdefàbregas, 1970).

In the Northern Jaca Basin the Lutetian succession (47.8 – 41.2 Ma) starts with the deep marine turbidites of the Hecho Group (Mutti *et al*., 1972), although the water depth of these sediments remains widely unconstrained. Interpreted as the distal lobe and basin floor equivalents of the Ainsa basin slope deposits (Mutti *et al*., 1985; Mutti, 1992), bathymetries should be as deep as those proposed for Ainsa (400 to 600 m) and, as stated above, is not extrapolable for the whole Hecho Group vertical succession in the Jaca Basin. The basin progressively evolved into the shallower prodeltaic environments of the Bartonian (40.8 -40.2 Ma) Larrés marls Formation (Remacha *et al*., 1987) and the delta front/delta plain environments of the Bartonian (40.2 – 39.9 Ma) Sabiñánigo sandstone Formation (Puigdefàbregas, 1975). A transgressive event occurred at the top of the Sabiñánigo sandstone, returning to deep-sea sedimentation of the Pamplona marls Formation (Mangin, 1959-60), a lateral equivalent of the Arguís marls Formation of the southern Jaca basin. These are overlain by the Bartonian to Priabonian (39.9 – 35.7 Ma) shallow-marine Belsué-Atarés Formation both in the Northern and Southern Jaca Basin. The top of the succession corresponds to the non-marine Santa Orosia fan of the Campodarbe Group (Puigdefàbregas, 1975).

1.2 Numerical modelling background. Models and sedimentology

The geological processes are controlled by many variables that occur during very long periods of time, complicating the understanding of those process. So, to study such processes it is necessary to simplify them into different models that adapt them in a human scale. Those models can be of multiple types, including the conceptual models –

which could be understood as a diagram or a cross-section–, numerical models or analogue models.

The **analogue models** have many years of development since their origin, which began being simple boxes where sand and clay were put to see how they reacted to a compression effort. An example of these primary models is the one done by Henry Cadell (figure 1.8), who used a box to compress sand and clay and compare the observed structures with the folds and thrusts in the nature.

Nowadays, analogue models are much more evolved thanks to the greater knowledge of scalability of the materials, and a major automation. We can do very accurate reproductions of the reality by combining the analogue models with technologies such as photogrammetry or laser scanning. The simulation targets include processes of uplift, erosion, precipitation, thrusting, diapirism, rheology, etc. Analogue models are very

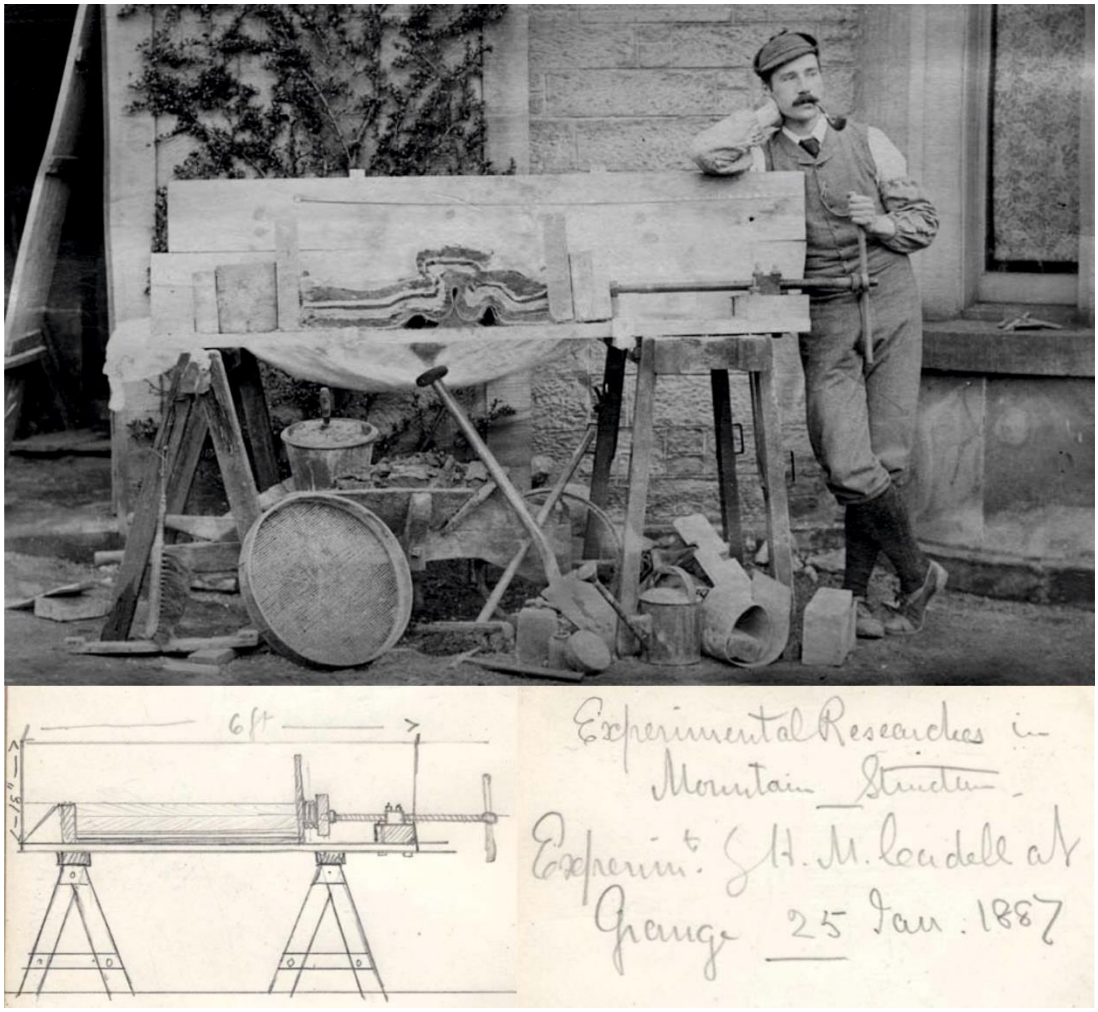

Figure 1.8: One of the first designs of a geological model based in processes photographed. With this apparatus, the geologist Henry Cadell (presumably the man on the photo) tried to understand how are related the compressional stresses with the growing of a mountain in layered rocks (McIntosh, 2009a; McIntosh, 2009b).

interesting because they reproduce the same processes that occur in the nature, but on a temporal and spatial scale that we can study.

On the other hand, **numerical models** are an approach to complex realities through mathematical formulas, bringing with them a series of advantages as they are universal, being able to be reproduced in different places with relatively little infrastructure and achieving identical results. These models are very convenient to use when analyzing the results, as being completely numerical they are easier to analyze statistically or by numerical procedures.

The main drawback of numerical modelling, however, is that there is a significant simplification of reality. The reality is often multiparametric and if we want to make an equation to predict absolutely all the casuistry, we would need to use a 40^{th} order tensor (or even higher). Therefore, constants are used to supplement the effect of multiple parameters with a single value. An example is the erosion value of a rock. Erosionability depends on multiple factors (exposure surface, chemical composition, microfracturing, ambient humidity, vegetation, temperature, weathering, gravitational potential, internal rock structure...). Controlling all these parameters accurately is virtually impossible, which is why in many mathematical models it is simplified into a single value or into a much simpler formula.

The other big problem with numerical models is that they can be designed in such a way that they can represent the most unlikely of scenarios, such as a channel carrying 5 m^3/s of flow and carrying a volume of sediment comparable to erosion three times the sediment of the Brahmaputra basin in 1 Myr. This is because numerical models often need to be calibrated and, depending on how they are calibrated, they can justify aberrant scenarios.

Despite these drawbacks, numerical modeling remains a very powerful tool and with careful calibration has a very interesting prediction ability (see section 5.4.3).

1.2.1 Models classification

Numerical models can be classified according to different parameters. Depending on the results that we want to achieve, we would choose the model that will be used. So models can be classified:

Depending on the **input**: Models can be of the **direct** type if they use a series of principles or processes and apply them in combination to obtain a result. In contrast, models are **inverse** if they are based on a result to obtain the processes that define them (figure 1.9).

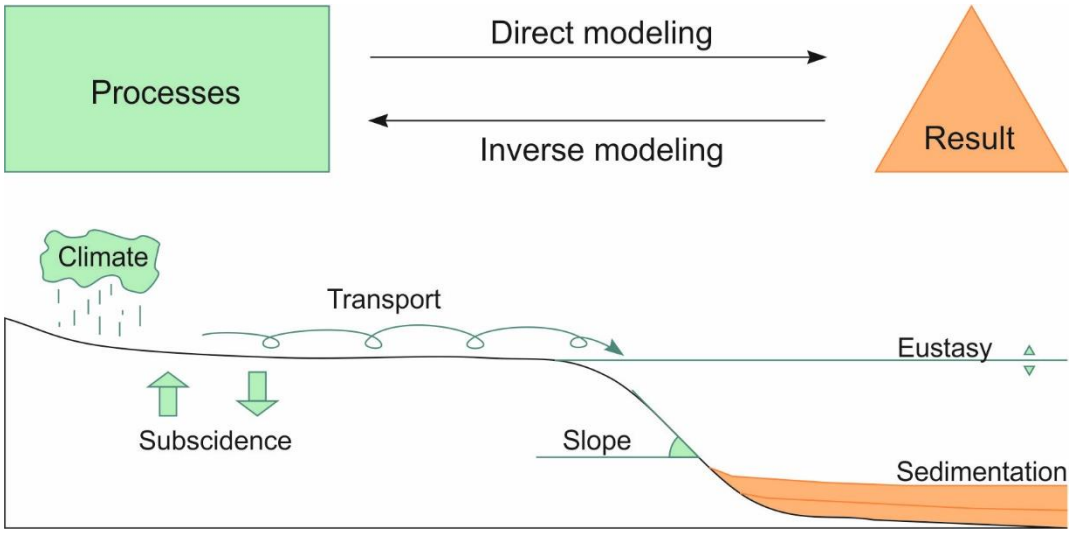

Figure 1.9: Diagram representing the relationship between direct modeling and inverse modeling.

Depending on the **knowledge of the input data**: The models can be **explicit**, if all the data that conform the question are known and its result can be calculated accurately, or **implicit**, if there is any of the data that is unknown and it must also be found out by means of multiple iterations, on the condition that these iterations only result in an exact result if they are infinite.

Depending on the **continuity of the data:** Models are **discrete** when dealing with data that can be individualized into different units either statistically, or because the object of the modeling is discrete in nature. Instead it would be **continuous** if modeling is done on continuous data, such as velocity or temperature.

Depending on the **certainty in the answer:** Models can be **deterministic** if the result they give is exact or **stochastic** if their result is the probability and the mathematical expectation that each scenario of a diverse group of possibilities will occur, whether continuous or discreet.

Depending on the **dynamism:** Models can be **static** if they solve situations in equilibrium and therefore do not depend on execution time. On the other hand, models can be **dynamic** if the result depends on time because they evaluate all situations before reaching an equilibrium state (if it is possible to reach it).

Depending on the **scope of application:** Models can be **specific** (*ad hoc*) if they are designed to explain a specific case or situation and are not valid in other scenarios, or **general** if they can explain a set of different situations.

1.2.2 Diffusivity equation

The diffusivity equation is an equation deduced from the heat transfer equation and is widely used in numerical modeling for its versatility. This equation explains with its multiple variants different scenarios of mobilization of elements within a geometry.

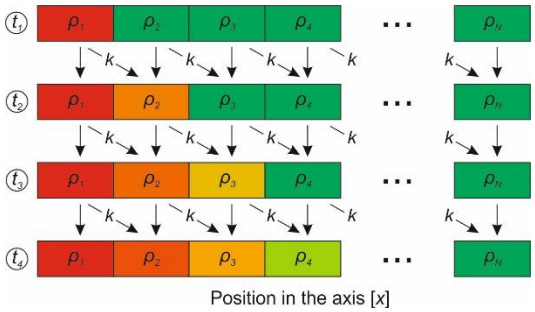

Figure 1.10: Sketch showing how the diffusion equation behaves in an unidimensional system through time. ρ is the value of the modeled element, x is the position on an axis, t is the temporal moment and k is the diffusivity constant. Contemporaneously to the evolution of the time steps from 1 to 4 there is a progressive change of ρ in all the cells, except in the cell ρ_1, where are set the boundary conditions.

The diffusivity is the property of matter to be distributed progressively in space without making large mass movements. Therefore, it is a different displacement from advection and convection. This property makes it especially interesting to study non-mass transport phenomena that occur throughout geological history, as although not being based on the mechanisms of hydrodynamic geological transport, most changes are so progressive that they can be explain by this mechanism.

There are multiple forms of the diffusivity equation, depending on the number of elements involved, the number of dimensions in which it is studied, whether it is calculated infinitesimally or in intervals, or if there are considered external conditioning factors of the formula. Its simplest expression is the one that explains the mobilization of a single element as a function of time in a single dimension (figure 1.10). This can be expressed as follows:

$$\rho(x,t) = \frac{N}{\sqrt{4\pi kt}} e^{-\frac{x^2}{4kt}} \tag{1.1}$$

Where ρ is the value of the modeled element, x is the position on an axis, t is the temporal moment, N is the number of elements in the simulation and k is the diffusivity constant. The diffusivity constant is a value that must be calculated empirically. However, sometimes it cannot be deduced empirically because the reality it represents is not given in the real world. It is the example of modeling displacements of sediment volumes, which is applied in this thesis. Because sediments are mobilized following hydrodynamic and gravitational processes, the diffusivity constant in this area is completely theoretical and must be estimated on a case-by-case basis. Being a space-dependent constant, if the dimensions of the modeled area change, the constant must also change.

2 OBJECTIVES

Foreland basins are regions on the Earth where there is a complex interaction between deep and superficial processes (DeCelles and Giles, 1996) and, therefore, it is not easy to understand the relationship between the processes and the importance of each one in the final result. All the questions on this thesis are formulated on the frame of these interactions, to evaluate how the variations in time and space of the tectonic and climatic conditions affect the sediment distribution and the routing systems.

The first objective considered was to **contribute to the knowledge of chronostratigraphy and the basin infilling in the study area**, focusing on improving the chronostratigraphy of the period in which the Tremp-Jaca basin system is incorporated on the thrust belt. Specifically, it was initially proposed to carry out two new magnetostratigraphic sections with a high sampling density to refine the previous datations. Those are the Olsón section, in the southern part of the Ainsa basin, and the Yebra de Basa section, in the western Jaca basin. Furthermore, a re-interpretation of previous magnetostratigraphic sections has been carried to obtain a precise chronostratigraphic frame for the whole basin, necessary to develop other tasks as the study of sedimentation rates or forward models.

The second objective was to **study the evolution of the sedimentation rates on the Tremp-Jaca basin** during the middle-late Eocene. This study will allow us to study the 4D distribution of the depocenters along with the tectonosedimentary evolution of the area. This objective will provide numerical data that will be used for the forward models of the basin.

The third objective is to **generate numerical models to assess the sediment routing and balance**. Those simulations have (a) to evaluate the basin response to the propagation of climatic and tectonic signals and (b) the general sediment routing on the southern Pyrenean foreland basins. In addition, the modeling must be done with the Dionisos software, to evaluate the incorporation of this tool to the research group.

Those three specific objectives will provide details in how were the sediment routing systems of the southern Pyrenean foreland basins during the Eocene. Also will provide hints to interpret similar foreland basins from other places.

3 METHODS

The present research involves different techniques to achieve the different considered objectives.

A contribution to the Chronostratigraphy and the basin infilling architecture has been made by application of Paleomagnetism. Here it is explained the basics of rock magnetism and geomagnetism, as the ground on which the paleomagnetic tools are based. Particular emphasis is made to the description of the magnetostratigraphic method as a dating tool of sedimentary sequences.

To study the evolution of the sedimentation rates on the Tremp-Jaca basin first it is here explained how we have done the systematic review of the published magnetostratigraphic data and then the backstripping process that has been followed to standardize the different studied sections to the differences of overburden along the basin.

Finally, to generate numerical models here it is explained the numerical theories applied on this research, the idiosyncrasy of the Dionisos software, used on this models and the workflow followed during the modelling. In the final part of the section there is also a glossary section for specify some of the wording used in models description.

The results on implementing those technics will bring tools for the discussion on the aimed topics.

3.1 Paleomagnetism

Paleomagnetism is the discipline of Earth Sciences that studies the evolution of Earth's magnetic field over time and its signature in the rock record in the form of remanent magnetization. The analysis of the direction of the remanent magnetization of rocks provides insights at global scale on the past location of lithospheric plates. At regional scale they help constraining the kinematics of curved fold-and-thrust belts (oroclinal bending). The analysis of the polarity of the remanent magnetization along stratigraphic successions is the basis of Magnetostratigraphy, a discipline that has contributed to the high resolution dating of basin’s sedimentary infill.

3.1.1 Materials and magnetism

All the materials have different behaviors when they are under the influence of a magnetic field. Their behavior depends on the distribution and interactions between

electric charges of their constituent subatomic particles. Depending on their behavior, materials are grouped into diamagnetic, ferromagnetic and paramagnetic materials.

Diamagnetism: Diamagnetic materials generate a magnetic field when they are subjected to the influence of an external magnetic field. The induced magnetic moment is weak compared to other magnetic behaviors, and of direction opposite to the external field (Figure 3.1a). Quartz and calcite are important rock-forming diamagnetic minerals. Gold, water and organic matter are other examples of diamagnetic materials.

Paramagnetism: When a paramagnetic material is exposed to an external magnetic field, the material aligns its magnetic moment with the external field. The induced magnetic moment is proportional to the external field, and the constant that relates both magnitudes is called magnetic susceptibility (*k*). The induced magnetization is lost when the material is no longer exposed to the external field (Figure 3.1b). Examples of paramagnetic minerals are iron silicates, such as clay-minerals and biotite, siderite, pyrite.

Ferromagnetism (s.*l.*): Ferromagnetic materials are able to retain a magnetic moment in the absence of an external magnetic field (Figure 3.1c). This stable magnetic moment, or magnetic remanence, is acquired at the time of mineral growth, rock formation, or cooling to below the Curie temperature of minerals. Iron oxides such as magnetite, maghemite and hematite,

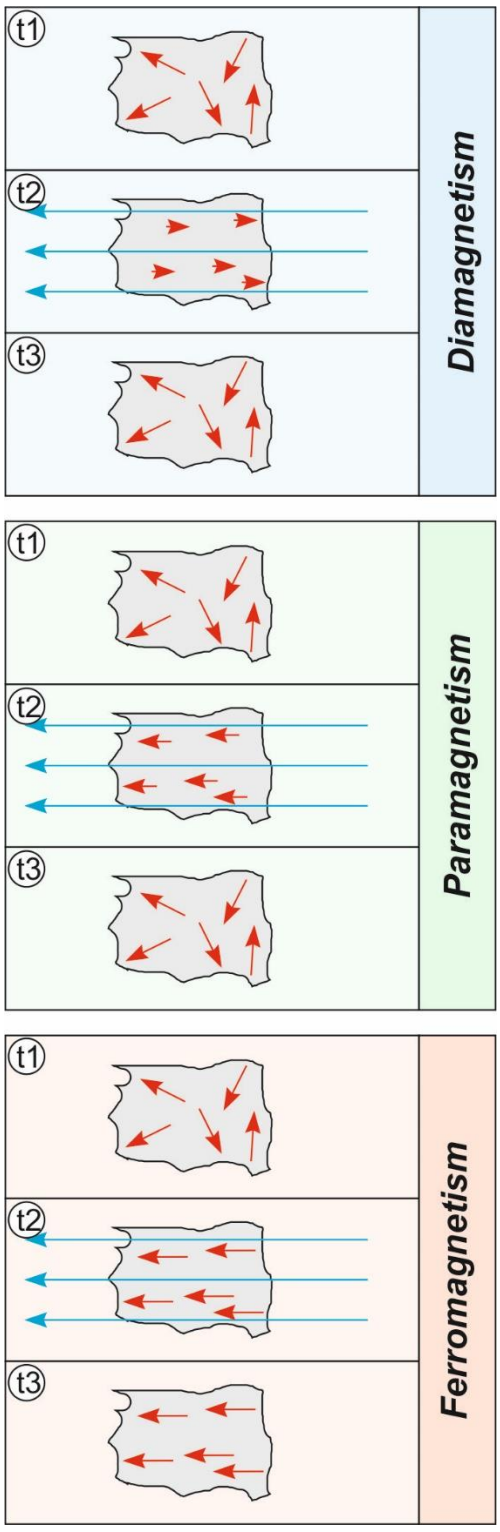

Figure 3.1: Three different types of magnetic materials and their relation with the application of an external magnetic field (blue arrows).

goethite and sulfides such as pyrrhotite and greigite are among the most common ferromagnetic minerals.

Most rocks contain ferromagnetic minerals which make them suitable for paleomagnetic studies. This is because they can record the Earth's magnetic field at the time of its formation. Ferromagnetism (*s.l.*) includes different kinds of spin interactions within the crystal, leading to either ferromagnetism (*s.s.*), antiferromagnetism, and ferrimagnetism (Figure 3.2).

Ferromagnetism (*s.s.*): The magnetic moments associated to the spin of unpaired electrons of some transition elements such as Fe within a crystal are all aligned in the same direction, generating a magnetic field in such direction. Native iron is ferromagnetic *s.s.*

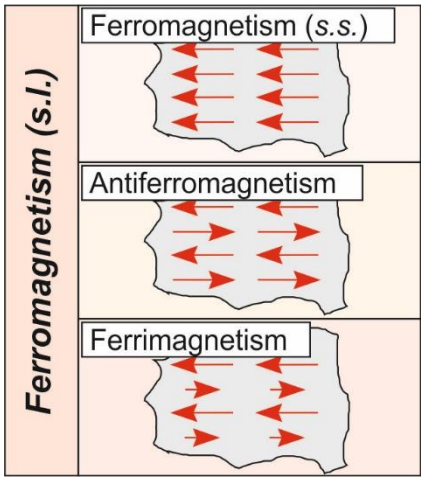

Figure 3.2: Different types of ferromagnetism (*sensu lato*) and the internal organization of the magnetic vectors (in red) for each type.

Antiferromagnetism: The magnetic moments within the crystal are aligned but in successively opposite directions, so that the exact 50% of the material generates field in one direction and 50% generates it in the opposite direction. So theoretically, the bulk remanent magnetism in an antiferromagnetic sample is zero. Nevertheless, in natural materials the bulk remanent magnetism will always generate a small magnetic field as nature is not perfectly isotropic. A special type of antiferromagnetism is the **Canted antiferromagnetism**, that is when the structure of the crystal lattice causes that opposing magnetic moments are not perfectly antipodal, as in hematite, resulting in a stable moment in a perpendicular direction.

Ferrimagnetism: As in the case of the antiferromagnetism, the electronic spins are aligned in opposite directions. The difference between this situation and the previous one is that the electronic spins aligned in one direction generate a more intense field than those aligned in the opposite direction. So, a bulk remanent magnetization can be measured. Magnetite is the most common ferrimagnetic mineral, and among the best suited for paleomagnetic studies.

The acquisition of ferromagnetism (hereinafter, magnetism) by rocks depends, first, on the rock-forming processes, and secondly, on the physico-chemical alterations that may occur during burial, diagenesis, and exhumation history of rocks.

Igneous rocks lock a stable magnetization as they are cooled below the blocking temperature of their magnetic minerals. This temperature is characteristic of each material and is approximately 100 °C below the Curie temperature (Butler, 1992). The Curie temperature is the temperature below which minerals shift from paramagnetic to ferromagnetic behavior and is generally below the melting temperature of their host rocks. See table 3.1 for some examples.

Mineral	***Curie temperature [°C]***	***Melting point [°C]***
Magnetite	580	1538 (Fe)
Hematite	675	1565
Goethite	120	300*
Pyrrhotite	320	1080

*Goethite undergoes dehydration from this temperature and is transformed into hematite

Table 3.1: Curie temperature and melting point of different magnetic minerals. In all the cases the Curie temperature is below of the melting point. Data from Lide (2000), Garcés (2014) and Bhagat (2019).

In the case of slowly cooling igneous rocks, there is a delay between the rock formation and the Earth magnetic field acquisition. On the other hand, in volcanic rocks the remanent magnetism is acquired practically at the time of its eruption, giving an almost faithful record of the Earth magnetic field at the time of formation.

Terrigenous sedimentary rocks acquire the remanent magnetism from the alignment of the tiny detrital magnetic particles after settling. If those particles are light enough, they orient themselves following the Earth's magnetic field, rotating until are aligned with it. The magnetization is locked-in when the particles can no longer rotate, as a result of the early stages of rock lithification (Figure 3.3).

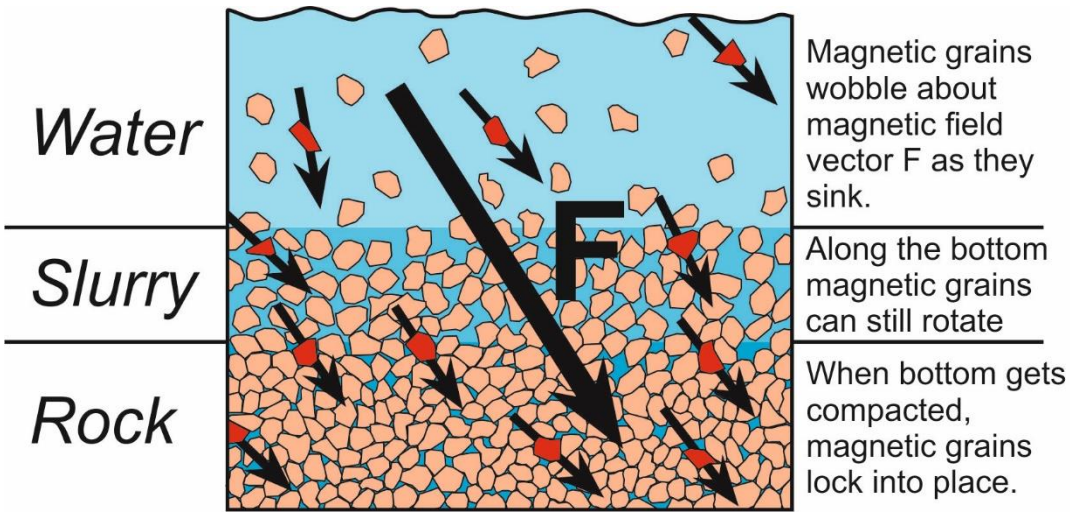

Figure 3.3: Simplified sketch showing the acquisition of a detrital remanent magnetization in a sedimentary layer. Until the sediments are compacted, those can rotate and reorientate following the Earth magnetic field (blue arrow) (Cox and Hart, 1986).

In many sedimentary rocks a remanent magnetism of chemical origin can be acquired. It results from the chemical precipitation of ferromagnetic minerals within the pores of the sediment or replacing other minerals. The magnetization is locked-in when the growing crystals exceed a critical volume.

The chemical remanent magnetism can be acquired in an early or late stage after sedimentation. If it is significantly delayed relative to the time of sedimentation it is considered a secondary magnetization, in opposition to the primary magnetization acquired at the time of rock-formation. Secondary chemical remanence may form in the late phases of diagenesis as a consequence of the circulation of fluids. It can also occur near the surface in exhumed rocks associated to processes of rubefaction, weathering, etc. As a result, a sedimentary rock may hold different magnetizations of primary and secondary origin residing in different populations of magnetic particles.

3.1.2 Earth magnetic field

The Earth's magnetic field is highly complex and mutant throughout the geological history, but for the period of interest it can be simplified to a magnetic dipole with its axis roughly coinciding with the Earth's rotation axis. This simplification is valid for most of paleomagnetic applications where the time averaged field, for time lapses greater than 10^4yr, is the reference frame. (Tauxe, 1998).

The formation of the dipole is consequence of the rotation of the semisolid outer core of the planet. This generates a magnetic field by a process comparable to that of rotating a magnet inside a

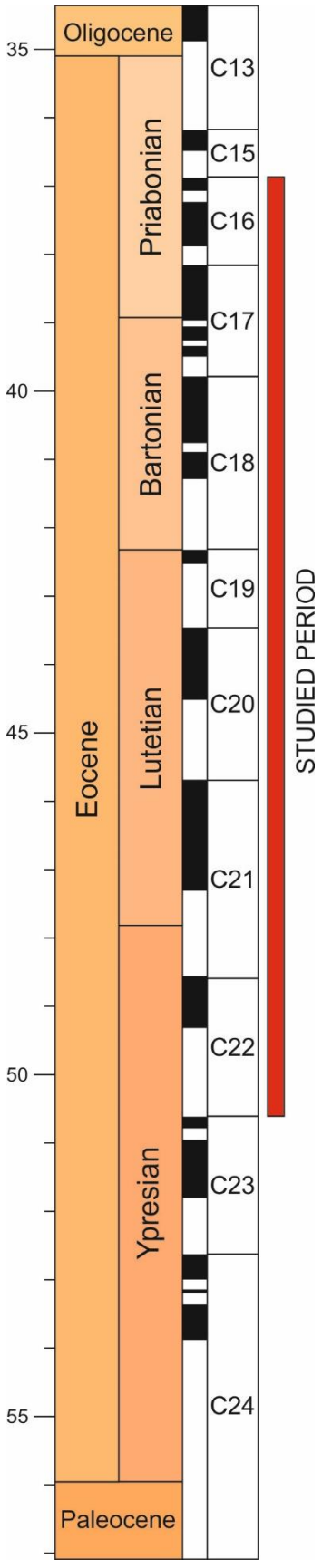

Figure 3.4: GPTS for the Eocene (Gradstein and Ogg, 2012). The studied period is highlighted in red.

copper coil. For reasons that are not yet fully understood, but that explore different publications (Glatzmaier and Roberts, 1995; Merill *et al*., 1998; Muller, 2002; among others), this dipole periodically reverses its polarity in irregular periods. As those inversions of the magnetic field are a phenomenon that happens on a planetary scale instantly, it forms magnificent timelines that are used in magnetostratigraphy.

The field reversals are documented in the Geomagnetic Polarity Time Scale (GPTS, Figure 3.4), which is calibrated with absolute dating techniques, such as radiometric dating and astrochronology. The current version is that of Grandstein and Ogg (2012), but previously other GPTS scales like Cox (1964) or Cande and Kent (1995) have been used. In the future, the GPTS will be updated with new geomagnetic chrons of short duration that have not yet been resolved (Garcés and Beamud, 2020).

As the model of the magnetic dipole approximates the Earth magnetic field, there are some minor variations on the position of the poles known as secular variations. Those variations usually take place in the first latitudinal 30° from the geographic poles. If those variations exceed these limits, they are referred to as magnetic excursions. If the field excursion is of longer duration and enters into the opposite hemisphere, then it is referred as a field reversal.

3.1.3 Magnetostratigraphy

The processes described below explain how to sample a sedimentary section, to identify the primary magnetization of sediments, to build a local magnetic polarity sequence, and to put forward a correlation of the local magnetostratigraphy with the GPTS, thus providing ages for the sequence of reversals found in the section.

Sampling

A sedimentary section suitable for magnetostratigraphy must be continuous and outcrops accessible for sampling at the required resolution. Bed by bed stratigraphic superposition is required in order to avoid unwanted gaps or repetitions during sampling. A lithostratigraphic section with measured thickness and position of sampled levels is required. The spacing between sites depends on the estimated age and duration of the section, as the number of field reversals per time unit expected to be found varies throughout the GPTS. It also depends on the estimated sedimentation rates. Indeed, the precise age and duration of the section is at this stage unknown, and often it may only be guessed from the broad regional context. Then, the choice of sampling spacing must be conservative, if age constraints are loose.

The sampling density finally achieved, however, will be conditioned by the quality of the outcrops, as well as by the availability of appropriate lithologies. The detrital sedimentary rocks acquire magnetism by orienting the magnetic particles with the Earth magnetic field as they deposit on the basin floor (figure 3.3). So, the sampling target are the finer lithologies, as the magnetic particles are lighter enough to rotate. Appropriate lithologies range from clay-sized shales to very fine-grained sandstones. Other lithologies may be appropriate for sampling, but the presence of potentially oriented magnetic elements must be carefully evaluated in each case. Three other good examples than fine lithologies that can be sampled could be a conglomerate with a very fine matrix, abundant enough to be sampled; a very poorly selected coarse sandstone that therefore have a very fine matrix; or a paleosoil in a sandstone with a high percentage of hematite cement.

Once located the sampling sites, for each site can be done the following steps:

The site must first be located, both on a map, using a GPS when possible, and in the lithostratigraphic section. The local bedding dip must be collected among all the notes that are considered necessary for interpreting the results. Then, it is necessary to clean the sampling spot by removing the altered material on surface until reaching the fresh rock. With the fresh rock uncovered, a rotary drilling is made to extract a rock core. A minimum of two cylindrical 2 cm high samples must be taken at each site. In places where is more difficult to drill, instead of cylindrical samples can be collected oriented fragments of the rock that will be cut later in the lab. Once the samples are collected, the next step is to take the orientation of each sample with respect to current geographic coordinates with the help of an orientation device; a tool that combines a sun or magnetic compass with an inclinometer to measure the azimuth and a dip of each sample. In later steps these data will be used together with the bedding attitude to restore the original position of the sample at the time of sedimentation.

Laboratory procedures

The main concern of the laboratory analyses is to isolate the different magnetic components contributing to the NRM, and to distinguish the primary from the secondary magnetizations. An interesting feature that helps on this process is that secondary magnetizations are often of viscous nature and have lower unblocking temperatures compared to primary magnetizations. So, in order to isolate the primary component of the NRM a stepwise demagnetization with increasing temperature can be applied to samples (TH) or by submitting the sample in an increasing external alternative magnetic field (AF). After each demagnetization step, the remanent magnetization is measured,

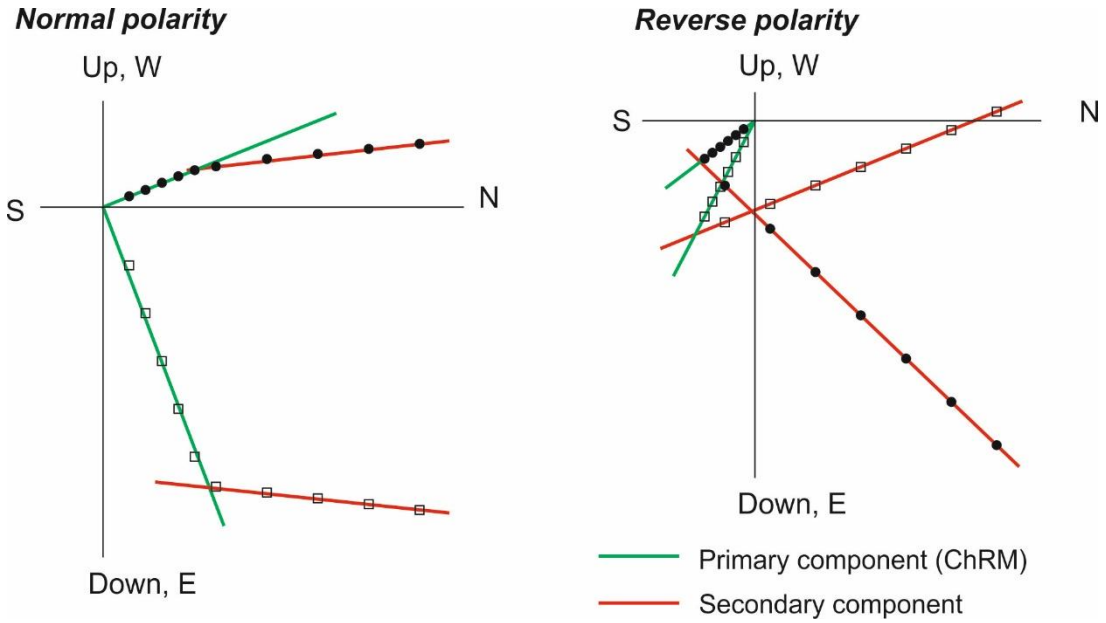

Figure 3.5: Idealized Zijderveld diagrams of a normal and a reversal site showing how the primary component (ChRM) can be isolated from the secondary component.

and all resulting NRM vector endpoints are plotted in a Zijderveld diagram (Zijderveld, 1967). This diagram is useful to understand the trajectory of the remanent magnetism during the demagnetization of each sample. This trajectory allows to separate the Characteristic Remanent Magnetization (ChRM) from secondary components (figure 3.5). The ChRM is the component identified for being the most stable and representative of the rock unit.

Sample preparation includes cutting the core samples into standard cylindrical specimens of 2.2 cm in length. For each sampling site is selected the sample that is presumed to have the better developed magnetic component for its measurement in function of the grain size, mineralogy… Twin samples from each site are archived in case of some measurements needs to be repeated. With the entire collection of samples selected, its natural remanent magnetism (NRM) and its initial magnetic susceptibility (χ) are measured. From this point on, the samples will be demagnetized in a destructive process, so it is necessary to put a special care on the process. As stated earlier, demagnetization can be done by two different procedures: thermal demagnetization (TH) or alternating magnetic field demagnetization (AF).

In the case of TH demagnetization, the sample is initially heated up at 100 °C and the successive steps increase the temperature by 50 °C. This increase will be reduced as the sample approaches the blocking temperature. The remanent magnetization is measured after each heating step in the rock-magnetometer. Also, for each step the magnetic susceptibility is measured to monitor the growth of magnetic phases as a

consequence of the temperature increase. Each sample is heated up until reaches the unblocking temperature of its minerals or until the trajectory of remenance vector reveals an erratic path.

In the case of AF demagnetization, the sample is progressively demagnetized by submitting it to an alternating magnetic field of increasing peak intensity, starting with increments of 10 mT and ending with increments of the order of 100mT up to 1 T. This magnetic field is applied separately to the three sample coordinate axes (x, y, z) to homogeneously reduce the intensity of the magnetic components. In the case of demagnetization by AF it is not necessary to measure susceptibility, as high magnetic fields do not contribute to the generation of new minerals. For this reason, the AF approach is especially useful for samples containing iron sulfides.

The directional behavior of NRM demagnetization data is visually inspected by means of Zijderveld diagrams. Paleomagnetic directions are analyzed after correction for the geographic orientation of each sample, as well as the bedding attitude of the sampling location. The most stable component, namely ChRM, could represent either a primary or secondary magnetization, and this has to be evaluated with a series of quality tests. In order to assess the primary nature of the ChRM directions, coherency with the expected direction of the magnetic field at the site latitude must be observed after correction for tectonic tilt.

Field tests

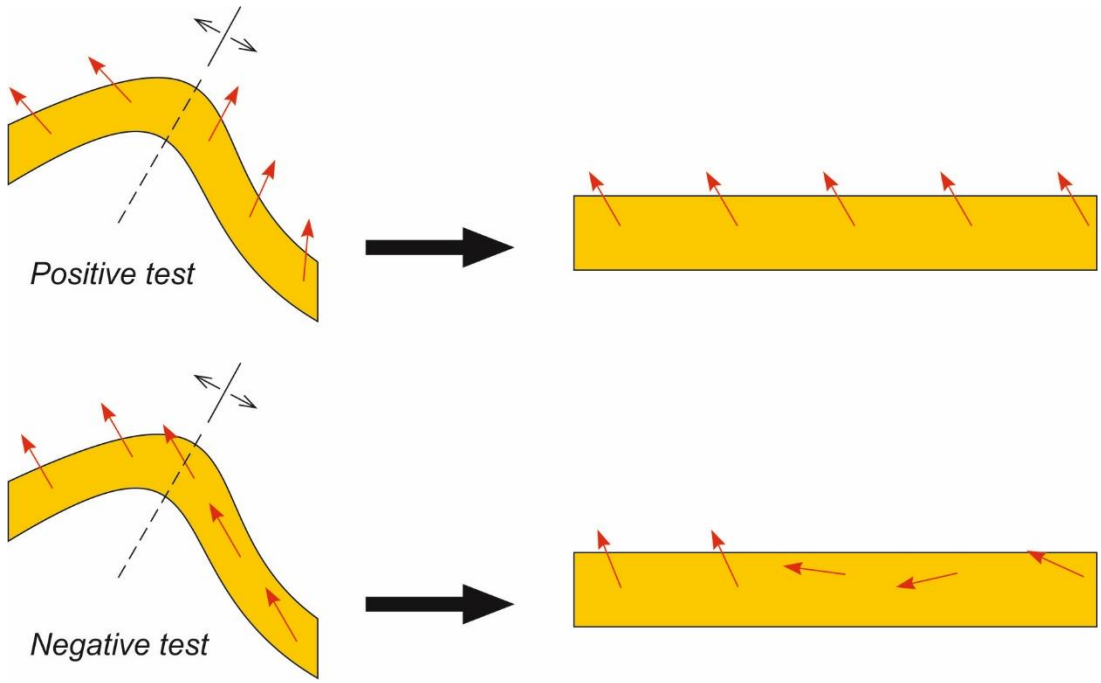

Figure 3.6: Fold test, consisting in restituting the magnetic vectors of the both limbs of a fold and observe if they are aligned after the restitution. If they are, the test is positive.

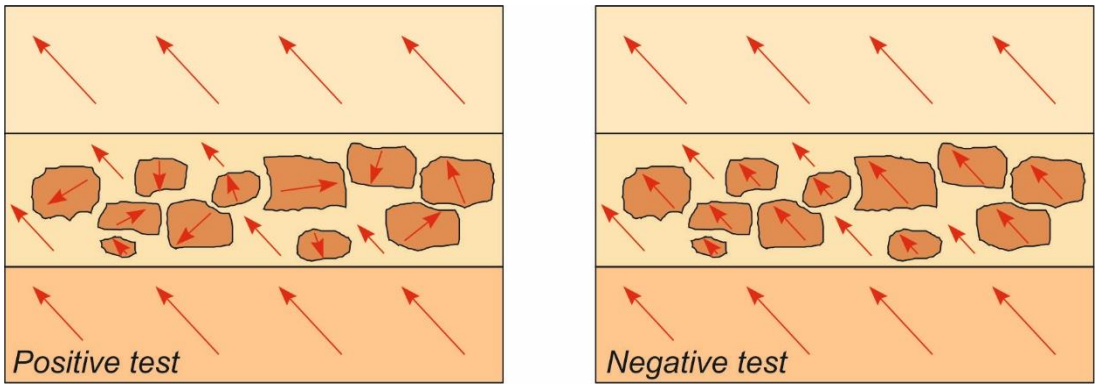

Figure 3.7: Conglomerate test, consisting in comparing the direction of the magnetic vectors in the pebbles and in the matrix/surrounding strata. When the test is positive, the magnetic vectors of the pebbles have random directions while in the matrix those are organized in one direction.

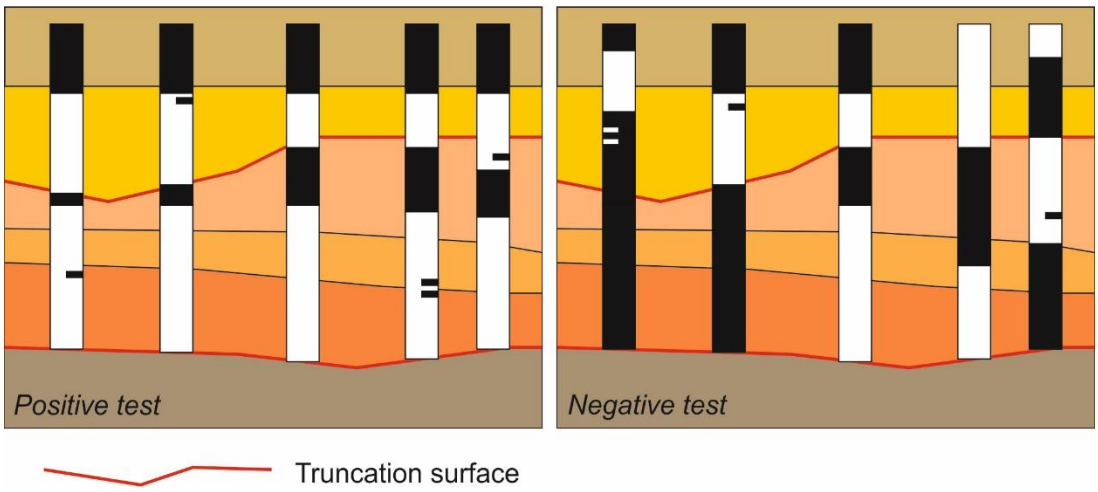

Figure 3.8: Consistence test. This test compares different magnetostratigraphic sections of the same area and laterally equivalents. This test is positive when the reversals are coherent between them.

A number of tests can be carried out in order to assess the stability and relative age of the ChRM. These tests are the fold test, the conglomerate test, the consistency test and the inversion test. Although it is not necessary to perform all the tests on every site, it is recommended to do more than one to be sure of the quality of the data.

The **fold test** consists of taking the ChRM of samples taken from both limbs of a fold and then checking if they show the same direction after unfolding the two limbs. If the ChRM vectors converge to the same direction, even if in reversal directions, the fold test is positive (Figure 3.6). This is useful to check if the ChRM predates folding, but the rocks could have been remagnetized during the period between the rock formation and folding.

The **conglomerate test** consists of separately measuring samples taken from pebbles in a conglomerate and then samples taken from the strata immediately above or below the conglomerate. The test will be positive if the ChRM measured in the pebbles of the

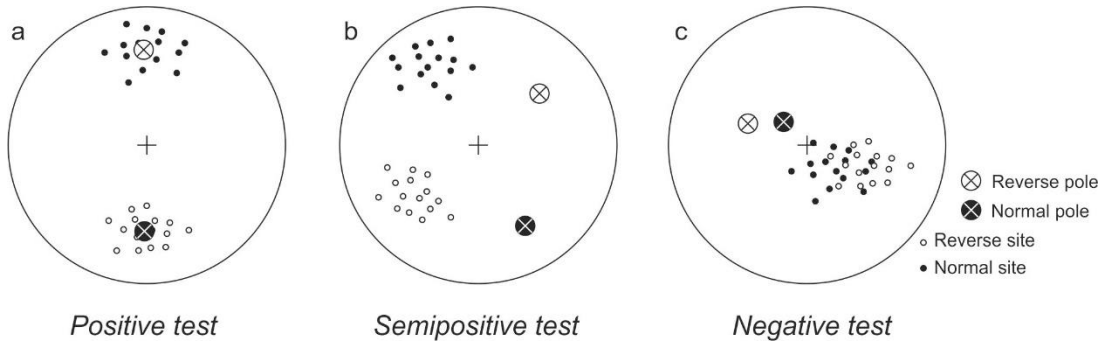

Figure 3.9: Inversion test. This test shows if the Fisher distribution of the normal and reverse samples is or is not antipodal. The test is positive when they are antipodal. But if they are not antipodal but it can still be distinguished two populations of sites, the test can be considered as semipositive, meaning that the section is not useful to calculate vertical axis rotations, but it allows to distinguish the normal from the reverse sites, allowing to interpret the magnetostratigraphy.

conglomerates give a random dispersion and, the samples taken in the immediately upper or lower strata, give the same direction between them (Figure 3.7).

The **consistency test** consists of comparing the magnetozone sequence of several lateral equivalent and correlatable sections to see if the results obtained are consistent with each other. The test will be positive if the magnetic polarity reversals are found to occur at equivalent stratigraphic position in the various sections (Figure 3.8). This test is useful if it is suspected that some local alteration (*e.g*. water circulation in a fault) may have produced secondary magnetism.

The **reversal test** consists of assessing the antipodality of the sets of samples of normal and reverse polarity of a section. First, the Fisherian mean (Fisher, 1924) of each polarity set is calculated to evaluate if the dispersion is or is not random. Then, if the two mean directions are found to be antipodal, the test is positive (Figure 3.9). If it is negative, however, it does not mean that the samples obtained should be discarded. It means that the ChRM directions are not perfectly isolated and are partially overprinted by a portion of secondary components. These overprinted directions may still be interpreted with caution in terms of magnetic polarity, while they cannot be used for assessing vertical axis rotations.

Magnetostratigraphic correlation

In magnetostratigraphic correlation the first step is to interpret the polarity of all primary ChRM directions. This is done by calculating the corresponding the virtual geomagnetic pole (VGP) latitude at sample level. VGP latitudes range from -90º to +90º. Positive VGP latitudes are interpreted to represent periods of normal polarity of the geomagnetic dipole, while negative VGP latitudes represent reversed polarity. The next steps are to

divide the lithostratigraphic sections into magntezones according to the polarity revealed by the sampled sites. To interpret a magnetozone, there must be at least two consecutive samples yielding the same polarity. If this situation does not occur, then the sample can be represented with a half bar to indicate a possible very short geomagnetic chron or magnetic excursion.

The resulting local magnetostratigraphy is finally correlated to the GPTS. To make this correlation, several aspects must be considered. The correlation must first be done by grouping the zones with a mostly normal polarity and the zones with a mostly reverse polarity and then identify the target interval in the GPTS. Once this first coarse correlation is made, the next step is to refine the correlation by linking each magnetzone with its corresponding geomagnetic chron. It must be taken into account that some short magnetozones might be missing in the sampled section due to either a sampling bypass or overlooked stratigraphic gaps. Similarly, it is possible that short magnetozones found in the sampled section represent true “new” geomagnetic chrons not yet incorporated into the GPTS. For these reasons, it is crucial not to try making a chron-to-chron correlation in first place, as the oscillating nature of the magnetic field combined with the discontinuous nature of the sedimentary record is likely to lead to misinterpretations.

Magnetostratigraphic completeness test

For magnetostratigraphic correlation to work, magnetostratigraphic completeness is crucial. It is not referred here to the presence or not of sedimentary hiatus, but to the sampling distribution and resolution. Magnetostratigraphic completeness is attained when sampling spacing was of sufficient resolution to record all the magnetozones present in the studied stratigraphic section. There are two main methods to do this. The first is the one described in Johnson and McGee (1983) which indicates that a section has a sufficiently solid resolution when there are more than 8 samples of the same polarity defining a chron.

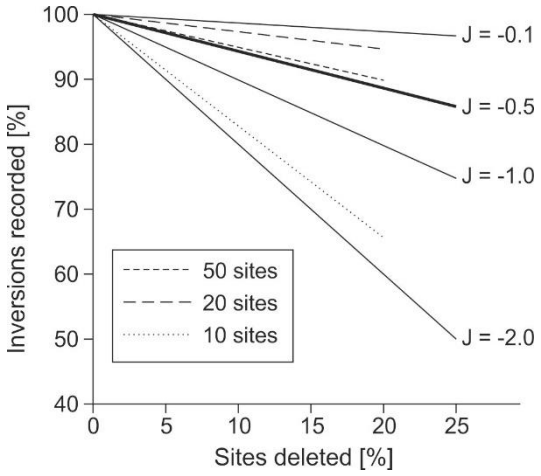

Figure 3.10: Example of a Jackknive test after different simulations, redrawn from Tauxe and Gallet (1991). Observe that as more sites are collected in a section, less slope (J) has the linear regression. It is estimated that a magnetostratigraphic section has captured the significant chrons if J is higher than -0.5.

The other method is called magnetostratigraphic jackknife (Tauxe and Gallet, 1991). This test compares the

number of reversals retrieved with the number of samples taken by progressively removing random sites until it removes the 20% of the samples. Then a plot is constructed where the vertical axis represents the percentage of inversions detected –100*[inversions detected]/[inversions on the GPTS]– and in the horizontal axis represents the percentage of sites deleted. This plot results in a linear regression with a slope J (figure 3.10). The test is positive when J is higher than -0.5.

3.2 Sedimentation rates calculation

3.2.1 Review of the preexisting magnetic data

To integrate the different sedimentation rates of the basin, first a critical review of the available data that can provide information about them must be done. This corresponds to all the thickness data that can be related with a duration. In the case of this thesis, it

Magnetostratigraphic section	***Reference***	***1***	***2***	***3***	***4***
Pobla de Segur (PS)	Beamud *et al.*, 2003				
Sis	Beamud *et al.*, 2003				**X**
Roda	Bentham and Burbank, 1996	**X**			
Esplans	Bentham and Burbank, 1996	**X**			
Lascuarre (LS)	Bentham, 1992				
Esera (ES)	Bentham, 1992				
Mediano (MD)	Bentham, 1992				
Eripol	Bentham, 1992	**X**	**X**		
Almazorre	Bentham, 1992	**X**			**X**
Liguerre	Bentham, 1992		**X**		
Belsué (BL)	Garcés *et al.*, 2014				
Salinas	Hogan and Burbank, 1996			**X**	
Arguís/Monrepós	Hogan and Burbank, 1996				**X**
Yebra de Basa	Hogan and Burbank, 1996		**X**		
San Felices	Hogan and Burbank, 1996				**X**
Agüero	Hogan and Burbank, 1996				**X**
Ayerbe	Hogan and Burbank, 1996				**X**
Arguís/Pico del Águila	Kodama *et al.*, 2010				**X**
Mondot (CM)	Mochales *et al.*, 2012				
Coscollar (CM)	Mochales *et al.*, 2012				
Río Gállego/Río Aragón (GA)	Oms *et al.*, 2003				
Santa Marina (SM)	Rodríguez-Pintó *et al.*, 2012 (a)				
Isuela (IS)	Rodríguez-Pintó *et al.*, 2012 (b)				
San Pelegrín	Rodríguez-Pintó *et al.*, 2013				**X**

Table 3.2: Relation of published magnetostratigraphic sections and the exclusion criteria marked with "X": (1) Average number of samples/magnetozones lower than 8. (2) Large number of magnetic reversals on the GPTS not found on the magnetostratigraphic section. (3) Data far-off from the studied profile. (4) Not the best section at a specific location, with respect to the overall quality of the data. The sections selected for this study are indicated in bold, see their location in figure 4.10.

has been chosen to study all the magnetostratigraphic data published in the studied area plus two new magnetostratigraphic sections performed.

After a critical review of the published data of the area, the magnetostratigraphic sections that include significant information during the Lutetian, the Bartonian and the Priabonian have been selected. This means all the magnetostratigraphic sections containing significant information from chron C22 to C16 (figure 3.4) and provide sufficient time-resolution to study the variations in sedimentation rates (table 3.2). The following criteria have been applied for the selection: (1) sections with an average number of samples/magnetozones lower than 8 were considered to have insufficient resolution (Johnson and McGee, 1983) and were excluded; (2) magnetostratigraphic sections that correlate with the Global Polarity Time Scale (GPTS) that missed significant geomagnetic chrons were excluded; (3) to better capture the 2D geometry along basin transects, data far-off from selected segments were ignored; (4) where multiple sections were available, the above quality criteria were applied to select the best section for a specific location. The selected sections were decompacted by backstripping. All the considered sections with the exclusion criteria are summarized in the table 3.2

3.2.2 Backstripping

Sediments are compacted after deposition, therefore the thickness of the sedimentary interval preserved is smaller than the original depositional thickness. Compaction directly depends on the pressure that is applied to the sediment mass onto the underlying strata. As this compaction reduces the thickness of the rock, a decompaction process is required to restore the original thickness in order to calculate the sedimentation rates. The decompaction of the different sections was calculated following the methods described by Angevine *et al.* (1992) and are based in two equations.

In one hand, the first equation was the porosity reduction law, that stablishes an exponential rate of decay of the porosity as the burial depth (*i.e.* lithostatic pressure) increases.

$$\emptyset_f = \emptyset_i \, e^{(kZ)} \tag{3.1}$$

This equation shows that the final porosity ($\emptyset_f$) depends on the initial porosity ($\emptyset_i$) and has an exponential relation with the burial depth (Z) and with a constant (k) that depends on the mineralogy and petrology of the rocks. The second equation in which is based this backstripping is the relation between the original thickness and the thickness in the past.

$$T_i = \frac{(1-\emptyset_f)T_f}{1-\emptyset_i} \tag{3.2}$$

In this equation the initial thickness (T_i) depends on the relation between the final and the initial porosity and the thickness in the final steps of the compaction (T_f). replacing the equation 3.1 on the equation 3.2, can be easily deduced this relation:

$$T_i = \frac{(1-\emptyset_i e^{(Zk)})T_f}{1-\emptyset_i} \tag{3.3}$$

This equation is an approximation that decompacts all the volume in one step, but as the lithological conditions change with depth, there is a more accurate method to achieve the decompaction, by using the following relation:

$$\int_{Z_i}^{Z_i+T_i}(1-\emptyset)dx = \int_{Z_f}^{Z_f+T_f}(1-\emptyset)dx \tag{3.4}$$

The relation assumes that the volume of rock grains $(1-\emptyset)$ is stable during all the compaction process, so the porosity reduction only depends on the reduction of the porosity. If those two integrals are analyzed analytically (Angevine *et al*., 1992), is obtained the following relation:

$$T_i + \frac{\emptyset_i}{k}e^{(-kZ_i)}\left(e^{(-kT_i)}-1\right) = T_f + \frac{\emptyset_f}{k}e^{(-kZ_f)}\left(e^{(-kT_f)}-1\right) \tag{3.5}$$

This is a transcendental equation, so it is impossible to solve the equation for T_i. A strategy for approximate the value of T_i is isolating one of both values of T_i and estimate a value for the non-isolated T_i. The result of solving the equation with this value will be used on the next iteration as the new value of T_i on the equation until the value gets stabilized. Isolating one T_i is obtained the following equation:

$$T_i = -\frac{\emptyset_i}{k}e^{(-kZ_i)}\left(e^{(-kT_i)}-1\right) + T_f + \frac{\emptyset_i}{k}e^{(-kZ_i)}\left(e^{(-kT_f)}-1\right) \tag{3.6}$$

In summary, there are to methods for doing the decompaction of a stratigraphic succession, in one hand, there is the direct method, following the equation 3.3, and the iterative method, following the equation 3.6. The iterative method is more exact but is more time consuming to achieve the results and less stable. The direct method is less precise but is faster and appropriate when dealing with long periods of time.

All those equations assume that the thickness of a compacted unit depends on the change of porosity during the burial, but the volume of the grains does not change during compaction. The decreasing compaction coefficient rate (*k*) of the different lithologies is empirically defined from different studies. Here we have used the data from Angevine *et al*. (1992), choosing an exponential relationship for the change in unit porosity. To

perform this calculation requires to estimate the maximum burial of the sections. The overburden values used on the decompactions of this thesis are on the table 4.2.

Finally, once the sections are decompacted, they can be compared among them without fear any artifact due to the differential compaction all along the basin.

3.3 Numerical modeling

Numerical modeling consists in simplifying the reality to isolate the fundamental elements of a particular problem and eliminate secondary aspects by reducing the reality to a set of mathematical equations.

3.3.1 Theoretical principles

There are two major types of approximations in modeling. On the one hand, direct modeling –that is, asking about the results of a process– and on the other hand, the inverse modeling –that is, knowing the results of a problem, asking about which processes lead to the result–.

To give an example for each case, a direct problem would be to ask how a sedimentary system in equilibrium will respond if sediment supply suddenly doubles (Will more sediment accumulate at a particular point? Will the excess of sediment bypass the sedimentary system to the ocean? Will erosive areas start accumulating sediment? etc.). Alternatively, a reverse problem would be to ask what might have caused a sudden increase on the sedimentation rates (Increase in subsidence? Increase of the sediment supply? Change in the depositional slope? etc.).

Although the above examples are specifically devoted to sedimentology, similar questions could be asked perfectly in the case of precipitation of a mineral in an epithermal deposit, the propagation of heat around a volcanic chimney or even of the response of the human immune system to a particular pathogen.

In this thesis, all the numerical models have been made from the diffusivity equation, conveniently modified and implemented in the software Dionisos (Granjeon and Joseph, 1999). The diffusivity equation comes from the heat transfer equation and has the following structure:

$$Q_s = Sk_s + S^m Q_w^n k_w \tag{3.7}$$

Where *Qs* is the sediment supply of a point of the basin, *k* is the diffusivity constant. The diffusivity constant is a theoretical value that modulates the distance that a specific sediment is able to travel. In the equation applied to sedimentary models, a different

value can be assigned depending on whether the sediment moves in a marine or non-marine environment, and a different *k* must be used for each grain size. *Qw* is the flow, *S* is the slope, and *m* and *n* are two coefficients that modulate the formula depending on whether the transport is more gravitational or water driven. Empirically, it has been observed that an appropriate value of *m* should be set between 1.5 and 1 and the value of *n* should be set between 1 and 1.2. In all the models of this thesis it has been used the values of *m* = 1.3 and *n* = 1.

This formula has an important theoretical component, as it does not really express hydrodynamic properties, but expresses the tendency of a volume of sediment to move depending on the slope (gravity) and the available flow. Therefore, the results obtained from modeling with this formula for each time step should not be understood as a single stratum, but as a group of them. Consequently, modeling using this formula will not be indicative of a single specific event but will be very useful for quantifying the broad regional infilling of an area.

3.3.2 Dionisos

Beicip's commercial software Dionisos (Granjeon and Joseph, 1999) has been used in the framework of this thesis. This software implements the diffusivity formula presented in the section 3.3.1. This formula is repeated in the successive time steps of a simulation for each cell of a grid, so that in the end it generates a three-dimensional grid with information on geometry (slope, bathymetry, thickness...), water flow and percentage of each sediment in each cell of the grid. Additionally, other parameters are also calculated by operating the hard results of each cell, such as water turbulence (sum of the proportions of each sediment divided by the corresponding water flow), sedimentation rate (sum of the proportions of each sediment divided by the duration of each temporary step), distance of one point to the shoreline...

A carbonate generation equation is also running at the same time as the diffusivity equation. This equation depends on multiple environmental parameters such as bathymetry, water turbulence, flow, temperature, salinity... Basically what it does is generating a carbonate thickness for each cell following the productivity assigned to it and modulated by the above parameters.

$$T_{CO_3} = PM \tag{3.8}$$

Where T_{CO_3} is the carbonate thickness *P* is the productivity and *M* is the multiplication of all the parameters that modulate the carbonate production, normalized between 0 and

1. This equation runs parallel to the diffusivity equation, to take into account how the geometry of the basin would change.

Dionisos also incorporates other formulas into its workflow. An example is the formula that computes erosion at each point, but this is not as well implemented as the diffusivity equation and should be used with caution.

In the next sections will be explained in general terms the workflow that is most convenient for solving a Dionisos model. This workflow can be used on other programs with similar numerical approximations. Specifically, the workflow is intended to solve an inverse problem through direct modeling and use Monte Carlo simulation as a methodology.

So, this workflow solves which processes takes place to produce a given sediment distribution. Therefore, this workflow works from a deterministic model or a representation of the reality, which will be reproduced through Dionisos modeling. The strategy is to make multiple models with small variations between the parameters and then automatically or visually search for the closest result to the compared model.

1st step: The inquiry

When modeling it is essential to have a well-defined question to answer, otherwise the model does not make sense. All models are a simplification of reality, and this simplification needs to be done in a way that is consistent with the result that you want to achieve. It is difficult that a model can answer other than the specific topic for which is designed, so this inquiry has to be (1) clear, (2) delimited in space and time, (3) adjusted to the formulas, and available resources (*e.g*. hardware, software…) and (4) that the effort devoted to answering it is consistent with the importance of the unknown.

Asking a good question is the essential basis for making a good model. You should invest all the time you need and even a little more to be completely convinced of its relevance and adequacy.

2nd step: The calibration model

The calibration model is the first approach to answer the inquiry. The objective of this model is to find the order of magnitude of the variables and setting the boundary conditions. Those boundary conditions could be the initial geometry, time steps, total time, or the characteristics of each sediment type. On the other hand, the variables could be the eustasy, the sediment supply or the carbonate production, among others. Usually, some of the variables also have to be fixed in function of the inquiry. Each variable added

to test in the model exponentially increases the number of simulations needed to solve the question, so it is important to economize what is being evaluated.

Finally, in the calibration model it is recommended to adjust the diffusivity constants (*k* from the equation 3.7). Being the *k* dependent on the system on which work, but of a totally theoretical nature, they must be adjusted manually for each model and must be readjusted each time that there are changes in the geometry, the temporal dimensions, the time steps, the sediment supply or the water flow, among others. Dionisos has a built-in diffusion coefficient calculator that is broadly precise, but it is recommended to use it prudently and check carefully that the result is coherent with the expected behavior of each sediment.

3rd step: Generation of the different Monte Carlo scenarios

Once known the expected range in which the different variables can fluctuate, within this range must be first determined the number of simulations that will be needed to evaluate all possible situations, as well as establish the distribution of the values of all the variables.

For the number of simulations required, there is not a pre-established mathematical rule. This number will depend on the range of each of the variables, the number of variables and their distribution. In addition, the time that will take running each simulation must also be considered.

On the other hand, the distribution of the different variables values can be established in different trends. For example, if our variable is the waves energy, it is possible that the range was very wide in the past, but in the case of a river-dominated delta we know that the waves provably will have low energy. In this case a binomial relation can be established where the maximum probability is 0 and decreases until the value is higher enough (figure 3.11a). On

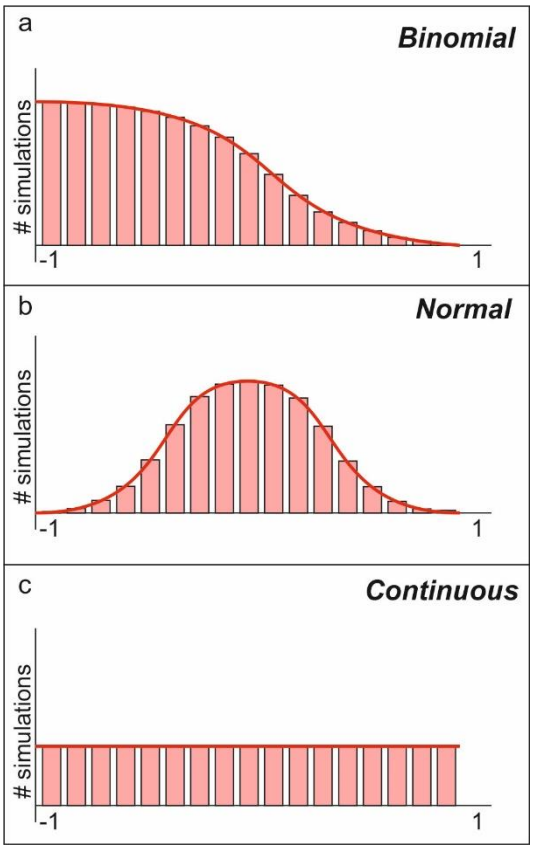

Figure 3.11: Distribution of the simulations in different approaches of a Monte Carlo distribution.

the other hand, if the variable refers to the river flow, the most appropriate distribution may be a normal distribution (Figure 3.11b). And, if we do not know how our variable relates to our environment, but we do know the range, it is best to make a continuous distribution of the variable (Figure 3.11c). The end result of this step will be a table with all the possible modeling combinations.

4th step: Running the simulations

This step involves pressing the button to start the model and crossing your fingers confident that everything will be fine. It's a good time to make a coffee break, go lunch or take a long nap, depending on the model duration.

5th step: Post processing and interpretation

Once the model is completed, it is necessary to observe that the results have coherence and significance to solve the inquiry considered in the 1st step. If they do not have it, the process must follow the 3rd step again, trying to correct the failure. Typically, modeling with this system involves multiple iterations before reaching a satisfactory result. This is because it is very difficult to deduce at the outset what effect will have the combination of all the variables.

To assess whether the results are satisfactory Dionisos can be integrated with Cougarflow, another software that allows to calculate the sensitivity of each parameter. The sensitivity of a parameter is the influence that modifying this parameter will have on the final result. The sum of the sensitivity of all variables must necessarily be 100%. In this case, if we want to solve an inverse problem from a direct model, the variables to be evaluated must have an equivalent sensitivity on the parameter that is compared with reality. To give an example, if we want to evaluate the importance of temperature and salinity in the formation of a nummulite bank, the variables temperature and salinity must have a similar sensitivity in order to be compared. If, for example, the temperature has a sensitivity of 95% and the salinity of 5%, then the geometry of the resulting nummulite facies distribution in each simulation will depend on 95% of the temperature, making it absurd to try to evaluate the weight that the salinity had.

Once the variables have reached a similar sensitivity, the parameter being evaluated (the geometry of the nummulite bank, in the previous case) must be compared with data obtained through direct measures, through conceptual modeling, or through another means. This comparison can be visual or it can also be assisted by equations that calculate errors and probabilities. An algorithm has been developed to make the

comparison by numerical means in the framework of this thesis and is explained in the results section.

3.3.3 Definitions

Here are precisely defined some words used in this manuscript as they can have a confusing meaning. Words contained on this glossary are highlighted in italics on the text.

Best Fit Simulation: From all the simulations on a model, this is the simulation closer to the data that we observe on the nature.

High Confidence Area: Area that we have used for all the numerical post processing and interpretations. As all the numerical models, this model have a deformation of the results near the boundaries due to the boundary effect. Also in this specific model we have done a prolongation of the basin downstream for accommodate the sediments that overflow the sedimentation area. The *High Confidence Area* is manually defined far enough from the boundaries and does not includes the overflown sediments. Interpretations of the data outside this area have to be taken with careful, as probably will led to an error.

Model: In this work, models are a representation of a specific aspect of the geology used for interpretation and quantification. As the modeling approach used is a Monte Carlo distribution of different forward models, specifically here models are all the experimental runs performed to solve a hypothesis and can contain one or more simulations.

Parameter: Are the outputted results of a model or simulation and are stored in a matrix. They define the environmental, geometrical and sedimentological characteristics of the results. Examples of parameters in this work are mean thickness, water flow, concentration of sand or bathymetry.

Simulation: The Monte Carlo models are divided on different simulations. Each simulation has a specific and fixed characteristics on the unknowns randomly defined.

Unknown: Input data that are the target of an inverse problem in our forward model.

4 RESULTS

The main results of this thesis include **two new magnetostratigraphic sections**, the Olsón section in the Ainsa basin and the Yebra de Basa section in the Jaca basin. They will be presented in the *Magnetostratigraphy* sub-section below. Age constrains provided by these sections have been added to the **analysis of the Tremp-Jaca basin sedimentation rates**, together with available data sorted from the literature. A correlation of all sections and decompaction by backstripping is presented in *Analysis of sedimentation rates in the Tremp-Jaca Basin* sub-section, which includes an analysis of sedimentation rates trends at both site level and basinwide. Finally, data obtained from the sedimentation rates analysis have been used to feed the **forward stratigraphic models** of the Tremp-Jaca basin; the Belsué model, in the Sierras Exteriores, and the General Flow Model in all the basin. In the models sub-section there is not only the formal results of those models but also the input data is described in detail. The model building itself must be considered part of the results of this thesis because of all the different decisions on the basin geometry and characteristics during the studied period that have been done.

4.1 Magnetostratigraphy

4.1.1 Olsón section

Olsón (*O Elsón* in Aragonese) is a village built on a hill located in the south of the municipality of Aínsa-Sobrarbe, following the road from Ligüerre de Cinca to Arcusa. The village is known for having a Gothic-Renaissance church known as the Sobrarbe Cathedral. Geologically, the village gives its name to multiple structures, as the Olsón anticline and the Olsón member in Escanilla formation. Here we have studied the Olsón section, with its base located in the lower part of the village and progresses south through the different ravines of the Serreta de San Benito (figure 4.1) (UTM 31T 26.3 km E, 468.5 km N).

The entire section and its laterally extensive outcrops are a magnificent exhibition of fluvial architecture and sedimentary structures, which not only allow a detailed study of the non-marine part of the Ainsa basin, but also permits to make cartographic correlations with submetric precision along the entire area. These fantastic exposure conditions have been studied on multiple occasions (Bentham, 1992; Labourdette, 2011; among others) and have served as inspiration to establish a classification of sequential

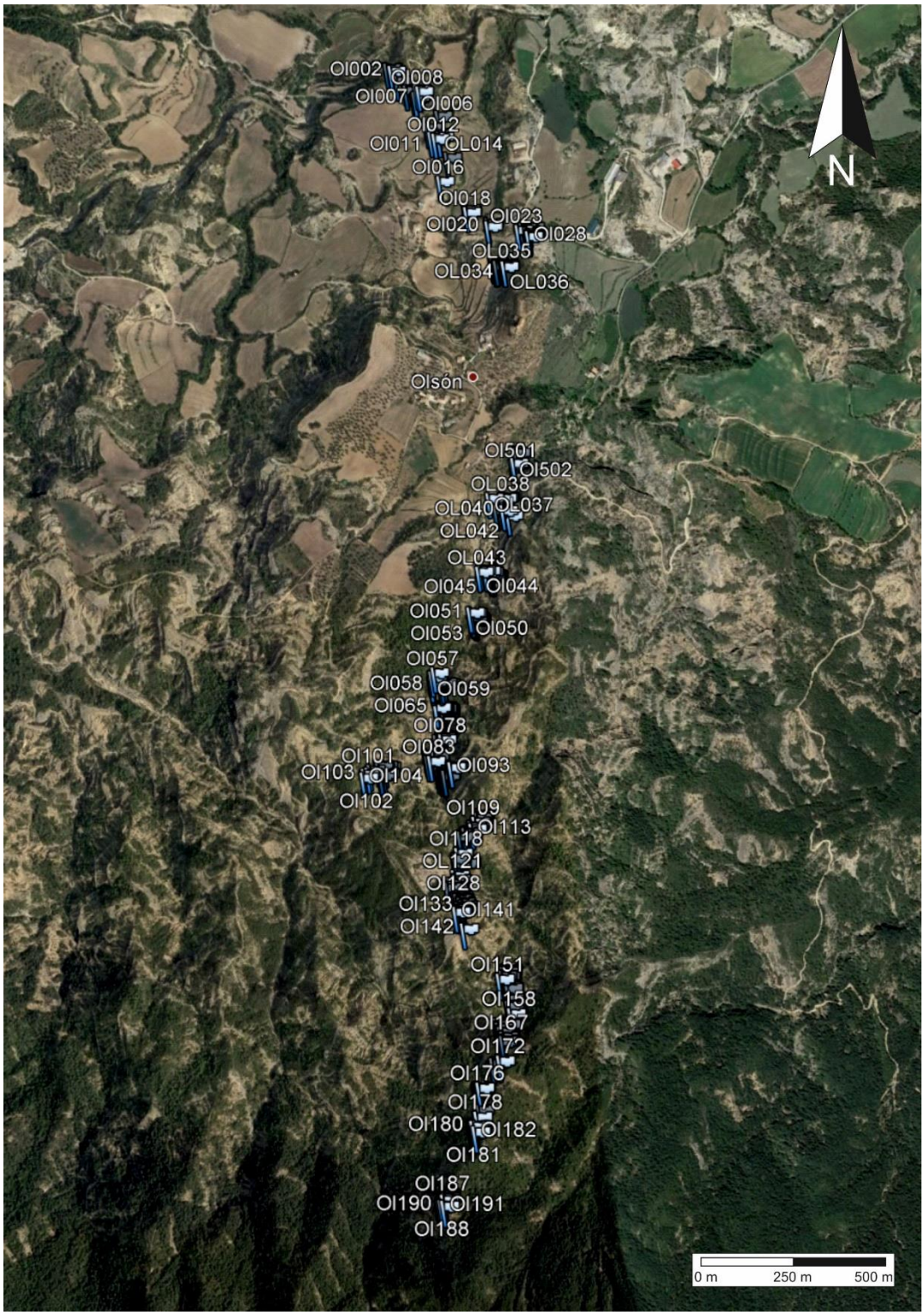

Figure 4.1: Position of the different samples of the Olsón section.

stratigraphy applied to non-marine sediments far from the coastline (Catuneanu, 2006 after Dahle *et al*., 1997).The relevance of these outcrops makes appropriate to carry out a dating with higher resolution in order to support finer correlations with sequences observed elsewhere and to understand the final stages of the Ainsa Basin infill. An earlier magnetostratigraphic

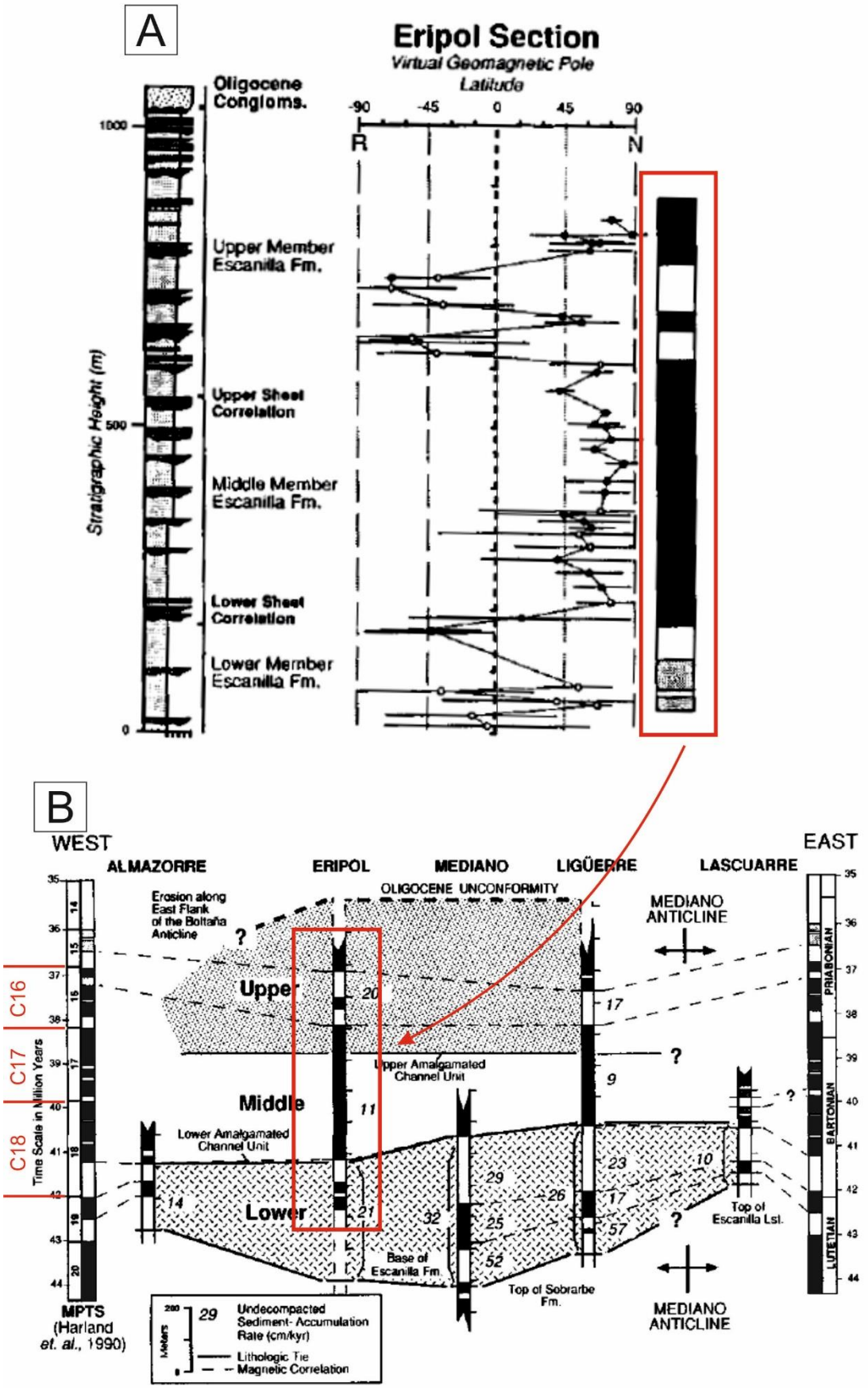

Figure 4.2: Eripol section from Bentham (1992) (A) Eripol section, VGP and inversions interpretation. (B) Correlation of the Eripol section with the GPTS. See that this correlation assumes that 3 chrons are in a normal magnetozone measured in Eripol.

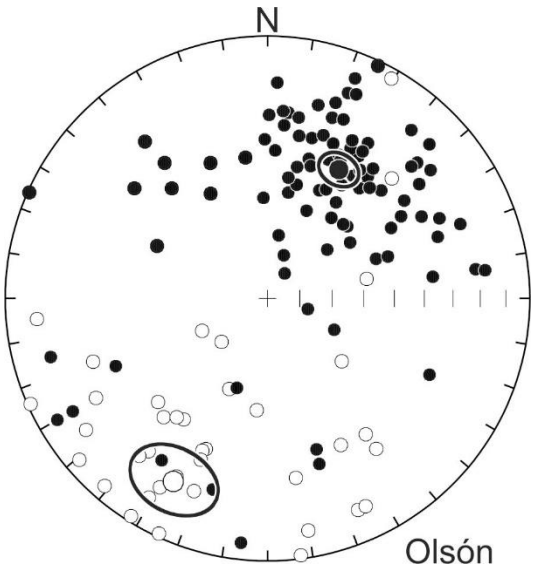

Figure 4.3: ChRM calculated from 70.1% of the total of the samples processed in the laboratory. The resulting mean direction of the Olsón section records a 30° clockwise rotation.

study close to the Olsón section was carried out in a ravine 1.5 km to the west, the Eripol section (figure 4.2) (Bentham, 1992). The Eripol sections was sampled at a relatively low resolution, with an average sampling space of *ca*. 20 m. A long normal magnetozone spanning the most part of the Eripol section was interpreted to correlate with chrons spanning from C18n to C16n (Bentham, 1992), therefore assuming that several polarity reversals were missed (figure 4.2).

The main purpose of the Olsón magnetostratigraphic section was to build a high resolution correlation by applying a sampling density high enough to ensure magnetostratigraphic completeness. Samples were collected at 3 m intervals. They were stepwise demagnetized in the UB-Geo3BCN paleomagnetism laboratory, mainly by TH and some by AF

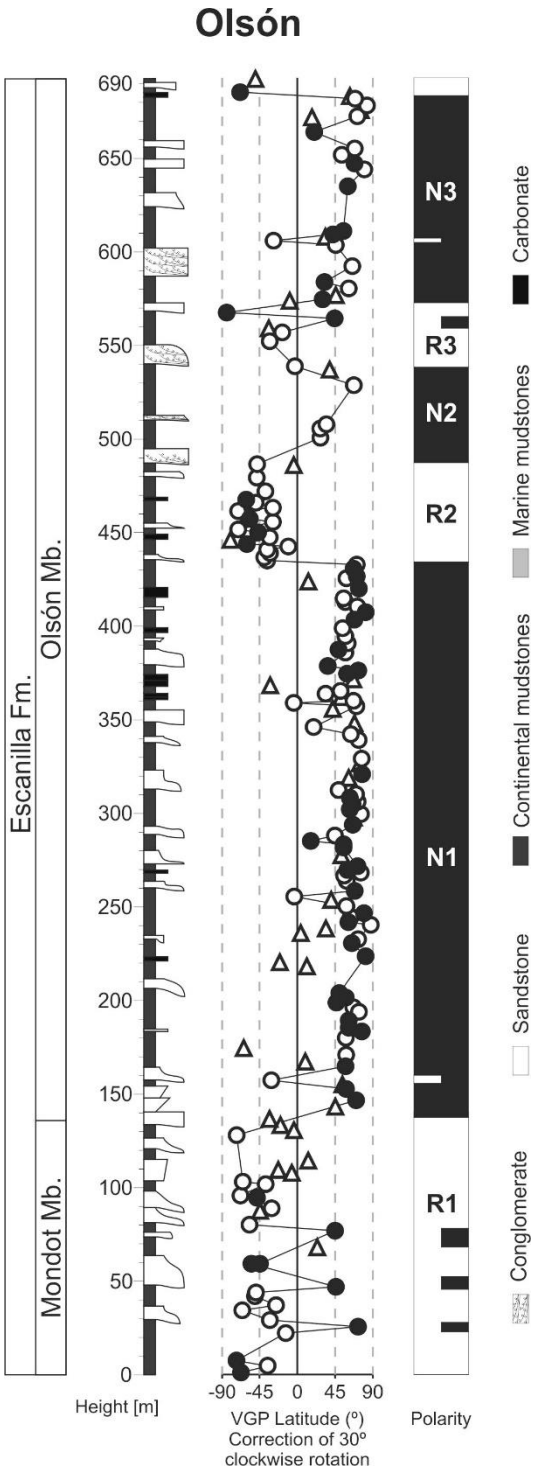

Figure 4.4: Olsón (Ainsa basin) magnetostratigraphic section. Black dots represent high-quality paleomagnetic directions and white dots represent intermediate quality. Triangles represent low-quality paleomagnetic directions. VGPs are corrected for a 30° clockwise rotation.

to test which of the two techniques was more appropriate (see digital suppl. data 1 for raw data).

ChRM directions were calculated from 70.1% of the total of the samples processed in the laboratory, and the results were aggregated in a stereographic projection. The resulting mean direction of the Olsón section records a 30° clockwise rotation (figure 4.3). Corrected paleomagnetic components at the time of deposition were obtained by

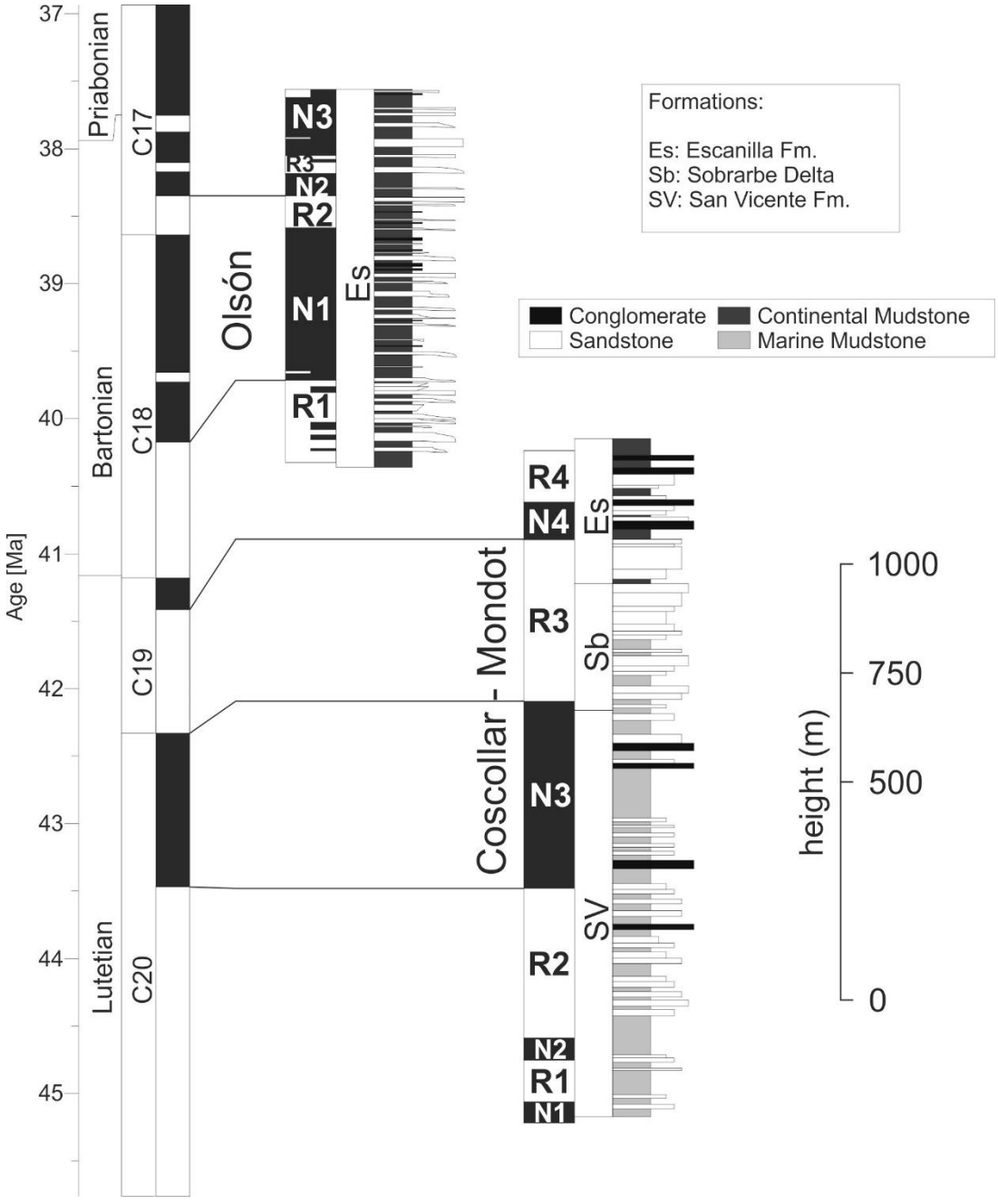

Figure 4.5: Magnetostratigraphic correlation of the new Olsón section with the GPTS (Gradstein *et al*., 2012), helped by the stratigraphic correlation with the Coscollar-Mondot sections (Mochales *et al*., 2012).

subtracting 30° to all ChRM azimuths. The latitude of the VGP was then calculated at sample level from each corrected ChRM paleomagnetic direction.

VGP latitudes were plotted against stratigraphic thickness in order to build a local magnetostratigraphy of the Olsón section. (figure 4.4). The new results revealed that missing reversals were not as many as interpreted earlier (figure 4.2), and that the Olsón section represents a time interval of shorter duration than presumed, spanning from C18r to C17n (figure 4.5). This correlation is coherent with the previous work done by Mochales *et al*. (2012), who dated the deep and deltaic marine strata underlying the Olsón section, attributing them to the Lutetian.

4.1.2 Yebra de Basa section

Yebra de Basa is a municipality of the region of the Alto Gállego located in the north shore of the Basa river (affluent of the Gállego) (UTM 30T 72.3 km E, 470.8 km N). This village is known by its church, where the relics of Santa Orosia are conserved. It is located 8 kilometers southeast of Sabiñánigo and 13 kilometers west of Fiscal, with which it has recently been connected by road through the Petralba and Berroy tunnels.

Geologically, Yebra de Basa is located at the northern limb of the Basa anticline, an east-west structure that crops out a beautiful shallowing-upwards sequence that records the transit from prodelta facies to the delta plain. This is widely known as the Sabiñánigo sandstone formation (Puigdefàbregas, 1975) and is followed by a widespread transgression that floods again the area returning it to the deep marine sedimentation. To the north of this sequence there is the Oturia thrust, isochronous to the sedimentation of the area and source area of an important part of the sediments contained therein (Roigé *et al*., 2016).

Previously, this area has been broadly studied due to the great importance of Sabiñánigo sandstone as an analogue of deltaic systems. There is a very complete thesis on Sabiñánigo sandstone made by Boya (2018), apart from other works by researchers from the *Universitat Autònoma de Barcelona*, such as the studies of provenance of Roigé (2018) and Roigé *et al*. (2016) or heavy mineral analyses, such as that of Coll *et al*. (2017). Moreover, the area had already been extensively studied in Puigdefàbregas (1975) and Remacha *et al*. (1987).

An earlier magnetostratigraphic study exists that spans the Yebra de Basa section (Hogan and Burbank, 1996). As in the case of Olsón, the sampling density was low (*ca*. 40 meters between sampling sites) and a single long normal magnetozone was interpreted to correlate with the sequence of chrons ranging from C18 to C16 of the

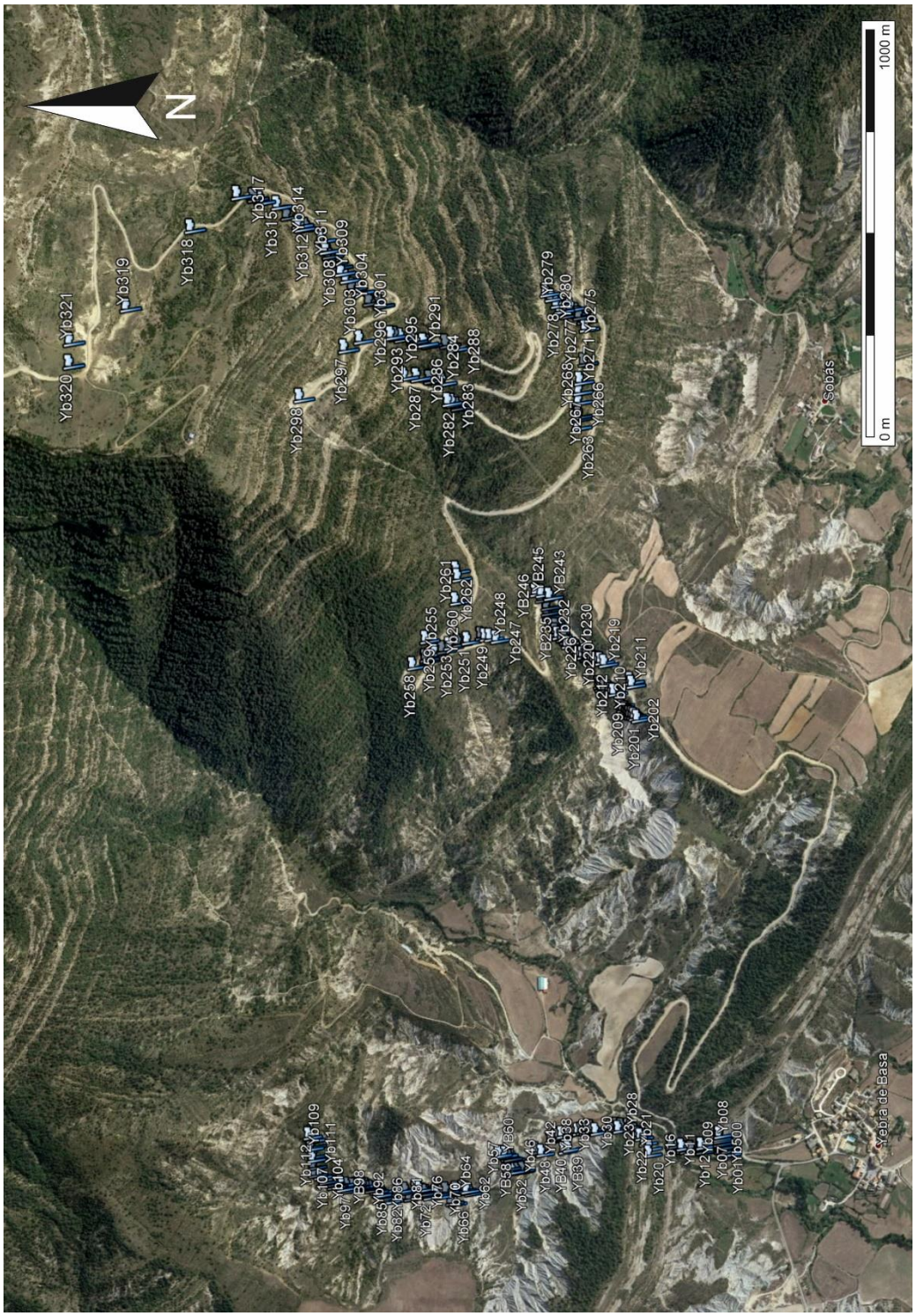

Figure 4.6: Position of the different samples of the Yebra de Basa section.

GPTS, therefore suggesting that several reversals were missed due to a sampling bias. In this study we aimed to test these conclusions by sampling a parallel section at higher density, with an average of a sample every 10 m (figure 4.6). Samples were demagnetized in the UB-Geo3BCN paleomagnetism laboratory by TH and some by AF to test which of the two techniques was more appropriate (see digital suppl. data 1 for raw data).

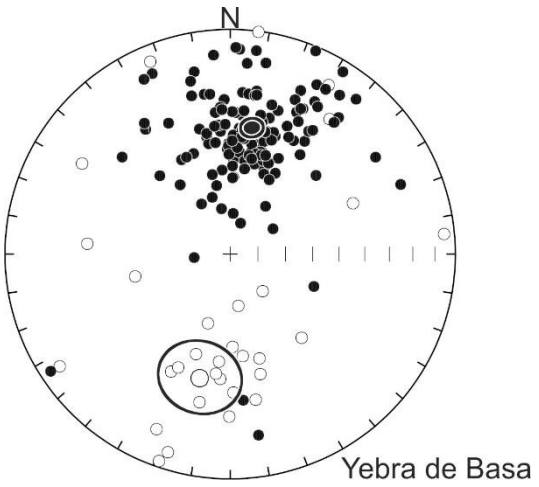

Figure 4.7: ChRM calculated from 75.1% of the total of the samples processed in the laboratory. The resulting mean direction of the Yebra de Basa section does not yield any significant vertical-axis rotation

Once calculated the ChRM directions and aggregated in a stereographic projection, the mean paleomagnetic vector does not show any significant vertical axis rotation (figure 4.7).

The log of VGP latitudes shows that there were no missing reversals in the earlier work of Hogan and Burbank (1996) (figure 4.8), despite their relatively low sampling resolution. Correlation of the Yebra de Basa has been re-interpreted according to the new results, correlating the overall section with chrons C18 and C17 (figure 4.9).

What reinforces the new dating and correlation with the GPTS is that the lower part of the section can be correlated with the uppermost units of the Gállego River and Aragón River sections by Oms *et al*. (2003). When all these sections are combined, the magnetic polarity pattern reveals characteristic and the new correlation with the GPTS is demonstrated (figure 4.9).

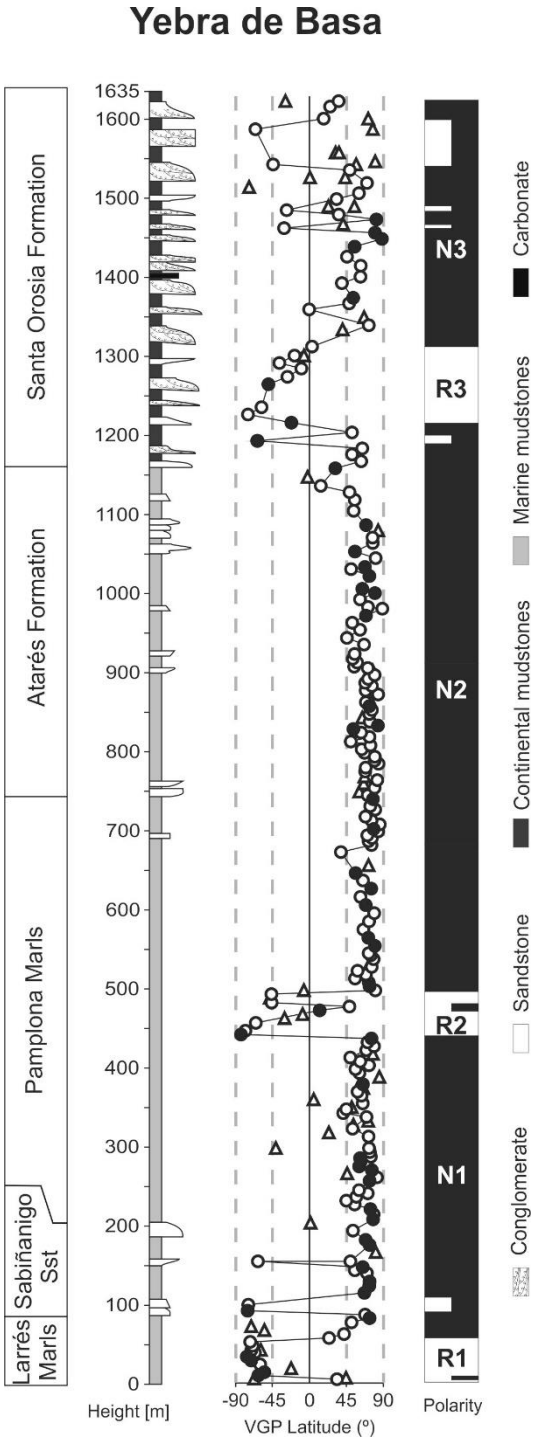

Figure 4.8: Yebra de Basa (Jaca Basin) magnetostratigraphic section. Black dots represent high-quality paleomagnetic directions and white dots represent intermediate quality. Triangles represent low-quality paleomagnetic directions.

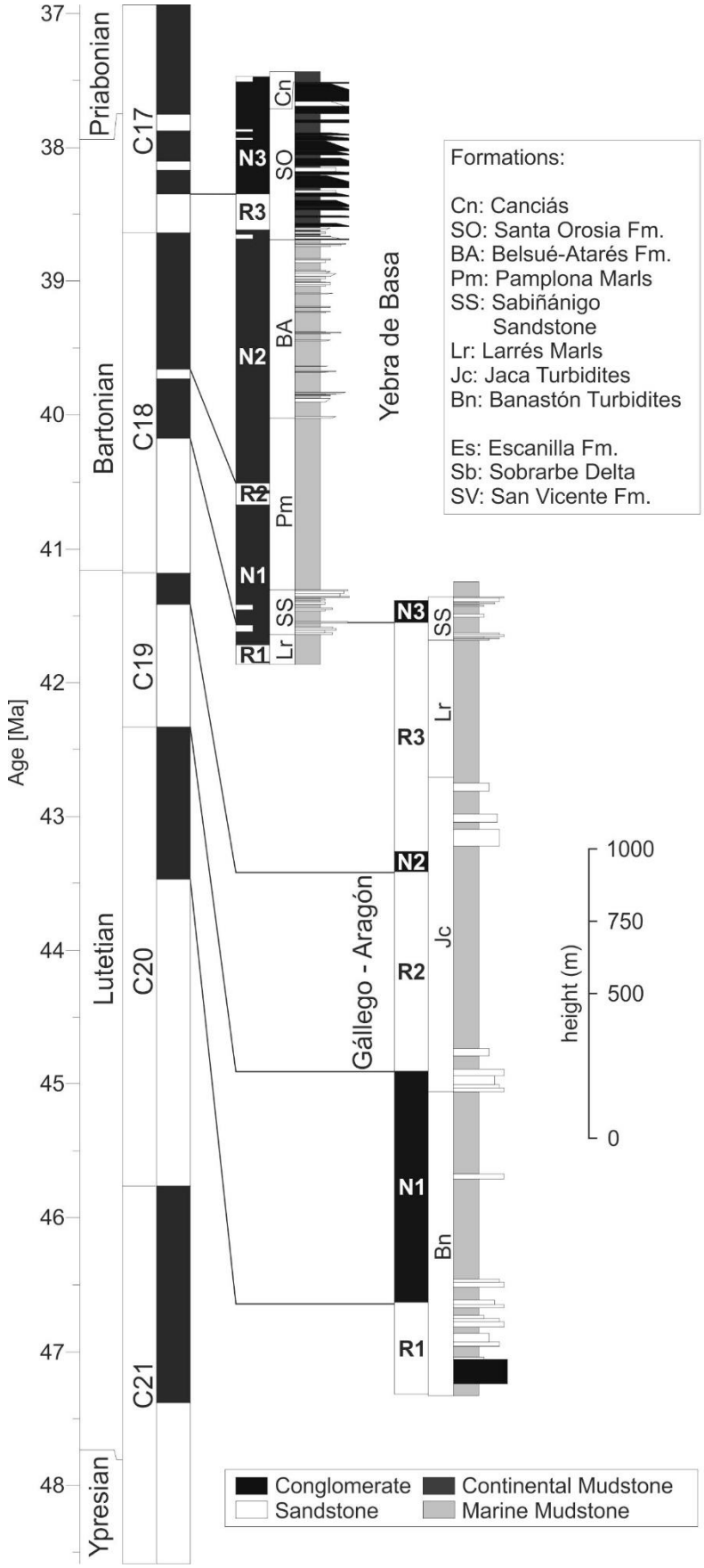

Figure 4.9: Magnetostratigraphic correlation of the new Yebra de Basa section with the GPTS (Gradstein *et al*., 2012), helped by the stratigraphic correlation with the Río Gállego/Río Aragón section (Oms *et al*., 2003).

4.1.3 Magnetostratigraphic correlation across the Tremp- Jaca basin

The two new sections of Olsón and Yebra de Basa have been correlated with different magnetostratigraphic sections along an almost east-west profile that is divided to the west into two branches (figure 4.10). The sections included in this panel are: Lascuarre (LS), Esera (ES) and Mediano (MD) from Bentham and Burbank (1996), Isuela (IS) (Rodríguez-Pintó *et al*., 2012b), Santa Marina (SM) (Rodríguez-Pintó *et al*., 2012a), Coscollar and Mondot (CM) (Mochales *et al*., 2012), Río Aragón / Río Gállego (GA) (Oms *et al*., 2003), Pobla de Segur (PS) (Beamud *et al*., 2003) and Belsué (BL) (Garcés *et al*., 2014).

Other sections in this area have also been considered, but have finally been excluded by meeting one or more of the following exclusion criteria (table 4.1):

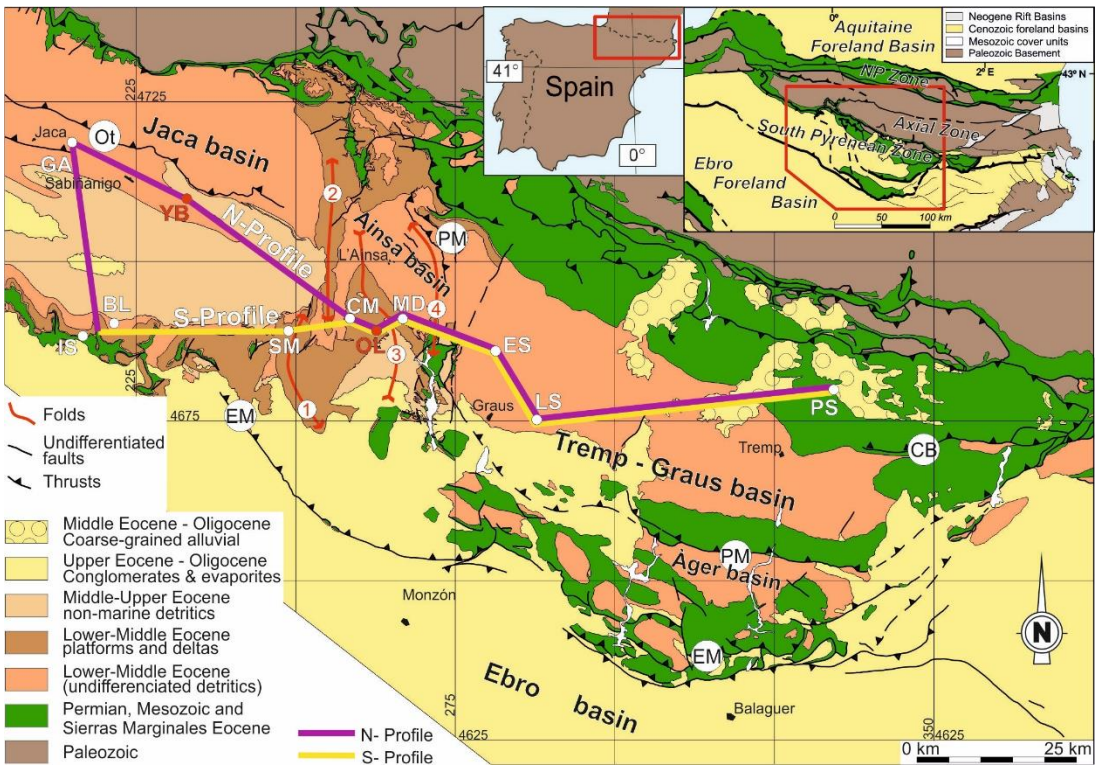

Figure 4.10: Geological setting of the South-central Pyrenees. (a) Geological maps with the location of the main structures, basins, studied sections and figure 4.13 and 4.14 profiles. Thrust Sheets: CB: Cotiella-Boixols; PM: Peña Montañesa-Montsec; EM: Sierras Exteriores-Serres Marginals. Thrust: Ot: Oturia thrust. Folds: 1: Balzes; 2: Boltaña; 3: Buil 4: Mediano. Sections: GA: Río Gállego-Río Aragón; YB: Yebra de Basa; IS: Isuela; BL: Belsué; SM: Santa Marina; CM: Coscollar-Mondot; MD: Mediano; OL: Olsón; ES: Ésera; LS: Lascuarre; PS: Pobla de Segur. The new sampled sections (Olsón and Yebra de Basa) are marked in red. This map was modified from the compilation made by Fernández-Bellón (2004) from published 1:50,000, 1:100,000 and 1:200,000 scale maps, and Muñoz *et al*. (2018).

Magnetostratigraphic section	*Reference*	*1*	*2*	*3*	*4*
Pobla de Segur (PS)	Beamud *et al.*, 2003				
Sis	Beamud *et al.*, 2003				X
Roda	Bentham and Burbank, 1996	X			
Esplans	Bentham and Burbank, 1996	X			
Lascuarre (LS)	Bentham, 1992				
Esera (ES)	Bentham, 1992				
Mediano (MD)	Bentham, 1992				
Eripol	Bentham, 1992	X	X		
Almazorre	Bentham, 1992	X			X
Liguerre	Bentham, 1992		X		
Belsué (BL)	Garcés *et al.*, 2014				
Salinas	Hogan and Burbank, 1996			X	
Arguís/Monrepós	Hogan and Burbank, 1996				X
Yebra de Basa	Hogan and Burbank, 1996		X		
San Felices	Hogan and Burbank, 1996				X
Agüero	Hogan and Burbank, 1996				X
Ayerbe	Hogan and Burbank, 1996				X
Arguís/Pico del Águila	Kodama *et al.*, 2010				X
Mondot (CM)	Mochales *et al.*, 2012				
Coscollar (CM)	Mochales *et al.*, 2012				
Río Gállego/Río Aragón (GA)	Oms *et al.*, 2003				
Santa Marina (SM)	Rodríguez-Pintó *et al.*, 2012 (a)				
Isuela (IS)	Rodríguez-Pintó *et al.*, 2012 (b)				
San Pelegrín	Rodríguez-Pintó *et al.*, 2013				X

Table 4.1: Relation of published magnetostratigraphic sections and the exclusion criteria marked with 'X'. (1) Average number of samples/magnetozones lower than 8. (2) Large number of magnetic reversals on the GPTS not found on the magnetostratigraphic section. (3) Data far-off from the studied profile. (4) Not the best section at a specific location, with respect to the overall quality of the data. The sections selected for this study are indicated in bold, see their location in figure 4.10.

1- Sections with an average number of samples/magnetozones lower than 8 were considered to have insufficient resolution (Johnson and McGee, 1983) and were then excluded.

2- Magnetostratigraphic sections that correlate with the Geomagnetic Polarity Time Scale (GPTS) by missing significant geomagnetic chrons were excluded.

3- To better capture the 2D geometry along the basin transects, data far-off from selected segments were ignored.

4- Where multiple sections were available, the above quality criteria were applied to select the best section for a specific location.

Cross-correlation between the above selected sections highlights a problem in the magnetostratigraphic interpretation of the Ésera section (Bentham and Burbank, 1996), particularly from its correlation with the Ainsa basin sections. The original magnetostratigraphic interpretation of the Ésera section (Bentham and Burbank, 1996) attributed the upper normal magnetozone (N3, figure 4.11) to the chron C20n, placing the Grustán limestone Formation (figure 1.7) within chron C19r. This is not consistent with the stratigraphic correlation of the Grustán limestone to the west. In Vinyoles *et al*. (2020) we propose to interpret the upper normal magnetozone of the Ésera section as either an artifact or a short geomagnetic event that is not yet identified in the GPTS, resulting in a correlation of the Grustán Formation with chron C20r (figure 4.11).

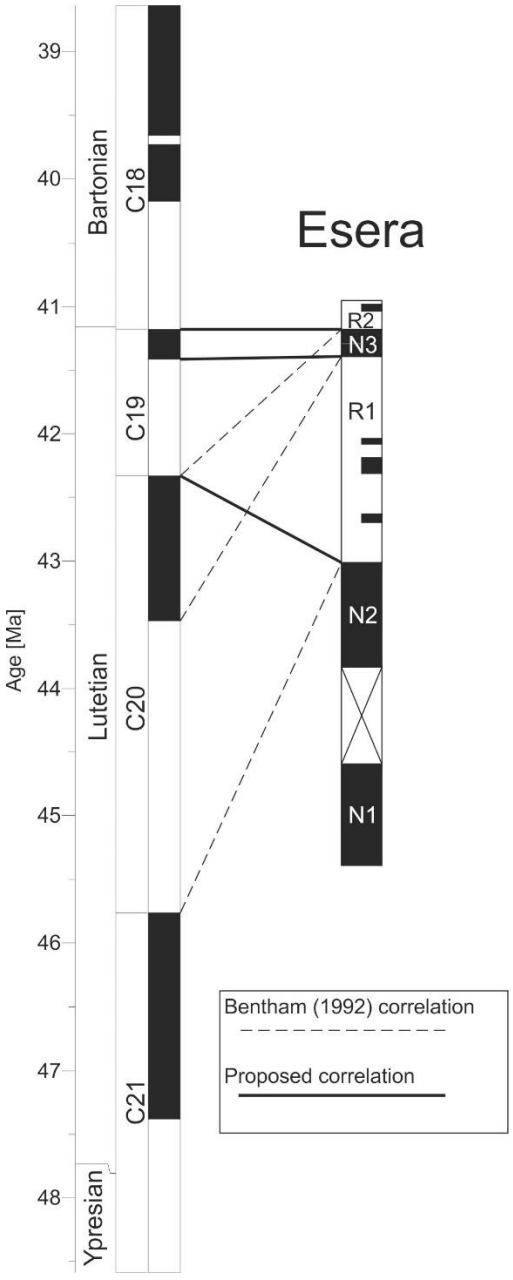

Figure 4.11: Original (Bentham, 1992) and discussed correlation of the Esera section. The new correlation corrects the age of the Esera section to the Grustan carbonate platform age.

4.2 Analysis of sedimentation rates in the Tremp-Jaca basin

All the sections selected for the correlation across the Tremp-Jaca basin (TJB) have their thicknesses corrected for sediment load compaction. For this purpose, an "extra" sedimentary unit (overburden) has been considered on top of each section to represents its estimated burial after deposition. The burial variability throughout the basin ranges from 210 m in La Pobla de Segur to more than 3000 m in the Isuela section (table 4.2). Decompaction has been performed by one-dimensional backstripping, following the methods described in Angevine *et al*. (1992). The present-day and decompacted thicknesses of each unit are listed in the table 4.3 and are explained on the section 4.2.1

Abbr.	*Section*	*Overburden thickness [m]*
BL	Belsué	2200
CM	Coscollar - Mondot	970
ES	Ésera	600
IS	Isuela	3100
LS	Lascuarre	300
MD	Mediano	470
OL	Olsón	300
PS	Pobla de Segur	210
SM	Santa Marina	3000
YB	Yebra de Basa	1200
GA	Gallego – Aragón	2800

Table 4.2: Overburden values for the studied sections. Values were obtained from Montes (2009), Beamud *et al*. (2011), and Rodríguez-Salgado *et al*. (2020).

4.2.1 Sedimentation rates in the Tremp-Jaca basin (from Vinyoles *et al*., 2020)

The average Sedimentation Rate (SR) of the complete stratigraphic interval yields long-term decompacted SR in the TJB that range from 8.93 cm/kyr in the PS log (Tremp-Graus) to 84.54 cm/kyr in the GA+YB composite log (Northern Jaca) both for a 6.5 Myr interval (table 4.3). Compacted SR for these logs are 8.27 cm/kyr and 53.25 cm/kyr respectively. All these values reasonably fit the range of 10 to >100 cm/kyr proposed for foreland basins in Einsele (2000).

Shorter term SR were calculated by decompacting sedimentary units from each magnetozone and dividing by their durations. The SR ranged from 3 to 170 cm/kyr, with average values between 30 and 40 cm/kyr (table 4.3). The SR trend for each log is shown in figure 4.12 for both compacted and decompacted thicknesses. Some of these diagrams (*e.g.*, Mediano (MD), Santa Marina (SM)) roughly depict an increasing then decreasing trend that is typical for a foreland basin infill (Figure 1.4e). Other logs only show increasing (Río Aragón/Gállego (GA), Isuela (IS), Coscollar/Mondot (CM)) or decreasing SR (Olsón (OL), Yebra de Basa (YB), Lascuarre (LS)), because these only

Area	Sect.	Magnetozone	duration (Myr)	Original thickness (m)	decompacted thickness (m)	decompact. SR (cm/kyr)	orig. mean SR (cm/kyr)		decom. mean SR (cm/kyr)	
Southern Jaca basin	Belsué	Overburden	-	2200	-	-	15.39	11.04	23.06	17.17
		C16n	0.994	>189.00	>293.83	>29.56				
		C16r	0.269	98.50	150.21	55.84				
		C17n1n	0.816	67.90	93.49	11.46				
		C17n3 + C17n1r	0.595	138.60	205.00	34.45				
		C17r	0.288	46.00	65.19	22.64				
		C18n.1n	1.018	156.80	215.75	21.19				
		C18n2n+C18n1r	0.515	106.30	186.06	36.13				
		C18r	1	78.90	122.95	9.94				
	Isuela	Overburden	-	3100	-	-	6.45		11.49	
		C19n	0.234	>49.59	>97.85	>41.82				
		C19r	0.913	128.5	226.66	24.83				
		C20n	1.154	156.38	278.32	24.12				
		C20r	2.437	88.75	163.01	6.69				
		C21n	1.895	39.42	67.42	3.56				
		C21r	1.265	>27.72	>51.05	>4.04				
	Santa Marina	Overburden	-	3000	-	-	8.99		15.88	
		C19n	0.234	29.11	54.14	23.14				
		C19r	0.913	278.86	458.14	50.18				
		C20n	1.154	105.02	195.80	16.97				
		C20r	2.437	153.82	288.69	11.85				
		C21n	1.895	29.41	56.40	2.98				
		C21r	1.265	>29.78	>60.41	>4.78				
Ainsa basin	Coscollar - Mondot	Overburden	-	970	-	-	14.57	16.27	20.67	21.53
		C18r	1.003	>80.00	>104.17	>10.39				
		C19n	0.234	71.00	93.57	39.99				
		C19r	0.913	314.00	411.34	45.05				
		C20n	1.154	359.00	500.36	43.36				
		C20r	2.437	284.00	425.94	17.48				
		C21n	1.895	44.00	72.47	3.82				
		C21r	1.265	79.00	129.11	10.21				
	Olsón	Overburden	-	300	-	-	20.36		23.59	
		C17n2r + C17n1r	0.277	31.50	34.63	15.26				
		C17n3n	0.178	50.00	55.68	31.28				
		C17r	0.288	53.00	61.30	21.29				
		C18n	1.533	296.80	332.26	21.67				
		C18r	1.003	236.20	289.76	28.89				
	Mediano	Overburden	-	470	-	-	19.03	23.37	25.20	30.09
		C18n	1.533	>104.71	>120.37	>7.85				
		C18r	1.003	247.17	285.51	28.47				
		C19n	0.234	96.39	119.57	51.10				
		C19r	0.913	171.73	216.01	23.66				
		C20n	1.154	600.45	786.98	68.20				
		C20r	2.437	337.76	516.31	21.19				
		C21n	1.895	>135.10	>224.50	>11.85				

Table 4.3: SR for the studied sections including decompacted SR for each significant magnetozone and average original (compacted) and decompacted SR for each section or successive pair of sections. Continued on the next page.

represent a portion of the whole succession at the site, so the complete vertical trend is not recorded. To avoid this incomplete view, and assisted by the magnetostratigraphic framework, we assembled two composite correlation panels comprising the whole stratigraphic succession: The N-profile and the S-profile, showing the vertical and

Area	Sect.	Magnetozone	duration (Myr)	Original thickness (m)	decompacted thickness (m)	decompact. SR (cm/kyr)	orig. mean SR (cm/kyr)		decom. mean SR (cm/kyr)	
Tremp-Graus basin	Esera	Overburden	-	600	-	-	21.00		25.62	
		C20r	2.437	>469.87	>557.82	>22.89				
		C21n	1.895	>439.72	>552.03	>29.31				
	Lascuarre	Overburden	-	300	-	-	8.67		9.83	
		C17r	0.288	29.65	31.51	10.94				
		C18n	1.533	89.73	96.84	6.32				
		C18r	1.003	105.78	122.63	12.23				
		C19n	0.234	39.89	49.47	21.14				
	Pobla de Segur	Overburden	-	210	-	-	8.27		8.93	
		C15n	0.295	41.65	43.34	14.69				
		C18n + C15r	4.907	205.23	214.60	4.37				
		C19n + C18r	1.237	285.83	317.37	9.61				
Northern Jaca basin	Yebra de Basa	Overburden	-	1200	-	-	48.95	53.25	72.49	84.54
		C17n	1.411	322.00	432.65	30.66				
		C17r	0.288	100.00	153.86	53.42				
		C18n.1n	1.018	708.00	1003.04	98.53				
		C18n.1r	0.07	61.00	118.86	169.80				
		C18n.2n	0.445	391.00	634.45	142.57				
		C18r	1.003	>53	>107.43	>10.71				
	Río Gallego - Río Aragón	Overburden	-	2800	-	-	57.46		96.33	
		C18r	1.003	637.12	1058.07	105.49				
		C19n	0.234	57.83	123.53	52.79				
		C19r	0.913	557.85	920.26	100.80				
		C20n	1.154	645.56	1080.84	93.66				
		C20r	2.437	>256.54	>456.05	>18.71				

Table 4.3 (continued)

horizontal evolution of the SR (figure 4.13b). The panels cover four different basin domains or subbasins: Tremp-Graus, Ainsa, Southern Jaca, and Northern Jaca.

In the Tremp-Graus area (Pobla de Segur (PS), Lascuarre (LS), and Ésera (ES) sections) SR can be higher than 29 cm/kyr (but approximately 15 cm/kyr on average). For a proximal-distal profile (Pobla de Segur (PS)-Lascuarre (LS)), we observe a slight increase in SR towards the distal part (table 4.3 and figure 4.13).

The Ainsa area (Mediano (MD), Olsón (OL), and Coscollar/Mondot (CM) sections) shows a wide range of SR (in time and space) for most of the Lutetian, reaching maximum values of 68 cm/kyr, minima close 4 cm/kyr, and average values near 45 cm/kyr. During the Bartonian and Priabonian SR are moderate, close to 20 cm/kyr on average. The general vertical trend is of increasing SR during the Lutetian, followed by a progressive decrease during the Bartonian, to minimum SR at the top of the succession.

The Northern Jaca area (Yebra de Basa (YB) and Río Aragón/Gállego (GA) sections) shows very high SR for most of the succession, with an average of 85 cm/kyr and maximum values of up to 170 cm/kyr (C18n.1r, Yebra de Basa (YB) section). The initially high SR (more than 90 cm/kyr) are punctuated by a transient decrease to 53 cm/kyr at

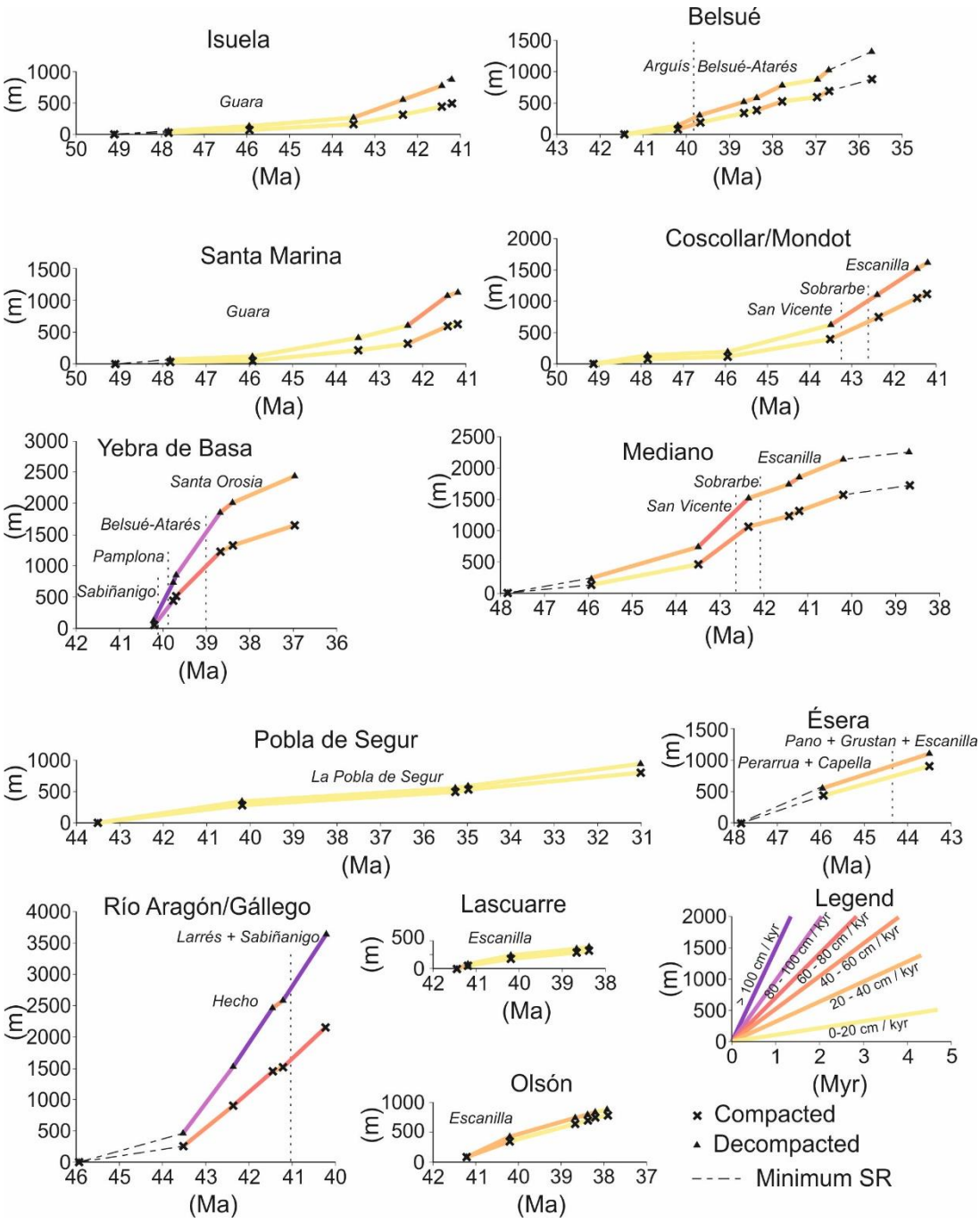

Figure 4.12: Compacted and decompacted SR diagrams for each of the studied sections in this work, including references to the stratigraphic units and formations. The vertical axis is stratigraphic height in meters and the horizontal axis is the age, in Ma. Segments are colored according to their SR following the color legend in figure 4.13.

the end of Lutetian, later recovering the high values to a maximum (170 cm/kyr) during the middle Bartonian and followed by a progressive decrease in the Bartonian-Priabonian.

The Southern Jaca area (Isuela (IS), Belsué (BL), and Santa Marina (SM) sections) depicts low to moderate SR (in most cases below 40 cm/kyr). As for Ainsa, they depict

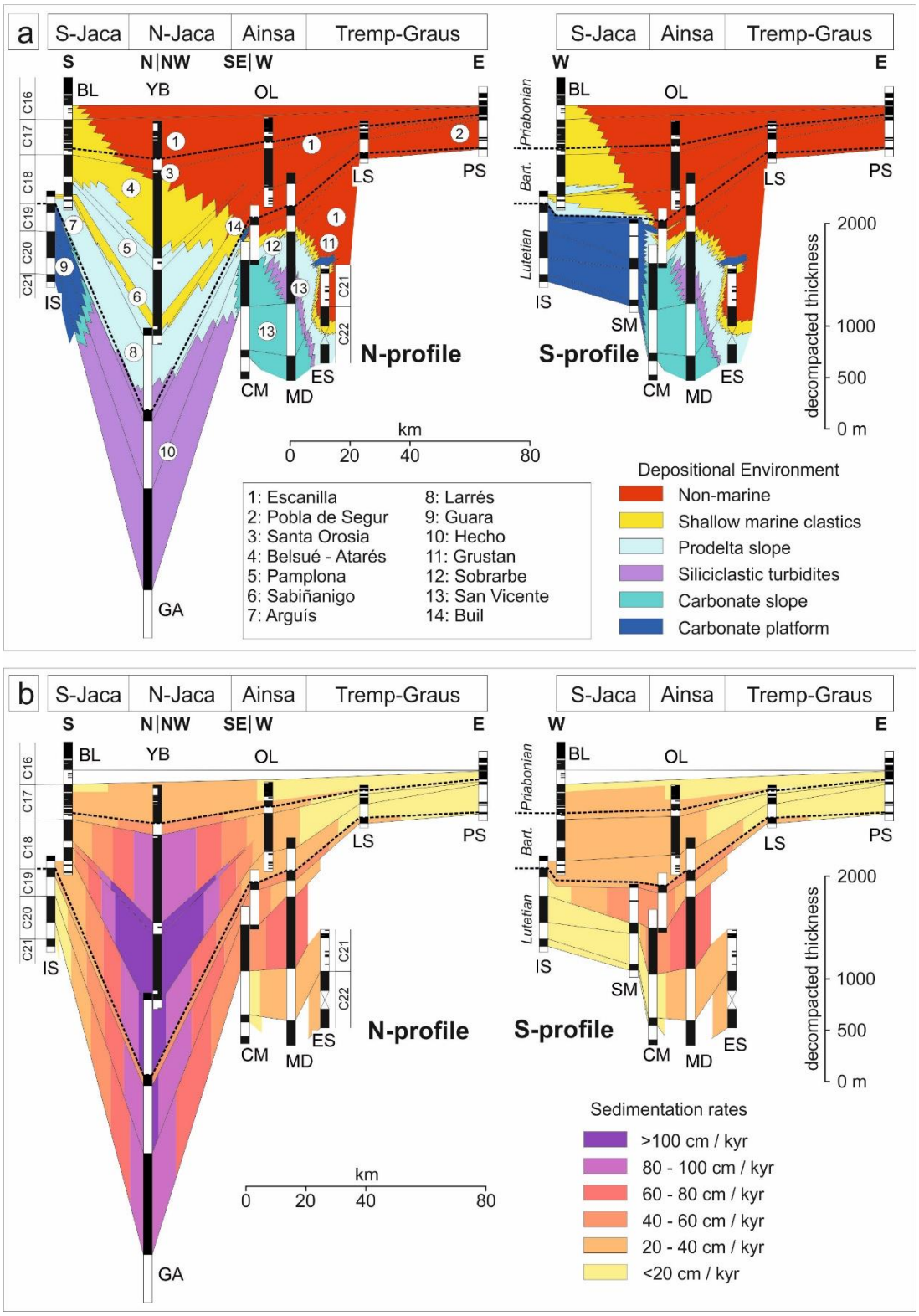

Figure 4.13: Correlation among the Tremp, Ainsa and Jaca sub-basins through the N-Profile and the S-Profile showing: (a) the main depositional environments, and (b) the lateral and vertical SR variations through the studied sections. Location of the profiles and sections is shown in figure 4.10.

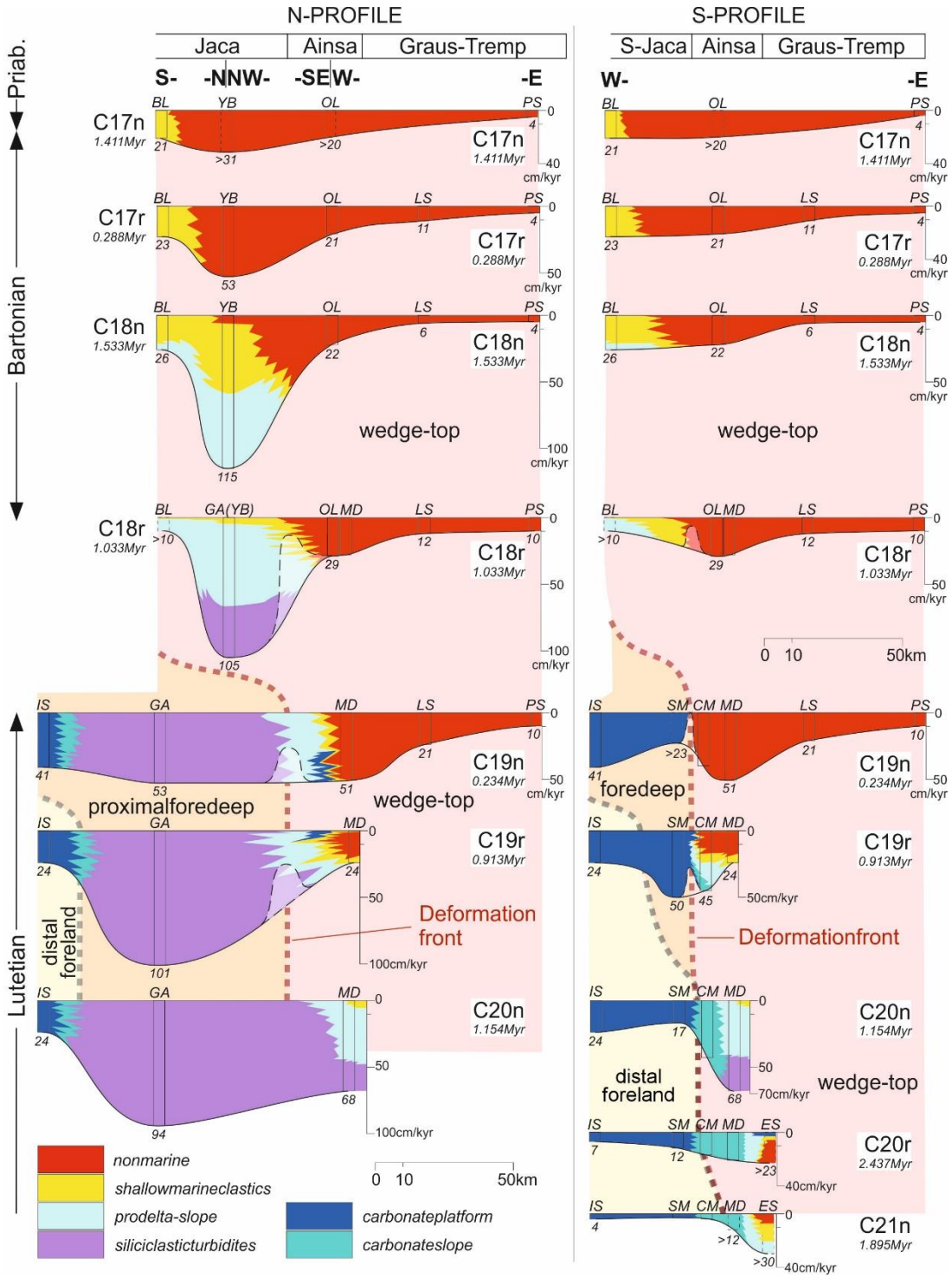

Figure 4.14: Evolution of decompacted SR across the Tremp–Jaca basin over time following the N-Profile and the S-Profile. 16 Graphs show SR variation for each time-slice (magnetostratigraphic chron) and distribution of the main facies belts. Vertical scale: SR in cm/kyr; horizontal scale: distance in km. Absolute ages from GPTS (Gradstein *et al*., 2012). Individual SR for each log are indicated. Background colors represent the attribution of the logs to the different depozones. The logs used are: BL, Belsué; IS, Isuela; SM, Santa Marina; GA, Gállego-Aragón; YB, Yebra de Basa; OL, Olsón; CM, Coscollar-Mondot; MD, Mediano; ES, Ésera; LS, Lascuarre; PS, Pobla de Segur. Dashed logs and SR curves indicate minimum values due to incomplete logs. Duration of each magnetozone is indicated in Myr. The SR graphs have been produced from the data obtained on the studied logs. Only variations related to Boltaña and Balzes anticline growth have been inferred since these structures have an important role on SR evolution and distribution.

an initial increase in SR (from 3 to 50 cm/kyr) during the Lutetian. During Bartonian values range between 10 and 56 cm/kyr with no clear general trend when considering short magnetozones.

Decompacted SR in figure 4.13 were calculated for every single magnetozone identified in the magnetostratigraphic logs. In the following analysis, short magnetozones were combined (table 4.3 and figure 4.14) in order to lower the errors in SR related to uncertainties in the location of the magnetozone boundaries. The N-profile (figure 4.13) shows a progressive increase of SR from proximal (Tremp-Graus) to the distal area (Northern Jaca), where a persistent major depocenter is established. From the Northern Jaca depocenter a southward decrease in SR is observed (figure 4.14). The Northern Jaca depocenter is characterized by the sedimentation of thick deep marine facies, whereas on the Tremp-Graus, Ainsa, and Southern Jaca alluvial, shallow marine and submarine slope facies are dominant. The last stages of evolution (uppermost Bartonian and Priabonian, 38.4 to 37.0 Ma) evidence a uniformization trend of SR in the Ainsa and Jaca basins.

The S-profile shows the development of a depocenter in the Ésera section (Tremp-Graus basin) during the early Lutetian (47.8 – 43.5 Ma) (figure 4.14, C21n and C20r). Later (figure 4.14, from C20n to C18r), the depocenter migrated to the Ainsa area for most of the Lutetian and the lowermost Bartonian (43.5 - 40.2 Ma). This depocenter reveals abrupt changes in SR across short spatial distances. In the final stage (40.2 – 36.9 Ma) (figure 4.14, from C18n to C17n) SR become more uniform in Ainsa and Southern Jaca like those observed in the N-Profile.

Integrating the N- and S-profiles in map view (figure 4.15) we observe that the main depocenters (Northern Jaca and Ainsa in figure 4.14) are part of the same sedimentary trough. The N-profile lies aligned with the sedimentary trough axis, whereas the S-profile cuts across it (figures 4.14 and 4.15). Thus, since maximum SR (depocenter) are obtained in Northern Jaca, we will refer to the region of maximum SR in the S-Profile as a relative depocenter.

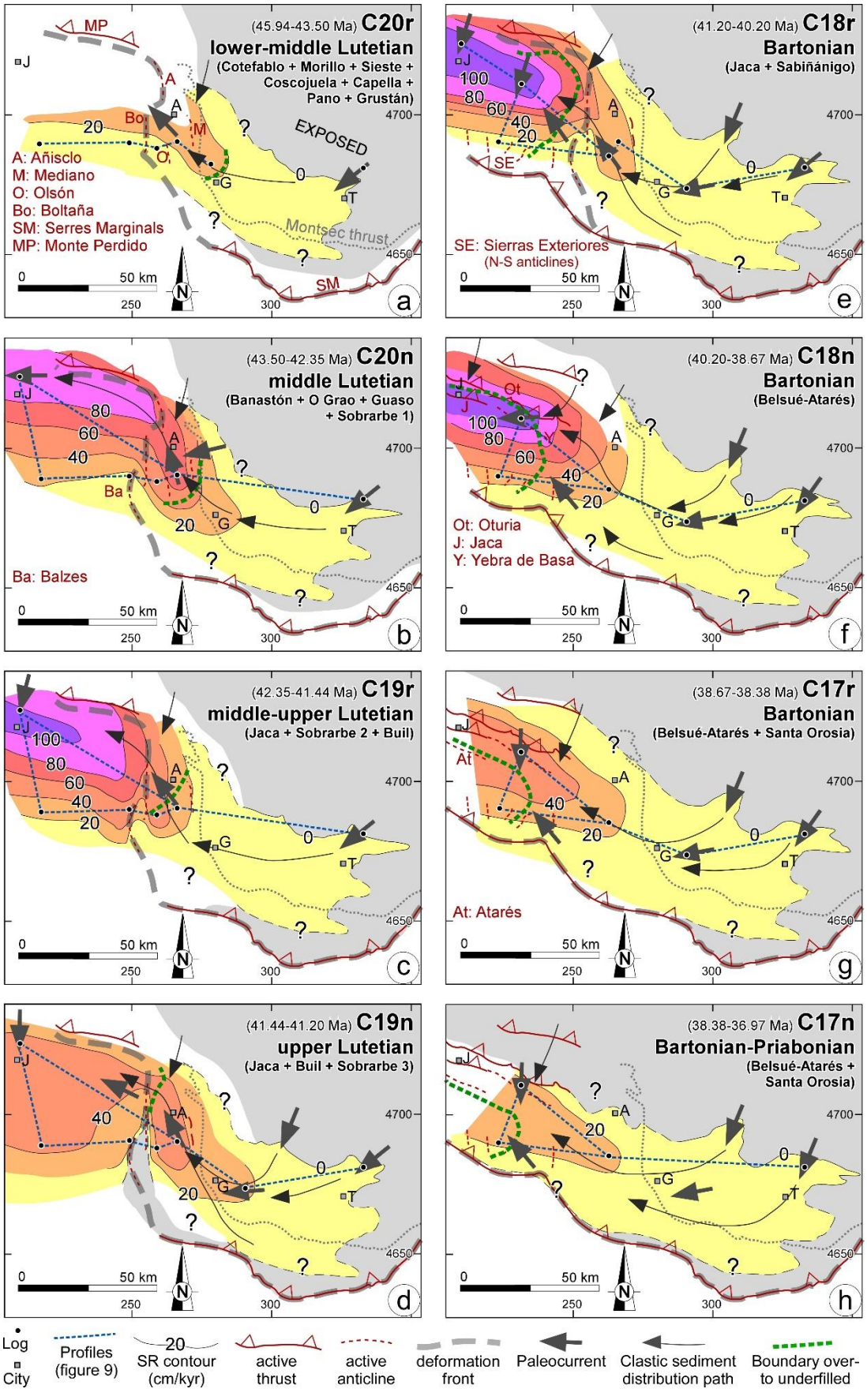
(45.94-43.50 Ma) C20r
lower-middle Lutetian
(Cotefablo + Morillo + Sieste + Coscojuela + Capella + Pano + Grustán)
A: Añisclo
M: Mediano
O: Olsón
Bo: Boltaña
SM: Serres Marginals
MP: Monte Perdido
EXPOSED
Montsec thrust
(41.20-40.20 Ma) C18r
Bartonian
(Jaca + Sabiñánigo)
SE: Sierras Exteriores
(N-S anticlines)
(43.50-42.35 Ma) C20n
middle Lutetian
(Banastón + O Grao + Guaso + Sobrarbe 1)
Ba: Balzes
(40.20-38.67 Ma) C18n
Bartonian
(Belsué-Atarés)
Ot: Oturia
J: Jaca
Y: Yebra de Basa
(42.35-41.44 Ma) C19r
middle-upper Lutetian
(Jaca + Sobrarbe 2 + Buil)
(38.67-38.38 Ma) C17r
Bartonian
(Belsué-Atarés + Santa Orosia)
At: Atarés
(41.44-41.20 Ma) C19n
upper Lutetian
(Jaca + Buil + Sobrarbe 3)
(38.38-36.97 Ma) C17n
Bartonian-Priabonian
(Belsué-Atarés + Santa Orosia)
0
50 km
250
300
4700
4650
N
a
b
c
d
e
f
g
h
Log
City
Profiles (figure 9)
20
SR contour (cm/kyr)
active thrust
active anticline
deformation front
Paleocurrent
Clastic sediment distribution path
Boundary over-to underfilled

Figure 4.15: Map view evolution of SR across the TJB over time. Each time step corresponds to a different chron as shown in figure 4.14. Coordinates are in km in the UTM reference system. This map shows the present-day location of structures and logs and the trace of figure 4.14 profiles through the logs considered for each chron. Absolute ages from GPTS (Gradstein *et al*., 2012). The shortening related to thrust advance and clockwise synsedimentary rotation of the Ainsa Basin and External sierras structures has not been taken into account (Palinspastic reconstruction is not considered). The Montsec-Peña Montañesa thrust has been used as a reference since it was not an active structure during the studied interval. Palaeocurrent data from Puigdefàbregas (1975); Vincent (2001); Barsó (2007); Arbués *et al*. (2011); Michael *et al*. (2014); Roigé *et al*. (2016), and our own data. J: Jaca, A: Ainsa, G: Graus, T: Tremp. SR variations related to anticline growth have not been inferred except Boltaña and Balzes folds due to their influence on clastic sediment routing. Cotefablo, Banastón and Jaca are turbidite systems of the Hecho group in the Jaca basin (Mutti *et al*., 1985; Labaume *et al*., 1987). Morillo, Coscojuela, Gabardilla, O Grao and Guaso are turbidite systems in the San Vicente Formation in the northern Ainsa Basin (Arbués *et al*., 2011; Muñoz *et al*., 2013). Sobrarbe 1: Deltaics older than San Lino horizon (Arbués *et al*., 2011) in Ainsa; Sobrarbe 2: Sobrarbe Deltaic Complex below Buil nummulite banks; Sobrarbe 3: Sobrarbe Deltaic Complex above Buil nummulite banks.

4.3 Models

The original interest of this thesis, in the framework of modeling, was to make a general model of the South-Pyrenean basins where the source to sink sedimentary and stratigraphic evolution could be studied. But after many failed models trying to reach this goal, I have decided to change the initial question into two simpler and more specific objectives that address key questions on the Pyrenees:

1. Do Milankovitch cycles propagate from the source area to the basin (propagation from the downstream) or from the basin to the source area (propagation from the upstream)?
2. Which are the clastic sedimentary routes in the South Pyrenean foreland basins during the Upper-Middle Eocene?

Two different models have been developed to answer these two questions. The first one is called "Belsué model". The second is the "General Flow Model (GFM)"

4.3.1 Belsué model

1st step: The inquiry

The Belsué model is designed to solve this specific question: **The Milankovitch climatic signal in the Belsué-Atarés delta is propagated from the downstream (sink to source) or from the upstream (source to sink)?** (figure 4.16)

Specifically, the inquiry is applied to the shallow marine Eocene succession in Belsué syncline (figure 4.17). There it is developed a delta sequence with a delta front part

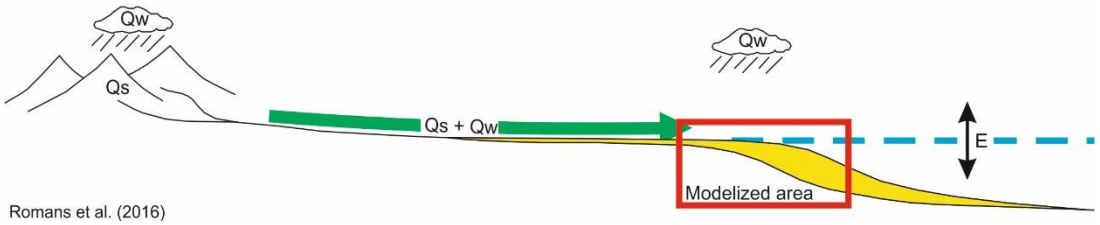

Figure 4.16: Target of the modeling. Sediments came with a cyclicity acquired on the upstream portion of the Sediment Routing System and arrived to the basin, were found a cyclicity controlled by the downstream portion. Redrawn from Romans *et al*. (2016).

corresponding to the Belsué-Atarés formation, a sandy formation of centimetric to metric strata highly bioturbated interbedded with a marly fraction. The prodelta is represented by the Arguís formation, a marly formation with some centimetric sandstones and limestones interbedded. Paleocurrents of this area show an overall northwest direction.

The Belsué syncline is located on the southern part of the Jaca Basin, close to the Sierras Exteriores (figure 4.10), between the Pico del Águila anticline (to the west) and Gabardiella anticline (to the east). The Belsué syncline has the particularity of being filled with syntectonic sediments, so the long-term cycles registered there are driven by the local tectonic evolution of the area (Millan *et al*., 1994). Shorter-term cycles were associated to regional relative sea-level changes (Castelltort et al., 2003), either related to eustasy or to foreland basin subsidence. Garcés *et al*. (2014) and Valero *et al*. (in prep.) show that the tectonic trends are overlapped by higher frequency orbital cycles. Specifically, there are Milankovitch eccentricity cycles of 405 kyr frequency, and also there is the imprint of the minima of 2.4 Myr and nodes of obliquity of 1.2 Myr (Valero *et al*., in prep.). Similarly, Kodama *et al*. (2010) found orbital cycles in the neighboring Arguís syncline, westwards of the Belsué syncline. There, magnetic susceptibility also shows the Milankovitch of 405 kyr, in addition to the 100 kyr eccentricity cycles (Kodama *et al*., 2010).

2nd step: The calibration model

In this section are defined the boundary conditions of the *model*. To define them it has been given priority to the conditions that can be directly measured. In case that the direct measurements were not possible, they were taken from previous works in the literature. Finally, those that were not available, were estimated based on values measured in other basins.

Geometry of the *model*: The geometry of the *model* is based in the structure of the Belsué area located between two synsedimentary north-south anticlines, the Pico del Águila anticline to the west and the Gabardiella anticline to the east (Millan *et al*., 1994).

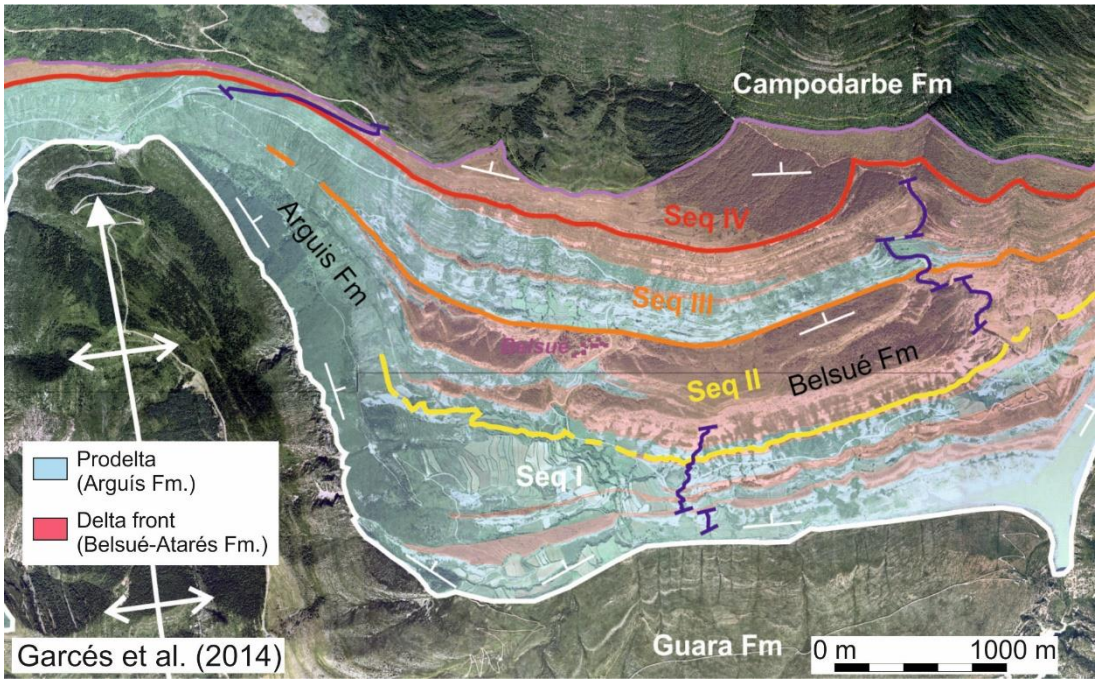

Figure 4.17: Geological map of the Belsué syncline. Blue represents prodelta sedimentation (Arguís formation) and red is for the delta front (Belsué formation). I, II, III and IV are the Sequences defined from Millán *et al*. (1994). The blue lines indicate the location of the stratigraphic section at figure 4.18.

The region has a north plunge as consequence of the tilting related with the emplacement of the Sierras Exteriores thrust front.

The area of the *model* is 34 km^2, and corresponds to the restored Belsué syncline before the folding. The original geometry and an evolution of subsidence has been estimated following the 3D geological model of Vidal-Royo *et al*. (2011). This model is a palinspatic restoration of the surfaces of the Eocene sequence boundaries of the deltaic sediments (Millan *et al*., 1994) in the area of del Pico del Águila. To calculate the subsidence within each sequence, thickness maps in between surfaces were made. In addition, these thickness maps have been overlaid with the bathymetric information from Castelltort *et al*. (2003) on the top of the interval to define subsidence from the previous stage. Finally, the *model* has been extended to the west to give space for the sediments that overflow the syncline.

Sediment types: Sedimentation in the middle-upper Eocene of the Belsué syncline is characterized by the development of the Belsué-Atarés delta, with clastic sediments comprising mostly shallow marine sandstones (delta front) and mudstones (prodelta-offshore) and minor delta plain units towards the top. To represent this situation, three different types of detrital sediments have been used for the reconstruction of the *model*. Those are *mud*, *sand* and *gravel*, a simplification needed for computational reasons and

Environment		*Gravel*	*Sand*	*Mud*	*Carbonate*
Gravity driven	Non-marine	0.0890	0.3979	0.6893	0.0010
	Marine	0.0171	0.3416	1.0248	0.0010
Water driven	Non-marine	0.8009	3.5815	6.2034	0.0010
	Marine	0.1537	3.0744	9.2232	0.0010

Table 4.4: Belsué model diffusivity coeficients (k).

to facilitate the interpretation of the results. In addition, also has been considered a small *carbonate* production in the shoreline that decreases as the bathymetry increases.

The detrital sediments have been defined with different diffusivity constants to simulate a different relative expansion from the source area, defining them to go further as the finer is the sediment. Instead, carbonates have been defined with a diffusivity constant close to 0 so that they remain in the same place where they are formed. Those carbonates are generated following equation 3.8. The diffusivity constants used are shown in table 4.4 and are different for the marine and non-marine environments.

The compaction laws integrated in the Dionisos have not been used to simulate the sediment compaction. These laws add complexity to the calculation and there is less control on the *model* variables. To compensate the effect of compaction a constant subsidence trend of 20 m/Myr has been added to increase the accommodation space continuously throughout the development of the *simulations*. This underlying trend has had been calibrated until the resulting bathymetry shows a similar trend to the measured in the field (Castelltort *et al*., 2003).

Sediment transport: The average sediment supply (Q_s) has been calculated from the sediment volume between the different surfaces of Vidal-Royo *et al*. (2011) and the average flow rate (Q_w) has been calculated assuming a flow turbidity of 0.1 kg/m^3 and a sediment density of 2 g/cm^3, by means of the following equation:

$$Q_w = \frac{Q_s \rho_{sed}}{turbidity} \tag{4.1}$$

Both the Qs and the Qw inputted are the average values, that will be evaluated by Monte Carlo (see step 3 in section 3.3.2).

Temporal and space resolution: The *model* has 230 time-steps with a duration of 20 each kyr and with 9375 square pixels of 40000 m^2 for each layer. The total duration of the *model* is 4.6 Myr corresponding to the time between the base of the chron C18r and the base of the C16, ages when the growth of the Belsué syncline took place (Garcés *et al*., 2014; Valero *et al*, in preparation).

3rd step: Generation of the different Monte Carlo scenarios

In this step are explained the *unknowns* evaluated on this *model*. Each Monte Carlo *model* have multiple *simulations*; on each *simulation* the value of the *unknowns* is different to test the effect of such *unknown* to the *model*.

First, we have defined the parameters on the *model* that could transport the Milankovitch signal. Those parameters are the Eustasy (E) for the propagation from the downstream; and water flow (Q_w) and sediment supply (Q_s) for the propagation of the climate signal from the upstream. The value of those three parameters have already been defined in the calibration phase. But for the Monte Carlo simulations, those calibrated values will become average values for each unknown. Over this average values, it will be applied a sinusoidal cyclical trend following the wave equation:

$$M(t) = A\sin(2\pi ft + \varphi) \tag{4.2}$$

In this equation *M* is the value of the *unknown* evaluated at time *t*, that in this *model* would be the values of Qw, Qs and E. *A* is the amplitude of the wave, *f* is the frequency, expressed in thousands or millions of years and φ is the phase of the wave.

Dionisos treats different E from Qw and Qs, so to model the E behavior is enough with the 4.2 equation. For Qs and Qw it must be added to the 4.2 equation the average value ($\bar{M}$) of each of the evaluated *unknowns*, calculated on the calibration step, the resulting equation has the following form:

$$M(t) = \bar{M} + A\sin(2\pi ft + \varphi) \tag{4.3}$$

In those equations (4.2 and 4.3) the *parameter A* specifically represents the amplitude of the variations and is the *parameter* that, if it becomes close to 0 will give a flat curve and, therefore, the average value of E, Qw and Qs will remain constant over time. Instead, the higher it gets, the wider will be the oscillations. Therefore, *parameter A* is what we will evaluate in each *simulation* to define the importance of the different Milankovitch cycles to the final result.

The climate modulation of the Milankovitch cycles is reflected on the insolation curve of the Earth. This insolation curve can be understood as the result of the weighted

convolution of the Milankovitch cycles of different frequencies. To reproduce that, for each modulated *unknown* we have opted for convolute three 4.3 equations with frequency periods of 100 kyr, 400 kyr, and 2.4 Myr for each variable: Qs, Qw, and E (figure 4.18).

For the amplitude values (A) of each *unknown* in each *simulation*, we have followed the following distribution. To represent all the cases a *model* design that includes 20 *simulations* has been done. These *simulations* have the A values distributed constantly, covering different expected positions of values independently of each other and assuming different combinations of values, leaving the different *simulations* as reflected in table 4.5. The assignment of these values is done in a directed way through internal formulas of the Dionisos software following a latin hypercube distribution.

4th step: Running the simulations

The different *simulations* have been calculated with a Workstation Dell Precision T7600 with an Intel® Xeon® CPU E5-2687W 0 @ 3.10GHz (2 processors) and 56 GB RAM, taking each of the *simulations* 1.4 hours on average, making a total of 27.6 hours for a *model* run.

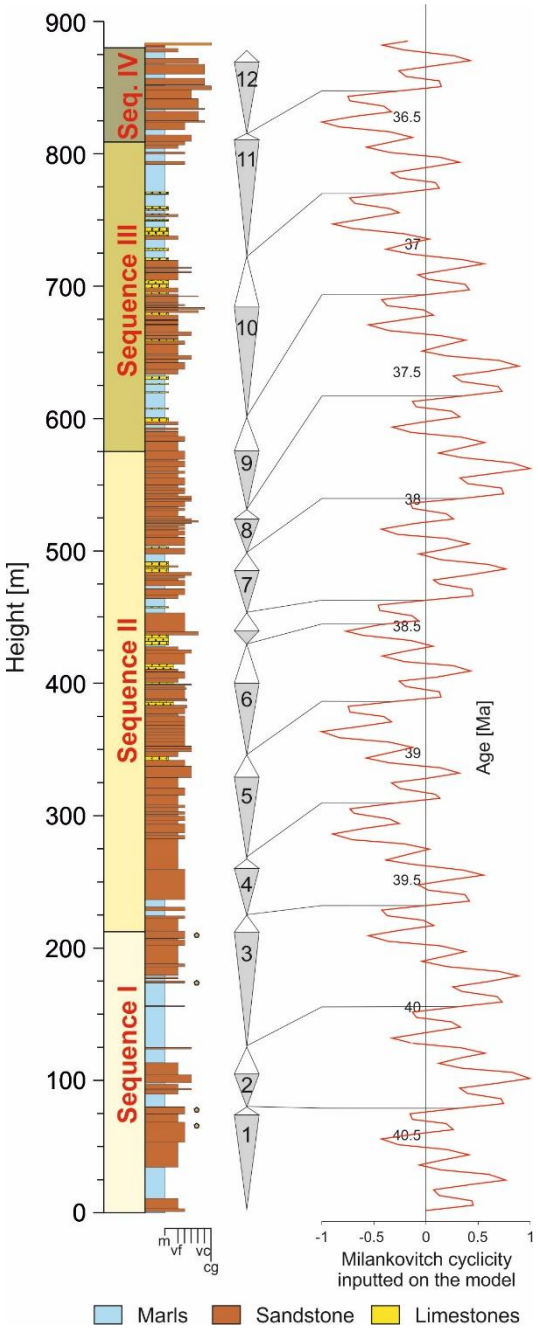

Figure 4.18: Relationship between the cycles found in the Belsué section and the dimensionless Milankovitch cyclicity used to modulate the Qs, Qw and E. Sequences are from Millan *et al*. (1994) and T/R cycles are extracted from Castelltort *et al*. (2003).

5th step: Post processing and interpretation

The results obtained have been analyzed by the procedures described in methods, giving the sensitivities on the figure 4.19. The values broadly reflect that the influence of

Simulation	Eustasy	Fluvial discharge	Sediment supply
#1	0.526	2.000	0.947
#2	1.368	1.158	1.158
#3	1.789	1.474	0.000
#4	2.000	0.421	1.684
#5	0.737	1.895	0.211
#6	1.474	0.211	1.053
#7	1.579	0.842	1.895
#8	1.053	0.737	1.474
#9	0.947	0.105	0.316
#10	1.895	1.579	0.737
#11	0.105	1.789	1.263
#12	0.632	1.263	0.421
#13	1.263	0.000	0.632
#14	0.316	0.947	1.579
#15	0.421	0.632	0.842
#16	0.000	1.053	2.000
#17	0.211	0.526	0.105
#18	1.684	0.316	0.526
#19	1.158	1.684	1.789
#20	0.842	1.368	1.368

Table 4.5: Monte Carlo distribution of the Belsué simulations. Maximum values represent double of the average imputed value. Minimum value represents 0 of the average value. This implies a major variability on the higher values than in the minimum values, being constant when is 0.

sediment supply is predominant to define the final sediment distribution over the eustasy and the water discharge.

Here, to study whether the Milankovitch cyclicity is influenced from the upstream or from the downstream portions of the system we searched a *parameter* with the most equivalent sensitivities in the upstream and

Sediment type	Eustasy	Sediment supply	Water discharge
Sand	1.886	97.600	0.514
Gravel	81.718	17.815	0.467
Average	*41.802*	*57.583*	0.981

Table 4.6: Sand and gravel sensitivities on the different variables. The sum of both sensitivities shows appropriate to evaluate the results as they are similar enough to establish a comparison between them.

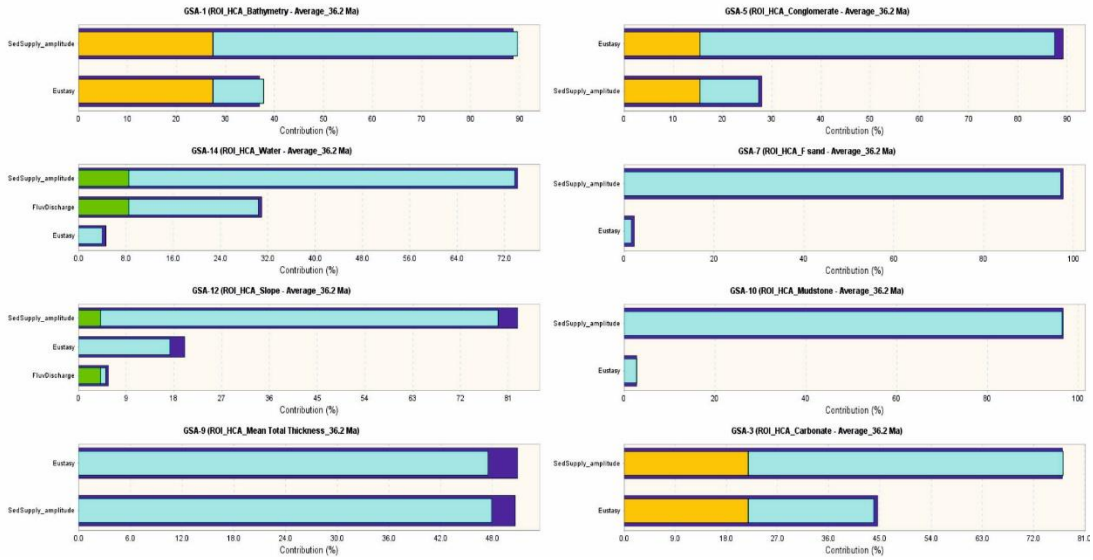

Figure 4.19: Contribution of the different evaluated unknowns on the final distribution of each parameter.

the downstream in order that the comparison is significant. We found this equality adding the sand *parameter* and the gravel *parameter* (table 4.6).

So, to sum the different values of sand and gravel, it has been designed a script codded in Groovy that does this calculation for each cell, obtaining the value called "gravel+sand" This script is in the digital suppl. data 2 of this thesis.

The values of this new “gravel+sand” *parameter* for each *simulation* (figure 4.20) has been compared on a location in the *model* equivalent to the section that crops out in the field (figure 4.17). From this comparison we conclude that all the sections in the different *models* are similar to the field section. This is because of the predominance of the tectonic subsidence over the climatic signal. Looking at the expression of the sequence I progradation, the expression of the transgression on the sequence II and the double regression of the sequence III, the #4, #7, #8 and #19 have been considered as the *best fit simulations.*

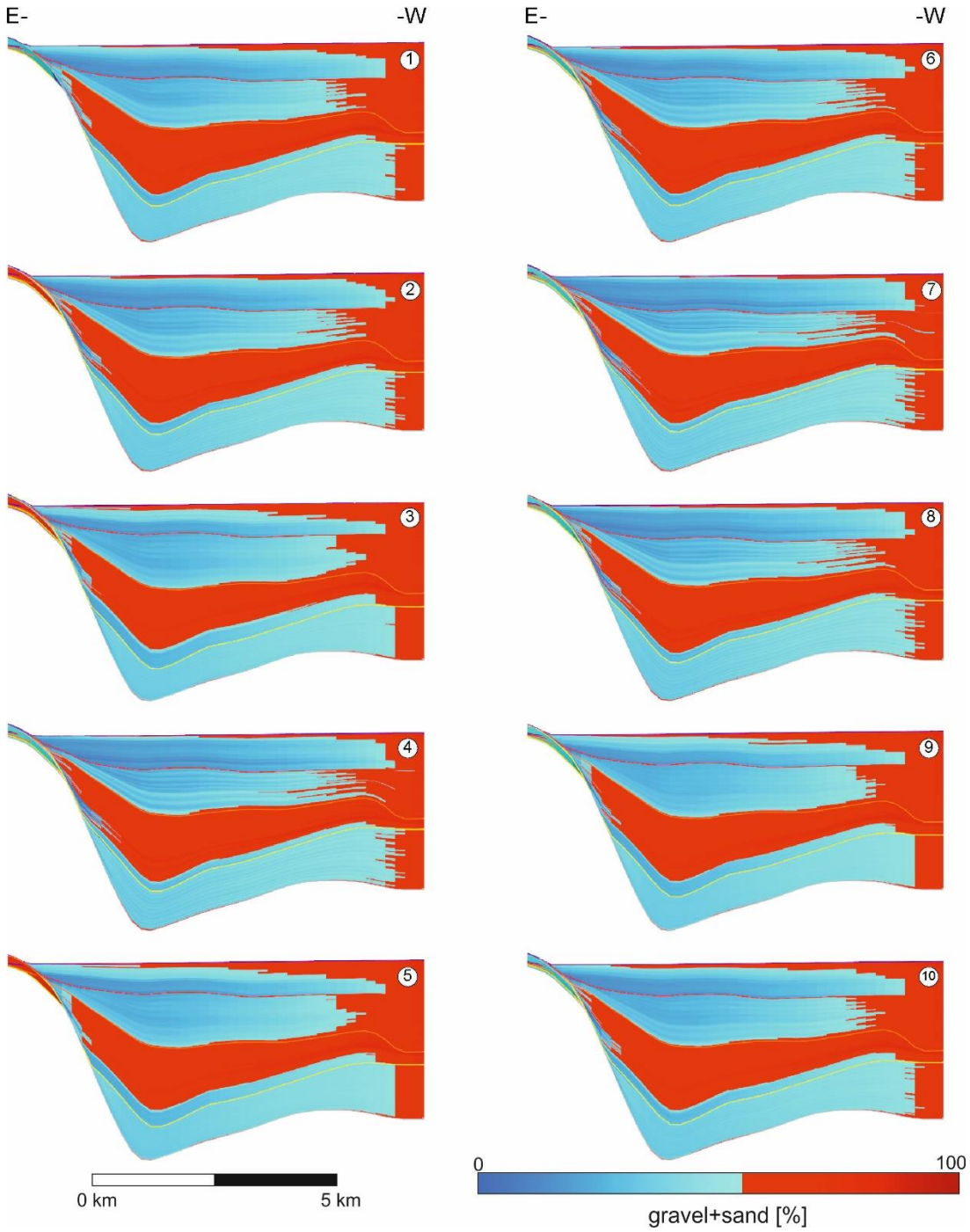

Figure 4.20: Simulations #1 to #20 of the Belsué model. Blue represents muddy sediment and red represents the coarser fraction (gravel+sand). Sediment input from the east. Yellow, orange and red lines represent the Millan *et al*. (1994) sequences boundaries (see figure 4.17). Vertical scale is 3 times the horizontal scale.

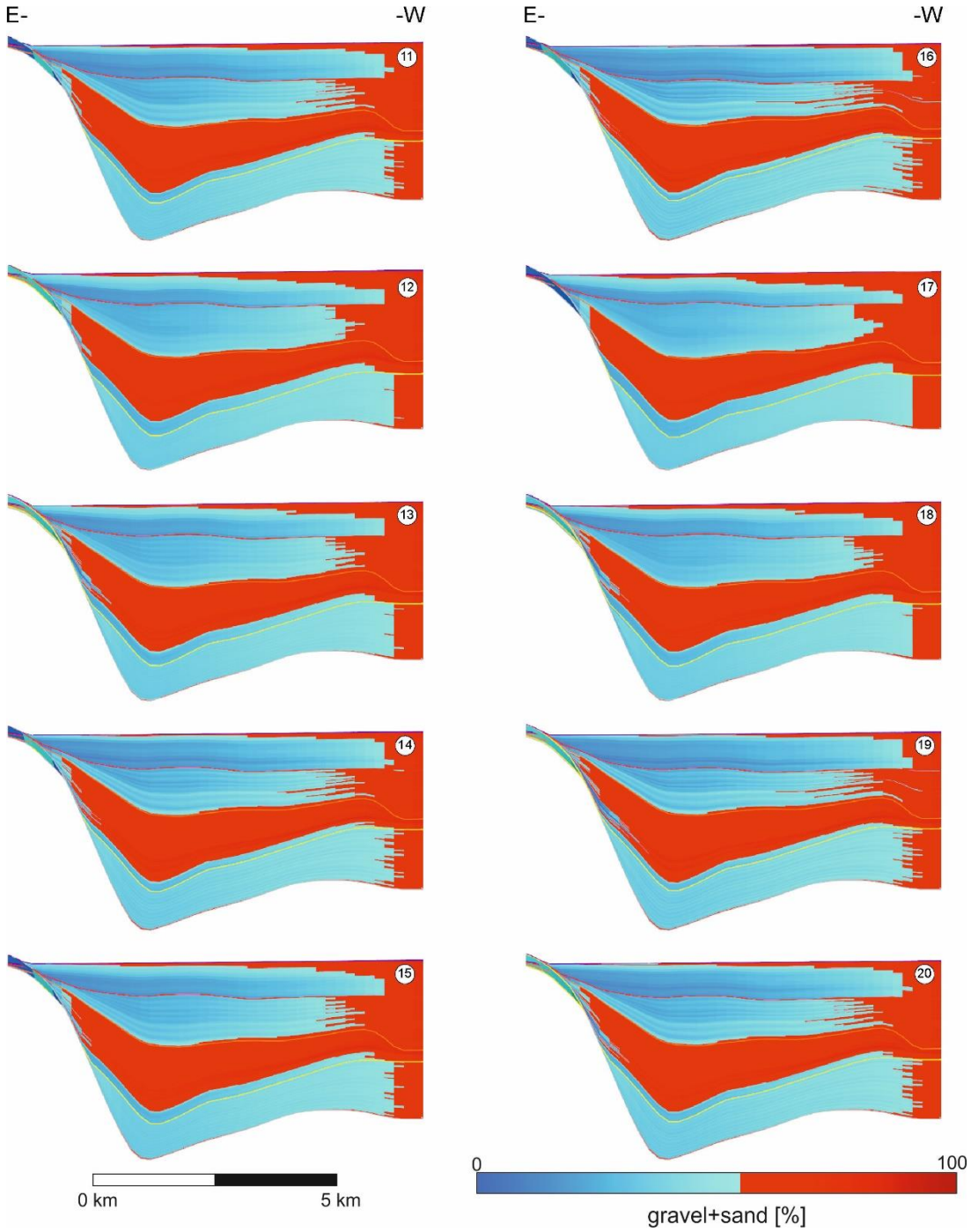

Figure 4.20 (continued)

4.3.2 General Flow Model (GFM)

1st step: The inquiry

For the flow model, I focus on understanding **the Tremp-Jaca basin sediment routing evolution from the source area to the Jaca basin, *i.e.* between the meridian of Tremp (0.89° E) and the meridian of Jaca (0.55° W), from upper Lutetian to Priabonian.**

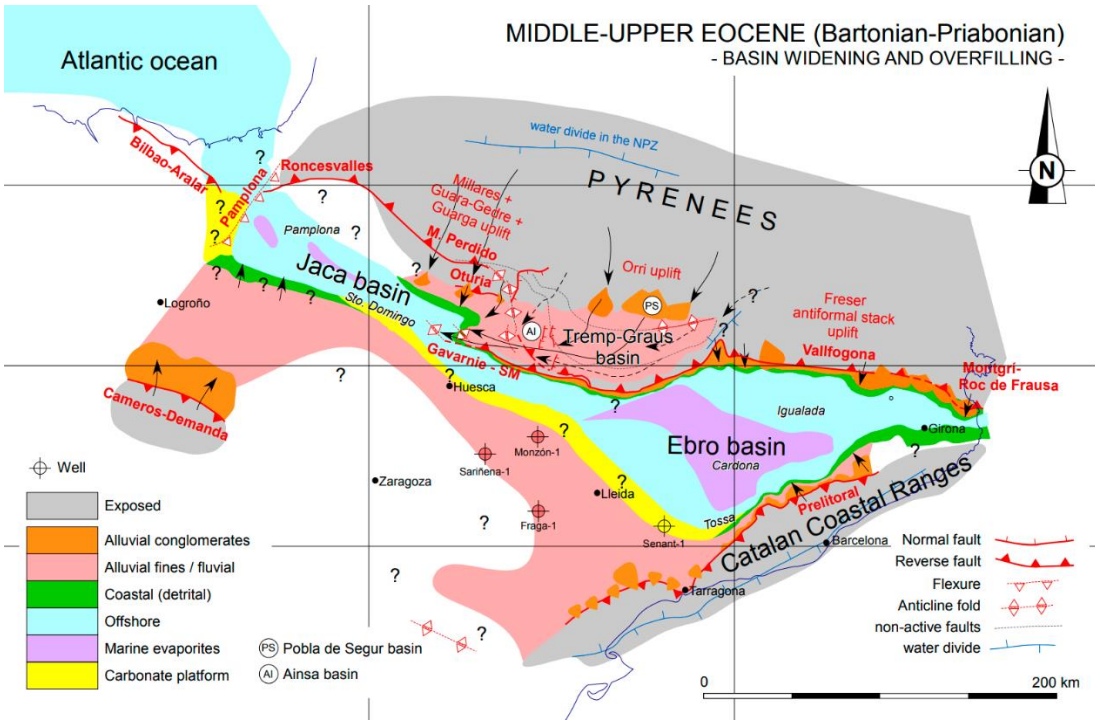

Figure 4.21: Paleogeographic maps of the South Pyrenean Foreland basin on the Bartonian-Priabonian. Garcés *et al*. (2020).

The Tremp-Jaca basin was part of the southern foreland of the Pyrenean chain during Paleogene. Clastic sediments were derived from the uplifting Pyrenees (present-day axial zone) an E-W oriented high-relief area located to the north and redistributed towards the west along a E-W oriented trough (Tremp-Jaca basin). As mentioned in the introductory section, the basin history was influenced by the emplacement of a piggy-back sequence of frontal thrust and fold growth.

For a correct performance my *model* will cover a larger surface than the targeted area, or *high confidence area* which is the area between the meridians of Tremp and Jaca. In the low confidence area, yet a number of unknowns or discussed points remain. The main uncertainties rise from the absence of geological record in Basque Cantabrian area during Bartonian and Priabonian times (Barnolas *et al*., 2019). The lack of geological constraints prevents us to establish an accurate link between the TJB distal parts and their potential equivalents in the Atlantic Ocean. Recent works pose doubts on such connection during the Bartonian/Priabonian (figure 4.21) (Garcés *et al*., 2020), whilst some other works based on paleocurrents (Jaizkibel turbidites, Kruit *et al*., 1972) and sedimentary thicknesses even stand for a non-connected scenario (Ortiz *et al*., 2019). Sediment routing analysis of the sedimentation during middle and upper Eocene were undertaken under a non-connected scenario (Michael *et al*., 2014). Complementary, paleogeographic models (figure 4.22) (Vacherat *et al*., 2017) suggest a connection of

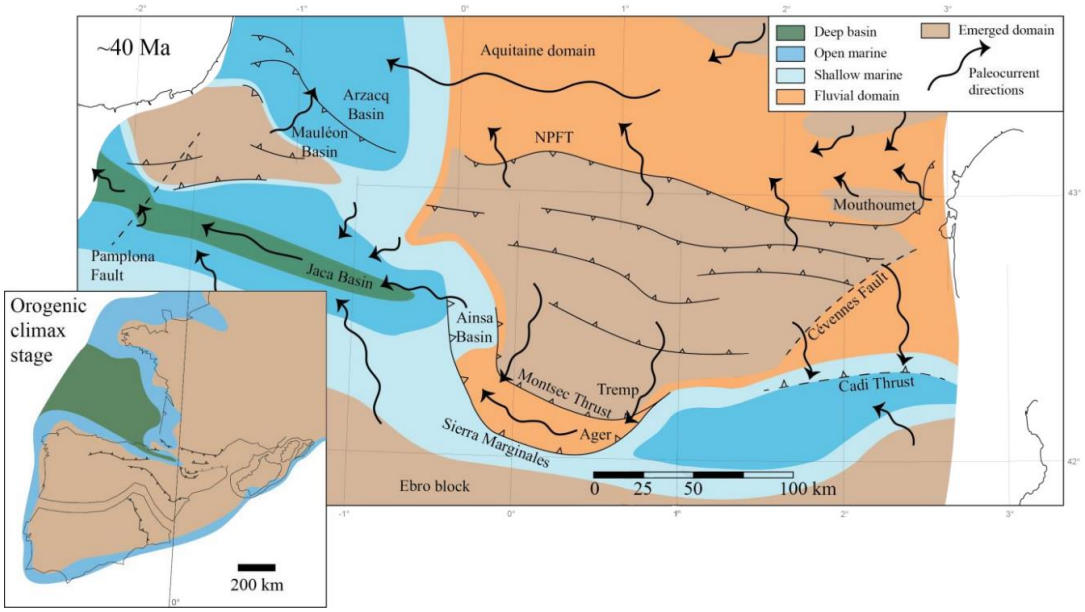

Figure 4.22: Paleogeographic map of the Pyrenees during the Lutetian-Bartonian. Vacherat *et al*. (2017)

the TJB with the Atlantic Ocean, although west of the Cuisian/Lutetian Basque Cantabrian turbidites.

To facilitate model performance and following Vacherat *et al*., (2017) models, we considered a paleogeography in which TJB connected with the Atlantic Ocean. In addition, a test of the different hypothesis as well as the reliability of the results will be performed by comparing model outputs with the SR dataset derived from data in the TJB (Vinyoles *et al*., 2020; section 4.2.1 on this thesis) together with the paleocurrents distribution from the Tremp-Jaca basin (Puigdefàbregas, 1975; Vincent, 2001; Barsó, 2007; Arbués *et al*., 2011; Michael *et al*., 2014; Roigé *et al*., 2016; and unpublished data from UB researchers).

2nd step: The calibration model

To calibrate the *unknowns* of this *model* data, such as the evolution of sedimentation rates of the area have been used (see section 4.2 in this thesis). In addition, paleobathymetric data and a geometrical projection for the emerged environments have been also considered.

The *model* geometry, is derived from the area between the Tremp and Jaca meridians, bounded on the north by the present day position of the Gavarnie thrust in Jaca and the basal unit of the Nogueres thrust sheet in Tremp. To the south, the boundary is at the present day position of the Gavarnie thrust, at the south of the Sierras Exteriores – Serres Marginals (figure 4.23). In addition, the basin has been extended with a geometric

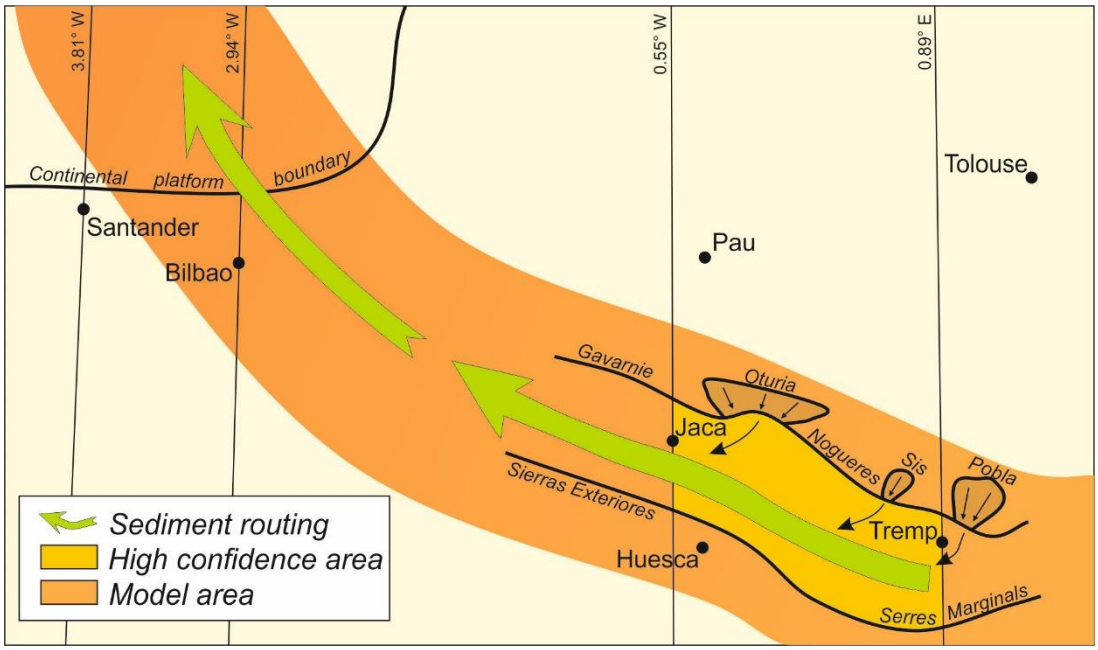

Figure 4.23: Schematic draw of the GFM area and the three northern sediment entry points. Arrows represent the overall sediment routing from east to west. The present day platform boundary is also indicated as a reference. The present day platform boundary is also indicated as a reference.

projection to the west to simulate the area for the sediments leaving the basin to the Bizcaia Gulf.

SR maps of the Tremp-Jaca basin (figure 4.15) were used to calculate and build sediment volume maps and thickness maps. Those maps where used together with paleobathymetric maps, to elaborate subsidence and slope maps for each chron interval. The bibliographic sources for the bathymetric data are summarized in the table 4.7. For non-marine zones a slope has been assumed following an exponential equation, empirically deduced from the Markham river (Papua New Guinea):

$$h(x) = e^{(0.04S\Delta x)} \tag{4.4}$$

Where *h* is the height above sea level, *s* is the sinuosity index (1.2 if there is little tectonic activity, 1.4 if there is more tectonic activity) and Δx is the map distance from the measured point to the river mouth.

The evolution of the eustatic curve it has been adjusted to the major transgressions and regressions on the south Pyrenean foreland basin. Since the compaction of the sediments has not been computed, a constant general rise on the base level to create accommodation space has been established.

	C20r		C20n		C19r		C19n		C18r		C18n		C17r		C17n		C16r	
	Value	*Ref.*	*Value*	*Ref.*	*Value*	*Ref.*	*Value*	*Ref.*	*Value*	*Ref.*	*Value*	*Ref.*	*Value*	*Ref.*	*Value*	*Ref.*	*Value*	*Ref.*
Belsué	-	-	-	-	-	-	-	-	115	1	100	1	80	1	60	1	40	1
SM	100	5	50	5	20	5	50	5	-	-	-	-	-	-	-	-	-	-
PS	-24	6	-16	6	-76	6	-160	6	-215	6	-392	6	-222	6	-307	6	316.3	6
Àger	-19	6	-13	6	-26	6	-52	6	-119	6	-145	6	-159	6	-188	6	228.0	6
Ésera	-1	6	50	5	-	-	-	-	-	-	-	-	-	-	-	-	-	-
Lascuarre	-	-	-	-	-	-	-5	6	-11	6	-15	6	-25	6	-23	6	-	-
Yebra	-	-	-	-	-	-	-	-	-	-	100	5	20	5	-1	6	1.76	6
GA	650	5	600	5	500	5	550	5	400	5	-	-	-	-	-	-	-	-
Isuela	15	4	15	4	40	4	200	4	-	-	-	-	-	-	-	-	-	-
Mediano	250	5	300	5	50	5	-1	6	-2	6	-	-	-	-	-	-	-	-
Olsón	-	-	-	-	-	-	-	-	-	-	-5	6	-7	6	-6	6	5.01	6
Coscollar	150	5	200	5	130	5	-	-	-	-	-	-	-	-	-	-	-	-
Ainsa	600	3	400	3	-	-	-	-	-	-	-	-	-	-	-	-	-	-
Buil	-	-	-	-	-	-	80	2	-	-	-	-	-	-	-	-	-	-
Coast	Coastline extracted from the figure 4.15 for all the chrons.																	

Table 4.7: GFM paleobathymetries. Values are extracted from (1) Castelltort *et al*., 2003, (2) Mateu-Vicens *et al*., 2012, (3) Pickering and Corregidor, 2005, (4) Silva, 2017, (5) extrapolated from the lithologies of each section on Vinyoles *et al*. (2020), (6) Non-marine values have been calculated from the distance from the river mouth to the calculation spot on this thesis by the 4.4 equation.

Environment		*Sand*	*Mud*	*Carbonate*
Gravity driven	Non-marine	225.0000	503.1153	0.1000
	Marine	7.5000	37.5000	0.0010
Water driven	Non-marine	3525.0000	7882.1396	1.0000
	Marine	117.5000	587.5000	0.0100

Table 4.8: General Flow Model model diffusivity coeficients (k).

The diffusivity constants have been defined with the diffusivity calculator integrated in Dionisos, using realistic slope values as input data. The diffusivity values are on the table 4.8.

The average sediment supply was calculated from the sediment volume extracted from the sedimentation rates. The water flow has been calculated assuming a turbulence of the incoming water of 0.098 kg/m^3, by means of the 4.1 equation.

Other boundary conditions are those related to the resolution of the *model*. The *model* has 90 time-steps of 0.1 kyr/time step and with 9553 square pixels of 2 km^2 for each layer. The total duration of the *model* is 9.0 Myr which are those between the base of the chron C20r and the base of the C16r, coincident with the period for which good data are available.

3rd step: Generation of the different Monte Carlo scenarios

The challenge on this *model* was to balance the importance between the different sediment entry points. So, in this modeling, three different sediment input points have been tested to observe the importance of the sediment entry for each point and the interactions between them. Those input points represent the Pobla de Segur, the Sis and the Oturia alluvial systems.

Sim.	*Oturia*	*Pobla*	*Sis*
#1	1.429	1.429	1.429
#2	0.857	0.000	1.143
#3	0.000	0.286	0.857
#4	1.143	1.143	0.000
#5	0.571	1.714	0.571
#6	1.714	2.000	0.286
#7	0.286	0.571	1.714
#8	2.000	0.857	2.000

Table 4.9: Monte Carlo distribution of the GFM simulations. Maximum values represent double of the average imputed value and minimum value represents 0 of the average value. When the value is 0 there is no sediment supply from the corresponding input point. When the value is 2 the average estimated value is duplicated.

For balancing the role of each entry point we have used the Monte Carlo approach designing 8 *simulation* scenarios (table 4.9) were changes on the sediment budget on the three entry points have been performed. The assignment of these values is implemented in a directed way through internal formulas of the Dionisos software following a latin hypercube distribution. The outputted results are contrasted with the SR maps for the different chrons (figure 4.15). An algorithm has been designed to compare the sedimentation rates for each chron on the direct measurement maps (figure 4.15) and the sedimentation rates obtained on the *simulations*. This comparison is made at the locations of Tremp, Graus, Ainsa and Jaca.

$$S_s = \frac{\sum_{i=1}^{n}(S_i \Delta t_i)}{\Delta t_T \; 10/S_{max}} \quad (4.5)$$

In this equation, S_s is the *simulation* score, S_i is the partial score of a *simulation* corresponding to a chron interval, Δt_i is the chron duration, Δt_T is the total duration of the *model* and S_{max} is the maximum score that can be achieved for a *simulation*.

4th step: Running the simulations

The different *simulations* have been calculated with a Workstation Dell Precision T7600 with an Intel® Xeon® CPU E5-2687W 0 @ 3.10GHz (2 processors) and 56 GB RAM, taking each of the *simulations* 1.4 hours on average, making a total of 27.6 hours for each *model* run.

5th step: Post processing and interpretation

ID#	C20r *2.437 Myr*	C20n *1.154 Myr*	C19r *0.913 Myr*	C19n *0.234 Myr*	C18r *1.003 Myr*	C18n *1.533 Myr*	C17r *0.288 Myr*	C17n *1.411 Myr*	Total score
1	3	2.5	3	2	3	3.5	1	3	8.40
2	1	1.5	3.5	1.5	4	4	2	3	6.93
3	2	1.5	2.5	1.5	3.5	4	2	3	7.45
4	1	3	3	1.5	2.5	4	1.5	3	6.83
5	3	2.5	3.5	1	2	4	2.5	3	*8.52*
6	2.5	2.5	4	1.5	2	3.5	2.5	3	8.01
7	3	2.5	3	1.5	2	2	2.5	3	7.57
8	3	2.5	3.5	1.5	2.5	2.5	2	3	8.01

Table 4.10: Partial and total scores of the GFM. The total scores are corrected to the chron duration by the means of the 4.5 equation.

To determine the most similar configuration to the measured on the *simulations* it has been done a comparison of the sedimentation rate maps on the figure 4.15 with the sedimentation rates obtained at the equivalent area on the *model*. The maps for each *simulation* are on the figure 4.24. It has been compared the “real” and “simulated” SR for the villages of Tremp, Graus, Ainsa and Jaca. For each location it has been assigned a score, so the maps are evaluated from 0 to 4. The *simulation* with a higher score in all the chrons, ponderated by the chron duration (equation 4.5), it has been considered the

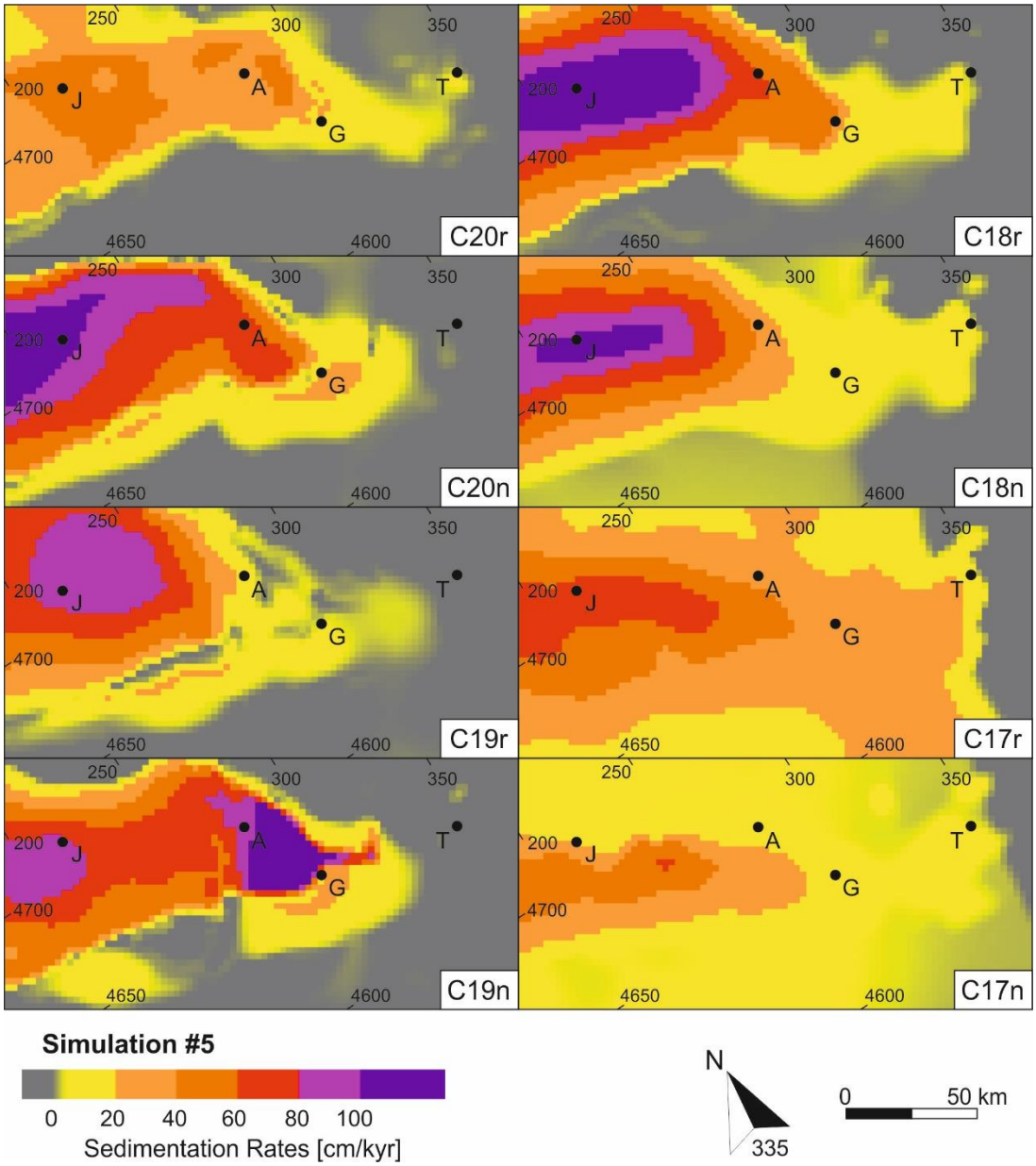

Figure 4.24: Sedimentation rate maps for each chron of the *Best Fit Simulation* (#5) in the GFM. Coordinates are in km in the UTM reference system. The shortening related to thrust advance and clockwise synsedimentary rotation of the Ainsa Basin and External sierras structures has not been considered. J: Jaca, A: Ainsa, G: Graus, T: Tremp.

best fit simulation. In this case, the *best fit simulation* is the *simulation* #5. All the partial and total scores can be found in the table 4.10.

Once determined the *best fit simulation* and for analyzing the routing system, it has been studied the behavior of the water flow, the slope, and the sedimentation rate, the lithology and the subsidence.

5 DISCUSSION

This discussion is divided into four sections, where the different results obtained on this thesis are analyzed separately. The first section presents an analysis of the sedimentation rates, its relationship with the different depozones, and the key controls related to depocenter location and migration. Then, the two models performed in the frame of this thesis are analyzed, discussing the results and contextualizing the numerical results with the field data. A last four section presents a general discussion, where all the results are integrated.

5.1 Sedimentation rates in the Tremp-Jaca basin (From Vinyoles *et al*., 2020)

Sedimentation rates in the Tremp-Jaca basin have been explored in Vinyoles *et al*. (2020). This section exposes the discussions contained therein. First, the relation between the sedimentation rates and the depozones is discussed, and the key role of the depozone concept in order to help making predictions on the sedimentation rates and to understand how sedimentation rates are affected as depozones migrate. Then the causes of the depocenter generation and migration are analyzed, starting from the basinwards migration due to the clastic shelf progradation, explaining how the depocenter migrates landwards when there is a transgressive episode and then is discussed the presence of a long term stable depocenter. Finally, it is discussed the presence of unexpected high sedimentation rates in non-marine settings by different possible approaches.

5.1.1 Sedimentation rates and depozones

The extensive structural and stratigraphic work carried out in the TJB (Puigdefàbregas, 1975; Millán *et al.*, 1994; Poblet *et al.*, 1998; Arbués *et al.*, 2011; Beamud, 2013; Muñoz *et al.*, 2013; Rodriguez-Pintó, *et al.*, 2016; Roigé *et al.*, 2016; Garcés *et al.*, 2020, among others) has provided the precise ages and locations of the different frontal structures of the southern Pyrenees in the study area. We have used them for the location of the different foreland depozones relative to the migrating deformation front (figures 5.1 and 5.2). Figure 5.1 marks the location of depozones for successive chron intervals, from C21n to C17n (47.8 to 36.9 Ma). Figure 5.2 shows a map view of these depozones with their location relative to the deformation front, as well as the tectonic structures active in each time-slice. The progressive advance of the deformation front is documented together with the westwards and southwards migration of the depozones. The present day “Z-shape” map view of the clastic sediment routing system from Tremp-Graus to

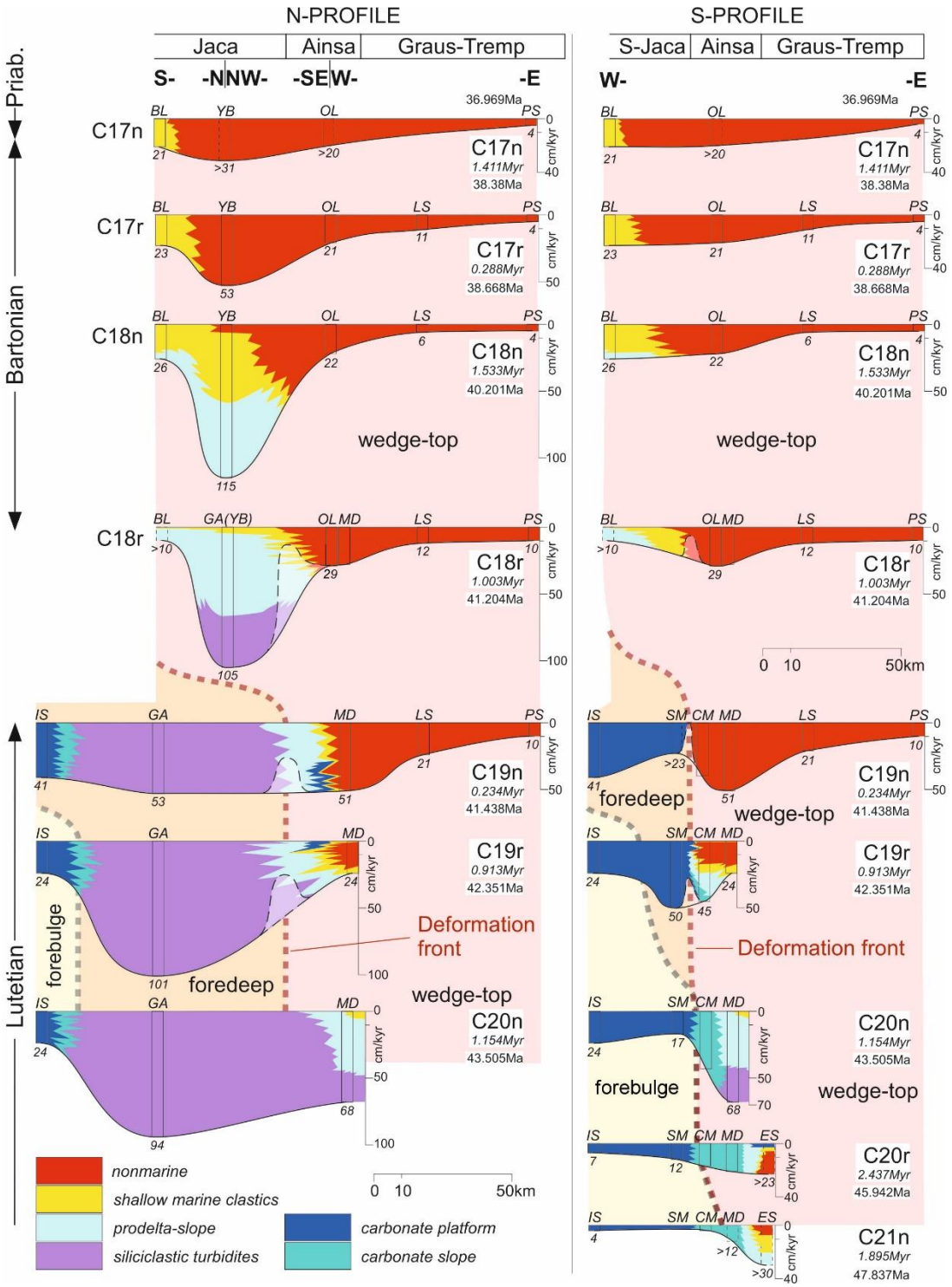

Figure 5.1: Evolution of decompacted SR across the Tremp-Jaca basin over time following the N-Profile and the S-Profile. 16 Graphs show SR variation for each time-slice (magnetostratigraphic chron) and distribution of the main facies belts. Vertical scale: SR in cm/kyr; horizontal scale: distance in km. Absolute ages from GPTS (Gradstein *et al*., 2012). Individual SR for each log are indicated. Background colors represent the attribution of the logs to the different depozones. The logs used are: BL, Belsué; IS, Isuela; SM, Santa Marina; GA, Gállego-Aragón; YB, Yebra de Basa; OL, Olsón; CM, Coscollar-Mondot; MD, Mediano; ES, Ésera; LS, Lascuarre; PS, Pobla de Segur. Dashed logs and SR curves indicate minimum values due to incomplete logs. Duration of each magnetozone is indicated in Myr. The SR graphs have been produced from the data obtained on the studied logs. Only variations related to Boltaña and Balzes anticline growth have been inferred since these structures have an important role on SR evolution and distribution.

Jaca during the Lutetian and early Bartonian (figure 5.2 b, e) is a consequence of the progressive clockwise vertical-axis rotation of the AOZ from Lutetian to Oligocene (Mochales *et al.*, 2012; Muñoz *et al.*, 2013). This rotation affects the central part of an E-W to ESE-WNW oriented sedimentary trough, as shown in the reconstructions by Muñoz *et al.* (2013) and Garcés *et al.* (2020). This trough should have shown a relatively straight ESE-WNW orientation during early Lutetian similar to the geometry observed in the maps of the uppermost Bartonian and Bartonian-Priabonian (figures 5.2 f, g, and h).

In the studied portion of the TJB, the wedge-top depozone is identified in the hanging wall of active thrusts and related folds. However, the distinction between foredeep and forebulge is not straightforward because the transition between the two zones maybe gradual and difficult to establish (DeCelles and Gilles, 1996). As indicated in DeCelles and Gilles (1996), in underfilled submarine foreland basin systems local carbonate platforms may develop in the forebulge depozone (Wuellner *et al.*, 1986; Patton and O'Connor, 1988; Allen *et al.*, 1991; Dorobek, 1995). Thus, the main sedimentological attributes of some of the studied sections cratonward from the main clastic trough (carbonate platform deposits with low SR) can be interpreted as part of a forebulge depozone (DeCelles and Giles, 1996).

During most of the Lutetian the basin was configured into wedge-top (Tremp-Graus and part of Ainsa in the hanging wall), foredeep (Northern Jaca and part of Ainsa in the footwall) and forebulge (Southern Jaca) depozones (figures 5.1 and 5.2). The forebulge depozone is associated with shallow-marine carbonate deposition (Guara formation) with relatively low SR (3 to 24 cm/kyr), and it is easily recognizable (logs IS and partially SM and CM in Ainsa) from C21n to C19r (47.8 to 42.4 Ma). The proximal foredeep is characterized by the presence of a distinct depocenter in Northern Jaca (log GA) with high SR (53 to 101 cm/kyr) in the Hecho group deep marine succession from C20n to C19n (43.5 to 41.2 Ma) (figures 5.1 and 5.2). This depocenter is located south to the deformation front in the footwall of the Monte Perdido thrust sheet (Muñoz *et al.*, 2013). The Montsec-Peña Montañesa thrust and its related splays (La Fueba thrust system) were the frontal structures of the Pyrenees until late Ypresian (C21r) (Muñoz *et al.* 2013). Afterwards (C21n), the deformation front shifted 10-15 km towards southwest, starting the emplacement of the Gavarnie thrust sheet which incorporated part of the former Montsec-Peña Montañesa related foredeep depozone to the new wedge-top and creating a new depozone boundary marked by the Añisclo and Olsón Anticlines (between MD and CM logs).

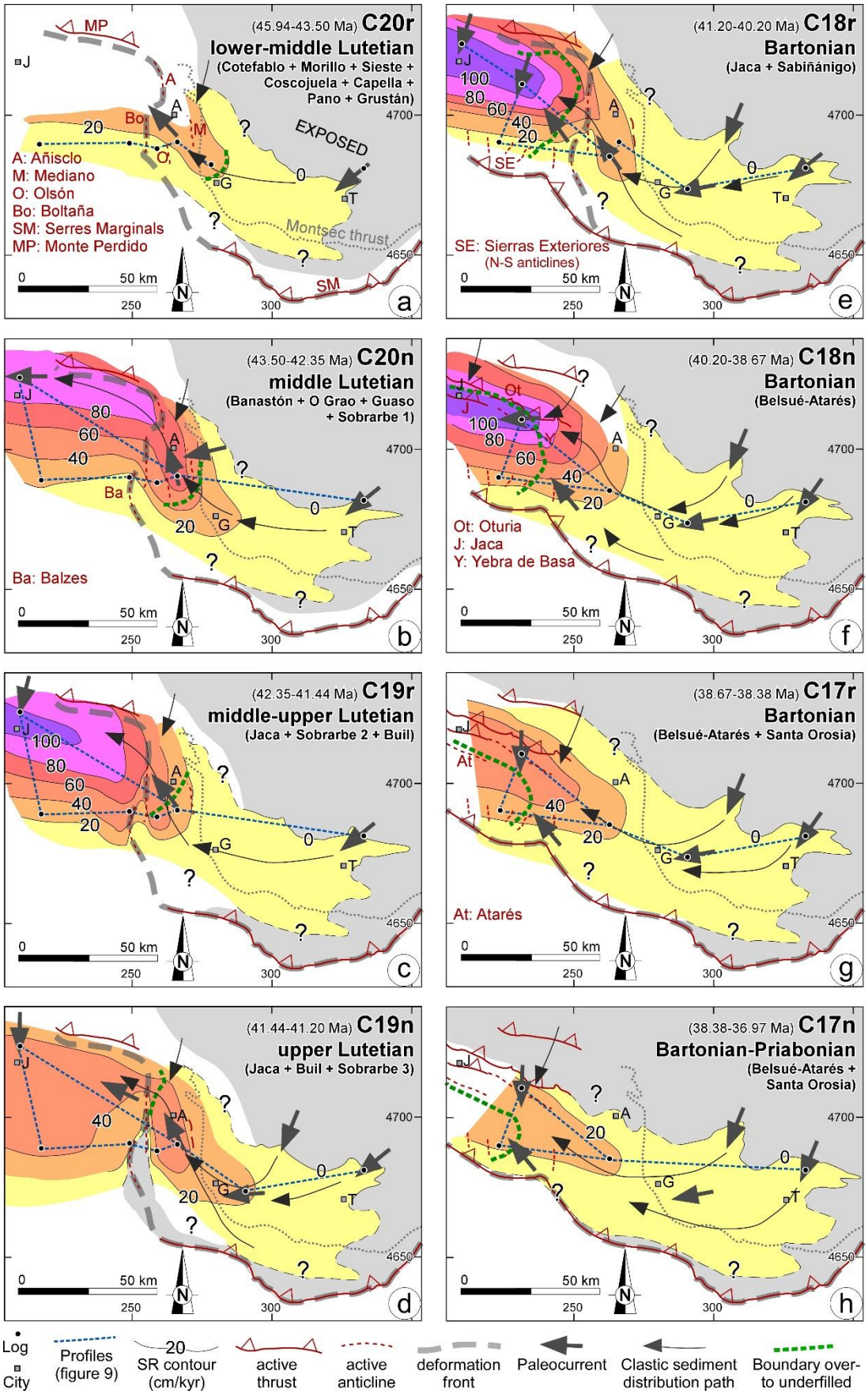
(45.94-43.50 Ma) C20r
lower-middle Lutetian
(Cotefablo + Morillo + Sieste + Coscojuela + Capella + Pano + Grustán)
A: Añisclo
M: Mediano
O: Olsón
Bo: Boltaña
SM: Serres Marginals
MP: Monte Perdido
EXPOSED
Montsec thrust
a
(43.50-42.35 Ma) C20n
middle Lutetian
(Banastón + O Grao + Guaso + Sobrarbe 1)
Ba: Balzes
b
(42.35-41.44 Ma) C19r
middle-upper Lutetian
(Jaca + Sobrarbe 2 + Buil)
c
(41.44-41.20 Ma) C19n
upper Lutetian
(Jaca + Buil + Sobrarbe 3)
d
(41.20-40.20 Ma) C18r
Bartonian
(Jaca + Sabiñánigo)
SE: Sierras Exteriores
(N-S anticlines)
e
(40.20-38.67 Ma) C18n
Bartonian
(Belsué-Atarés)
Ot: Oturia
J: Jaca
Y: Yebra de Basa
f
(38.67-38.38 Ma) C17r
Bartonian
(Belsué-Atarés + Santa Orosia)
At: Atarés
g
(38.38-36.97 Ma) C17n
Bartonian-Priabonian
(Belsué-Atarés + Santa Orosia)
h
0 50 km
250 300
4700
4650
Log
City
Profiles (figure 9)
20 SR contour (cm/kyr)
active thrust
active anticline
deformation front
Paleocurrent
Clastic sediment distribution path
Boundary over-to underfilled

Figure 5.2: Map view evolution of SR across the TJB over time. Each time step corresponds to a different chron as shown in figure 5.1. Coordinates are in km in the UTM reference system. This map shows the present-day location of structures and logs and the trace of figure 5.1 profiles through the logs considered for each chron. Absolute ages from GPTS (Gradstein *et al*., 2012). The shortening related to thrust advance and clockwise synsedimentary rotation of the Ainsa Basin and External sierras structures has not been taken into account (Palinspastic reconstruction is not considered). The Montsec-Peña Montañesa thrust has been used as a reference since it was not an active structure during the studied interval. Paleocurrent data from Puigdefàbregas (1975); Vincent (2001); Barsó (2007); Arbués *et al*. (2011); Michael *et al*. (2014); Roigé *et al*. (2016), and our own data. J: Jaca, A: Ainsa, G: Graus, T: Tremp. SR variations related to anticline growth have not been inferred except Boltaña and Balzes folds due to their influence on clastic sediment routing. Cotefablo, Banastón and Jaca are turbidite systems of the Hecho group in the Jaca basin (Mutti *et al*., 1985; Labaume *et al*., 1987). Morillo, Coscojuela, Gabardilla, O Grao and Guaso are turbidite systems in the San Vicente Formation in the northern Ainsa Basin (Arbués *et al*., 2011; Muñoz *et al*., 2013). Sobrarbe 1: Deltaics older than San Lino horizon (Arbués *et al*., 2011) in Ainsa; Sobrarbe 2: Sobrarbe Deltaic Complex below Buil nummulite banks; Sobrarbe 3: Sobrarbe Deltaic Complex above Buil nummulite banks.

During C21n there is a relatively constant low (3 to >12 cm/kyr) SR zone with carbonate platform and slope sedimentation occupying Southern Jaca and eastern Ainsa (IS to CM logs), grading eastwards to higher SR in eastern Ainsa and western Tremp–Graus (>30 cm/kyr) where shallow marine and non-marine sedimentation occurs (S-profile, figure 5.1). Thus, the western oblique boundary of the wedge-top depozone is in a location where the expected increase in SR towards non-deformed areas (footwall) does not occur. We do observe instead a westwards decrease from 11 cm/kyr at MD (wedge-top) to 4 cm/kyr at CM (forebulge) (figure 5.1; C21n). The absent or very narrow (less than 3.5 km wide) foredeep at this position points to an abrupt transition from forebulge to a thrust-top depozone with moderate SR (>30 to >12 cm/kyr). This sharp transition is due to the differential advance of the Gavarnie trust whose oblique front reached (very close to) the forebulge in southern Ainsa Basin whereas in Jaca Basin the deformation front was located further north (Muñoz *et al.*, 2013, Garcés *et al.*, 2020) with a well-developed foredeep to the south. However, these 2D observations are restricted to the available magnetostratigraphic logs which do not cover the northern Ainsa basin. The N-S cross sections in Cámara and Klimowitz (1985) show an important thickening of the Lower and middle Eocene units towards the north in the Ainsa basin, with the MD and CM logs located close to the southern edge. This implies a northward increase in SR of the wedge-top basin potentially connected to the foredeep growing to the northwest in the Jaca basin (figures 4.10 and 5.2b). At C20 SR show a similar trend as during C21n (S-profile, figure 5.1), with higher SR (43 to 68 cm/kyr) to the east (wedge-top) than to the

west, where carbonate platform and slope deposition took place with low to moderate SR (17 to 24cm/kyr).

The northern profile between C20 and C19r highlights changes in SR west of the oblique thrust front (Boltaña and Balzes structures). The N-S orientation of the profile between GA and IS (figures 4.10, 5.1 and 5.2), perpendicular to the western Pyrenees structures, allows clear observation of the expected SR for a transition between forebulge, foredeep and wedge-top. In its northern edge, SR reach close to their highest values of 95-104 cm/kyr. To the east of the oblique front (Balzés Anticline) relatively high SR (50 cm/kyr) are obtained from carbonate platform deposits in the SM section in Southern Jaca (figures 5.1 and 5.2c). These carbonate platform deposits display a fan-like geometry related to a syntectonic progressive unconformity linked to the growth of the Balzes anticline (Rodríguez-Pintó *et al.*, 2016). During C19n Southern Jaca shows its maximum SR (41 and >23 cm/kyr) close to the proximal foredeep values for Northern Jaca (53 cm/kyr) and the wedge-top (51 cm/kyr in Ainsa). Thus, during C19, the former distal foreland was incorporated into the foredeep, as deduced from a threefold increase in SR in SM (from C20n to C19r), and double in IS (from C19r to C19n). This part of the foredeep still remained as a carbonate platform because of its protected location from clastic inputs (figures 5.1 and 5.2d).

The transition from Lutetian to Bartonian in Southern Jaca shows an abrupt decrease in the SR (from 41 to >10 cm/kyr) coinciding with the passage from foredeep to a wedge-top situation.

During the Bartonian (between 38.0 - 41.3 Ma) the whole area becomes incorporated into the wedge-top depozone, on top of the Gavarnie-Sierras Exteriores thrust sheet. The Bartonian emplacement of Sierras Exteriores thrust sheet is deduced from

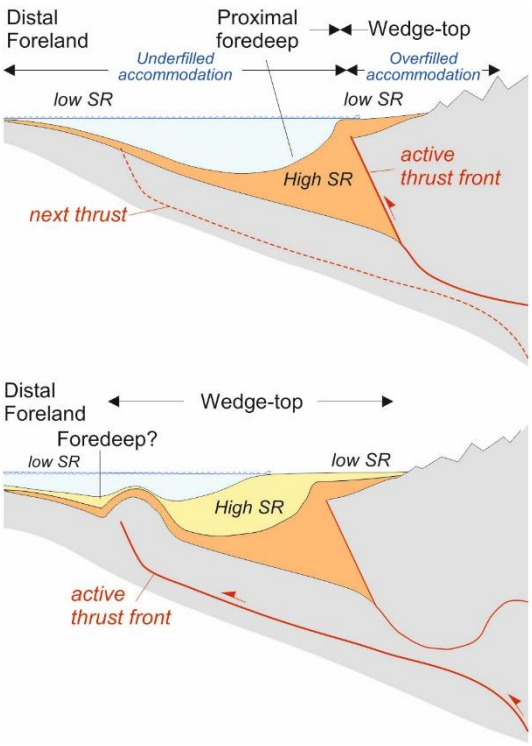

Figure 5.3: Evolution of a foreland basin system where a foredeep with underfilled accommodation is later incorporated into a wedge-top depozone in a thrust-flat position without major uplift. This evolution results in an early wedge-top stage having high SR and relatively low SR in the area where the proximal Foredeep should be developed. Vertical scale exaggerated. (a) Initial underfilled foredeep situation. (b) Wedge-top situation keeping higher SR than other depozones.

the growth of N-S oriented anticlines in the Serres Marginals area (Millan *et al.*, 1994; Poblet and Hardy, 1995; Castelltort *et al.*, 2003) before ramp development during the Oligocene (Labaume and Teixell, 2018). Immediately following the transition to wedge-top, SR reach their highest values (105-115 cm/kyr) in northern Jaca basin. However, in general, SR show a sustained decreasing trend as expected for basins incorporated onto the wedge-top.

A possible reason for the high SR in the wedge-top (Ainsa during Lutetian and Northern Jaca Bartonian to Priabonian) is as the deformation propagates toward the foreland, a new frontal thrust (or its related anticline) does not immediately produce a new proximal foredeep depozone with a relatively higher SR. The sustained moderate-to-high SR during the initial wedge-top situation may be associated with the structural arrangement of the AOZ and front of Sierras Exteriores thrust sheet, with thin-skinned cover units that are deformed in a thrust-flat position with horizontal displacement and uplift mainly restricted to the frontal anticline axes (figure 5.3). In this wedge-top depozone, regional subsidence related to the load from the emplacement of basement units in the axial zone (figure 4.10) is not

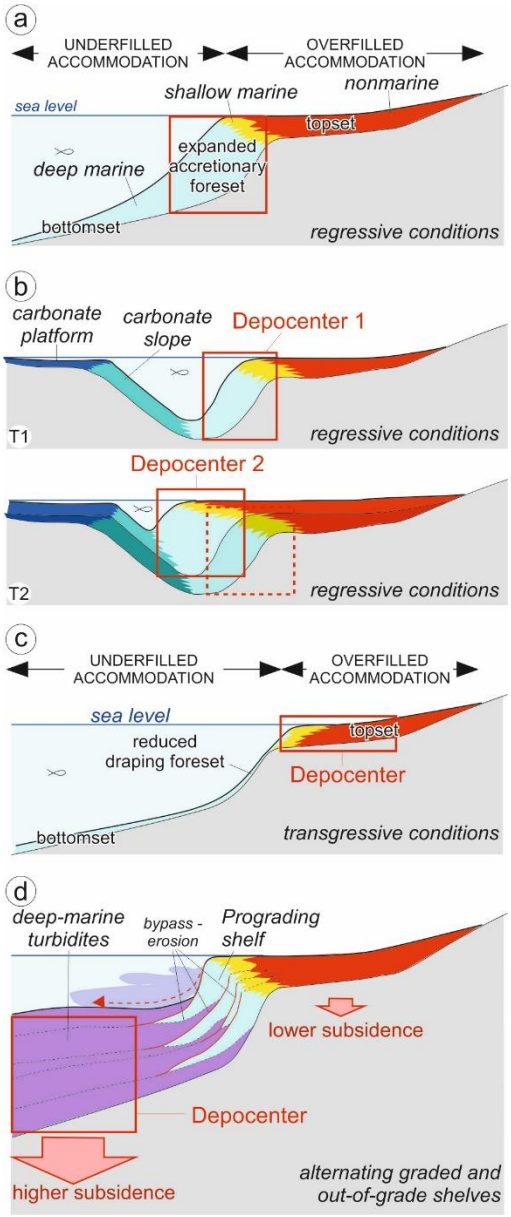

Figure 5.4: General conceptual models showing the geometry of shelf margins parallel to the main sediment transport direction from non-marine to deep sea areas showing the location of the sedimentary depocenters in different situations: a) Normal regression in a graded prograding clastic shelf; b) Evolution of two successive regressive episodes where the advance of the graded clastic shelf produces a retreat of the carbonate facies; c) Accretionary transgression; d) Normal regression with steepening of the shelf margin and tectonically induced subsidence preventing the overfilling of the accommodation of the sedimentary trough. This last case shows the alternating deposition of deep marine turbidites during out-of-grade episodes and the progradation of clastic graded shelfs in more stable periods.

reduced or counteracted by the thrust sheet uplift (figure 5.3), keeping SR higher in the synclines and lower in the anticlines.

5.1.2 Basinward migration of depocenters due to shelf clinoform progradation during regressive conditions

A feature observed in four of the profiles illustrated in figure 5.1 is an important increase in SR associated with the deposition of shallowing-upwards clastic shelf and deltaic successions (*e.g.,* C20r to C20n at MD or C18r and C19n in GA and YB). Conversely, when deltaic complexes grade upwards to subaerial sediments, a reduction in SR occurs. The first increasing and later decreasing trend in SR is likely related to the shelf clinoform progradation (figure 5.4a) and coeval basinward displacement of the boundary between underfilled (below sea level) and overfilled (above sea level) accommodation areas (Catuneanu, 2017). These kinds of progradational shelves are graded margins whose profiles are in equilibrium with depositional and erosional processes operating within each environmental regime (Ross *et al.*, 1994). They display a sigmoidal shape where the largest sediment accumulation takes place in the foreset environments (Kuehl *et al.*, 1986; Alexander *et al.*, 1991; Walsh *et al.*, 2004), which in progradational episodes are expanded, developing accretionary active clinoforms (Patruno and Helland–Hansen, 2018). In regressive and progradational settings, the topsets are overfilled accommodation domains which are close to equilibrium with the base level. Thus, SR in topsets will be mainly controlled by relative sea level (base-level) changes. In the foreset, the accommodation is directly related to the water depth of the marine basin (figure 5.4a), and it could be increased or reduced by relative sea level variation. Therefore, SR in prograding foresets is higher than in the topset because here, in addition, the depth of the marine basin is added. In the bottomset SR are usually lower than in the foreset (figure 5.4a). Despite that typically both sub-environments share a similar accommodation, the reduced supply of sediments (since they are located in an underfilled accommodation area) diminishes SR in the bottomset.

In the S-profile (figure 5.1), the basinward migration of the Ainsa-relative depocenter can be directly linked to a clastic shelf—from C20r, to C19r in the MD log (figures 5.1, 5.2b and 5.2c). During C20r low SR (21 cm/kyr) are related to carbonate slope settings. At chron C20n, the clastic input arrives to the area, filling the basin trough (close to 500 m deep; Pickering and Corregidor, 2005), first with deep-marine sediments and then with shallow water delta front and shelf facies. The introduction of this clastic sediment is associated with a sharp increase in SR (from 21 to 68 cm/kyr). During C19r, as the Sobrarbe deltaic complex progrades NW, the MD log is no longer located in the foreset,

but rather in the topset area. This vertical evolution from foreset to topset in the MD log is associated with an SR reduction (from 68 to 24 cm/kyr). At this stage, the depocenter in Ainsa has migrated westwards (CM log, 45 cm/kyr), as sketched in figure 5.4b.

In a similar way, in Northern Jaca (YB log) there is a well-documented increase-to-decrease of the SR related to the Sabiñánigo and Belsué-Atarés deltaic progradation, from C19n to C17r (N-profile, figure 5.1). Deltaic foreset progradation during C18r and C18n show high SR (105 cm/kyr and 115 cm/kyr respectively), while in previous (deep sea bottomset) and later stages (topset fluvial and alluvial) SR are lower (53 cm/kyr). The high SR recorded here is also related to the infill of a marine basin with water depths of several hundreds of meters during clastic shelf progradation.

Contrasting SR during C21 are also observed between the Tremp-Graus (ES log, >30 cm/kyr), showing a shallowing-upward trend as a result of the progradation of a clastic shelf, and the Ainsa and Southern Jaca carbonate platform and slope environments (SR between 3 and >12 cm/kyr).

5.1.3 Uniformization of SR and widening of depocenters due to transgressive conditions

During the latest Lutetian (C19n) we observe an exceptional uniformization of the SR (between 53 and >23 cm/kyr) in both Ainsa and Jaca areas (figures 5.1 and 5.2d). This resulted from a drastic decrease in SR in the Northern Jaca depocenter and an increase in SR in Ainsa and Southern Jaca. Because Chron C19n is relatively short (0.234 Myr, Gradstein *et al*., 2012) the averaged SR may reflect short-term variations on sediment supply and/or accommodation due to relative sea level or subsidence variations. In Ainsa, a significant part of C19n is represented by the deposition of the Buil nummulite banks carbonate unit (Dreyer *et al.*, 1999; Callot *et al.*, 2009) (figure 5.5) embedded between highly progradational clastics of the Sobrarbe deltaic complex (Dreyer *et al.*, 1999, Grasseau *et al.*, 2019). This unit records a transgression larger than 12 km (Grasseau *et al.*, 2019) and a landward displacement of the boundary between underfilled and overfilled accommodation areas. This carbonate platform deposition above and below regressive deltaic complexes implies an Accommodation/Sediment Supply ratio (A/S) higher than that deduced for the long-term general regressive trend of the TJB infill. This relative high A/S may be responsible for trapping more clastic sediments in the topset area. In this situation, clastics are only able to fill the accommodation space in the proximal areas (figure 5.4c), resulting in reduced foresets if present (draping passive clinoforms in Patruno and Helland–Hansen, 2018) and delivering less sediment to deep areas. As a result, in the LS log at Tremp-Graus there

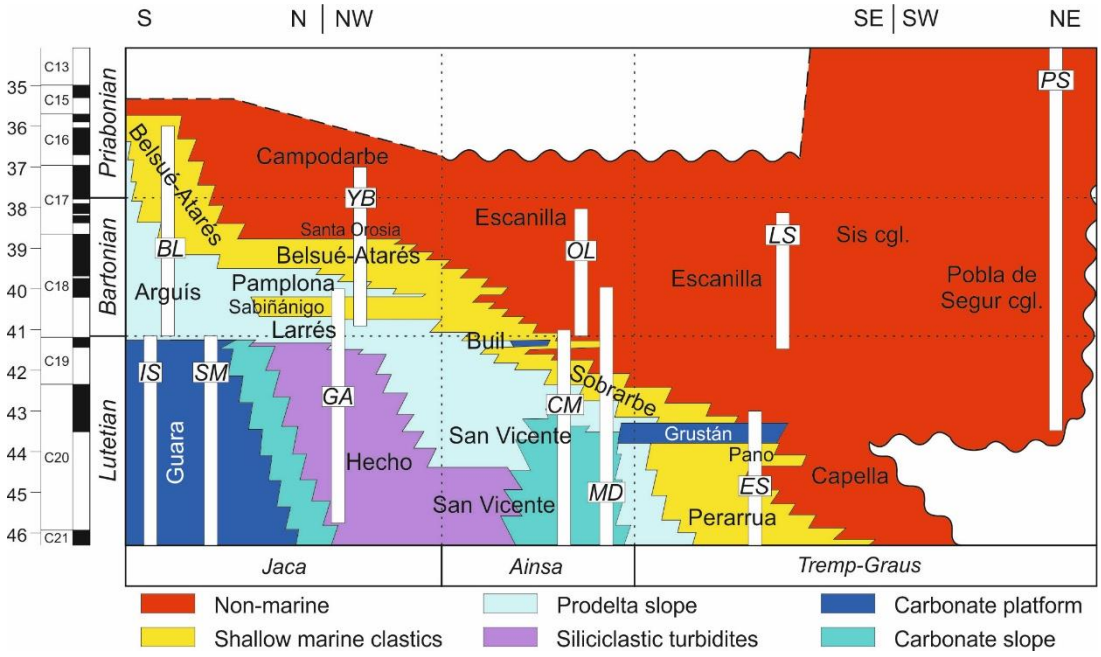

Figure 5.5: Stratigraphic diagram of the Tremp-Graus-Ainsa-Jaca basin, with the different stratigraphic units, approximate location of studied logs and sedimentary environments.

are higher SR than for the subsequent stages (figures 5.1 and 5.2d). In Southern Jaca, sediment-starved cleaner waters than for Northern Jaca and Ainsa favored higher SR in the carbonate platform. The increase in accommodation in Southern Jaca at this stage can be attributed to the incorporation of the area into the foredeep as the plate flexure advanced southwards.

During Chron C20r SR were relatively uniform when compared with previous and later regressive episodes (S-profile, figure 5.1). This period also shows a transgressive trend as marked by the vertical evolution from non-marine to transitional and finally marine carbonate platform deposits in the ES log.

5.1.4 Long-term depocenter in Northern Jaca and Ainsa

As indicated in the previous sections, we have documented a long-term persistent depocenter in Northern Jaca (figures 4.13, 5.1, and 5.2). This depocenter accumulated a thick succession of deep marine sediments during Lutetian and early Bartonian times (from before 43.5 to *ca*. 40.8 Ma). The progradation of a graded clastic shelf (figure 5.4a) as deduced from the observations in the Ainsa Basin (S-Profile, figure 5.1) cannot explain the presence of this depocenter. This configuration implies a high subsidence area in Northern Jaca that accommodated higher SR in deeper bathymetries than the more proximal and shallow marine areas (Ainsa and Tremp-Graus), which were accompanied by a high clastic input. The high subsidence can be directly related to the proximal foredeep depozone situation of Northern Jaca, during the Lutetian (N-profile,

figure 5.1) associated with its location in the footwall and close to the deformation front (figure 5.2). Considering the fluviodeltaic and slope complexes in Tremp-Graus-Ainsa as the main feeders of the Northern Jaca area (figure 5.2) (Mutti *et al.*, 1985; Mutti, 1992), a high clastic sediment flux toward deep marine areas in the context of an out-of-grade or erosional margin (Ross *et al.*, 1994), is needed to produce the resulting high SR (figure 5.4d). This sediment flux from areas where SR were lower (figure 5.2) implies erosion and/or bypass in the foresets. In the Ainsa slopes, these two processes have been documented as related to slope instability (sliding and slumping) and to the erosional and sediment transport capacity of turbidity currents, both operating at a variety of scales and frequencies. These resulted in turbidite channel complexes of the mixed erosional-depositional type (*sensu* Mutti and Normark, 1987; 1991), large-scale canyons (Mutti *et al.*, 1985), or submarine truncation surfaces (Arbués *et al.*, 2011). This large-scale out-of-grade period deduced for the whole Lutetian shows higher-frequency cycles of graded margin progradation-outbuilding that progressively oversteepening until reaching the situation of an out-of-grade margin with upbuilding in deep marine areas; finally restoring the conditions to a graded shelf progradation (as developed by Ross *et al.*, 1994). This cyclic behavior of the clastic margin has been described for the northern Ainsa Basin by Mutti *et al.* (1985) and Arbués *et al.* (2011). Previous studies point to high rates of clastic sediment input, seismicity, and tectonically-driven oversteepening as in Odonne *et al*. (2011), or, periods of relative sea level fall and subaerial exposure of the shelf (Castelltort *et al.*, 2017) as an influence on the oversteepening, destabilization and sediment transfer across the slope. Thus, during the Lutetian (*ca*. 40.8 Ma) the Northern Jaca depocenter received deep water deposition related to the periodically out-of-grade margins, whereas, in Southern Ainsa the deposition records dominant graded shelf progradation episodes.

During the Bartonian, Northern Jaca continued as the main depocenter. At C18r, the clastic shelf progradation reached the Jaca basin, while substituting the deep marine sedimentation in Northern Jaca and the carbonate platforms in Southern Jaca (figures 5.1 and 5.2). At this time, the Sabiñánigo Delta prograded onto a deep water area (Northern Jaca) and the near-complete infill of a water column of several hundreds of meters resulted in high SR associated with the graded shelf progradation (figures 5.1, 5.2, and 5.4a). Following a transgressive episode on top of Sabiñánigo sandstone (Puigdefàbregas, 1975), peak SR of 115 cm/kyr occurred in Northern Jaca during Chron C18n (170 cm/kyr—if subchron C18.1r is considered), related to the graded shelf progradation of the Belsué-Atarés deltaic Formation.

During the latest Bartonian (C17r), the continuous progradation toward the southwest of the coastal systems in Northern Jaca resulted in alluvial deposition in the YB log, a progressive lowering of SR, and the obscuring of the depocenter during the Priabonian (C17n) coeval to the homogenization of the SR in the Jaca and Ainsa sub-basins.

In Southern Ainsa, a relative depocenter between chrons C20n and C18r (figure 5.1), shows SR that first increases and then decreases, an evolution that can be explained with the graded clastic shelf progradation model (figure 5.4a). The arrival of the clastic systems to the MD log coincided with a major increase in SR from C20r to C20n. Noticeably, a coeval increase in SR also affected the Southern Jaca carbonate platforms, which were sheltered from clastic input. This fact points to a widespread accommodation increase (Southern Jaca and Ainsa). The sum of the generalized accommodation increase and the almost complete infill of the depocenter by the prograding shelf resulted in a major increase in SR. At the end of the Lutetian (C19r) the non-marine strata of the Escanilla formation had already filled most of the southern Ainsa sub-basin (figures 5.1 and 5.2). Nevertheless, the Ainsa relative depocenter was still present during C19n and C18r; and this persistence required other factors in addition to the graded clastic shelf progradation.

5.1.5 Unexpected high sedimentation rates in non-marine settings (local tectonics, sediment load, salt withdrawal and regional subsidence distribution)

The graded shelf progradation model (figure 5.4a) predicts a decrease in SR at the transition from foreset to topset settings. However, in a wedge-top context, the topset fluvial areas at MD, CM, and OL logs in Ainsa during C19n and C18r, or YB during C17, were still depocenters (figures 5.1 and 5.2) with SR higher or similar to adjacent downstream areas that were developing deltaic progradation (Southern Jaca). SR were also higher than areas upstream in Graus-Tremp with non-marine sedimentation. A key local factor here was the synchronous tectonic growth of adjacent structures (Boltaña, Balzes, and Mediano anticlines in the Ainsa sub-basin and Oturia thrust and Yebra de Basa anticline in the Jaca sub-basin, see figures 4.10 and 5.2), which could have influenced the local subsidence, sediment supply, or clastic sediment routing or trapping.

At the end of the Lutetian (C19) most of the southern Ainsa basin filled with non-marine sediments of the Escanilla formation. This fluvial system was substituted at a very short distance westward by the Guara Formation carbonate platforms of Southern Jaca (S-profile, figure 5.1). This transition from fluvial and alluvial sediments to carbonate platforms cannot be physically traced due to the present-day interruption of the outcrops of that age along the Boltaña and Balzes anticlines (figure 4.10). The synsedimentary

development of these anticlines from middle Lutetian to lower Bartonian is demonstrated by growth strata and also by paleocurrent patterns (Puigdefàbregas, 1975; Mutti *et al*., 1988; Dreyer *et al*., 1999; Soto and Casas, 2001; Arbués *et al*., 2011; Muñoz *et al*., 2013; Michael *et al*., 2014; Rodríguez-Pintó *et al*., 2016; among others). In the Ainsa basin, the anticline growth forced the clastic systems (turbidite units first, followed by deltaic and alluvial units) to adopt a NNW direction that paralleled the anticlines (figures 5.2c and d). During the growth episodes, in the transition from Lutetian to Bartonian, the originally submarine buried anticlines shoaled in the southern Ainsa basin and produced a temporary barrier, preventing the transit of the clastic sediments towards the west (Bentham *et al.*, 1992; Dreyer *et al.*, 1999; Moss, 2005). As a result, detrital sediments accumulated in the Ainsa basin and carbonate sedimentation persisted in Southern Jaca (figure 5.1). The paleogeographic barrier promoted clastic funneling and an increased transfer of clastics northwards to Northern Jaca Basin (figure 5.2d). The fold growth of Boltaña and Balzes, together with the Mediano anticline (figures 4.10 and 5.2), resulted in a synsedimentary intermediate syncline structure, the Buil syncline (figure 4.10), which established a local depocenter in the center of the Ainsa basin (figure 5.1). The relative high SR for the Buil syncline during C19n and C18r (figures 5.1, 5.2d, and 5.2e) may be the result of interference and feedback among different tectonic and sedimentary factors as shown in figure 5.6. The anticline growth in Boltaña-Balzes generated a barrier for clastic transfer and the location of a simultaneous clastic trough along the Buil syncline (figure 5.6c). The Buil syncline had high SR that caused local sediment load which increased local subsidence, favoring the migration of Keuper salts from the syncline to the

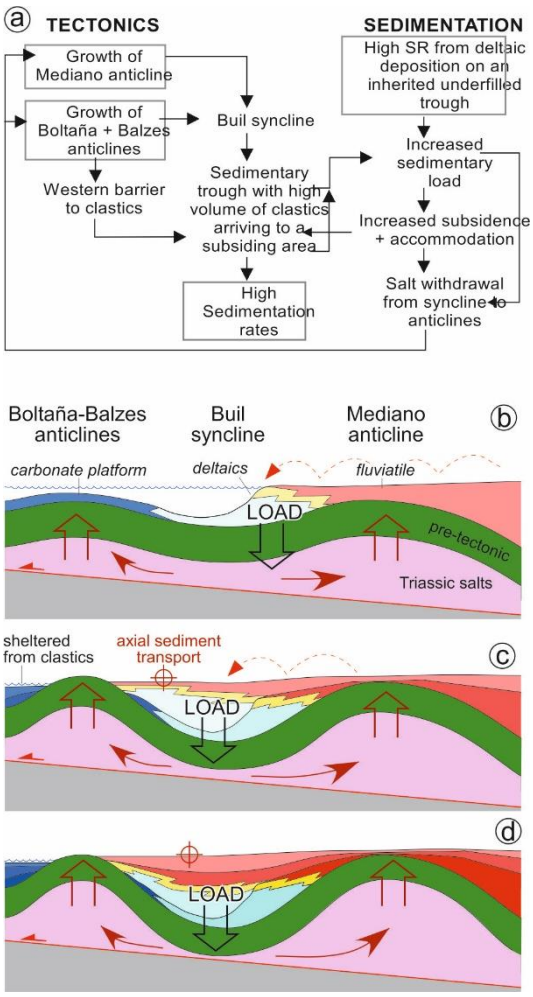

Figure 5.6: Mutual influence and feedback among tectonics, sedimentation, and salt migration as a hypothesis to explain the abnormal SR in the Escanilla Formation in the Ainsa Basin during the uppermost Lutetian and lowermost Bartonian. (a) Flow diagram. (b), (c), and (d) simplified not-to-scale E-W evolutionary sections from C20n (b) to c19n (d).

adjacent anticlines (figure 5.6 a, b, and c) and diapiric structures (Clamosa and probably Naval)— similar to the models presented by Ge *et al.* (1997). Salt migration could reinforce the anticline growth and generate a local salt withdrawal depocenter in the Ainsa Basin. The growth of evaporite-cored anticlines in this region linked to tectonic and sediment load driven salt migration was pointed out by Holl and Anastasio (1993), Soto *et al.* (2002) and Santolaria *et al.* (2016) among others. This situation ends during Chron C18r, when the clastic flux was transferred to the SE over the Boltaña and Balzes anticlines, arriving to Southern Jaca Basin (figures 5.1, 5.2e, and 5.2f).

In the Jaca Basin, during Bartonian and Priabonian, there is a thrust front located to the south at Sierras Exteriores, which developed synchronously with some the thrusts and thrust-related folds to the north (Monte Perdido system, Oturia, and Jaca, figures 4.10 and 5.2). The evolution of the thrusts located north of the Jaca Basin (figure 5.2) produced a southwards-migrating uplift during the Lutetian, Bartonian and Priabonian that resulted in a clastic supply increase of northern origin and the incorporation of earlier foredeep strata (Hecho group turbidites) into the uplifted wedge-top source area (Labaume *et al*., 2016; Roigé *et al*., 2016).

The influence of northern provenance systems is first observed in middle Lutetian Jaca turbiditic unit paleocurrents (figure 5.2c) and extends to at least C17r, interfering with the axial Tremp-Graus-Ainsa clastic sediment routing system. During C17 SR show a significant increase towards north across the Jaca Basin, with much higher values in YB where alluvial sedimentation was taking place than in BL (progradational shallow marine deltaics). This contrasts with the expected SR for prograding shelves, lower in non-marine sediments and higher in prograding clinoforms. We argue this distribution of SR, as seen in the depozones section, is the response to the tectonic subsidence related to the load of basement-involving thrust sheets (Gavarnie-Oturia and Sierras Exteriores) to the north, producing a northwards dipping regional flexure. The increased clastic supply resulting from the merging of the axial and the northern provenance systems produced a southwestwards progradation of the detrital systems. This resulted in a progressive continentalization, restricting the marine sedimentation to the southern the Jaca Basin.

The extremely high SR associated with the evolution from the Belsué-Atarés delta to the Santa Orosia alluvial fan deposits during C18 (figures 5.1 and 5.2f) is interpreted as regional subsidence due to load of basement thrusts, and the progradation of the clinoforms of the Belsué-Atarés deltaic system onto a deep basin floor.

5.2 Tectonics *vs.* Climate in the Belsué-Atarés delta

The study of the Belsué syncline through the model presented on the section 4.3.1 shows that the *Best Fit Simulations* (*BFSs*) are #4, #7, #8 and #19. This section analyzes the parameters resulting from those simulations to determine if the Milankovitch cyclicity of the Belsué-Atarés delta is propagated from the upstream or from the downstream by analyzing the standard deviation of the input parameters and by studying the cycles of the output parameters on the most representative *BFSs*.

5.2.1 Forcing mechanisms of the sediment distribution

Belsué model *Best Fit Simulations* (*BFSs*) are #4, #7, #8 and #19 (see section 4.3.1, 5th step). On those *BFSs* the amplitudes of the *unknowns* set for the Monte Carlo simulation are analyzed. As the unknowns have different amplitude units (meters for the eustasy, m^3/s for the water discharge and km^3/Myr for the sediment supply) it is necessary to convert the amplitude values of the Milankovitch oscillations to dimensionless amplitudes (*i.e.* between 0 or no-amplitude and 1 or maximum amplitude).

Forcing mechanisms determined by the standard deviation

For this model the inquiry was to understand if sedimentary trends where mainly forced from the upstream parts of the system or from the downstream, so the more similar are the amplitude values of the *BFSs* between them, the more accurate is the amplitude value. This accuracy on the amplitude values points out that the unknown is highly determined on the *BFSs*, indicating that this unknown is forcing the sediment distribution at the *BFSs*.

The similitude between the *BFSs* amplitude values can be measured from calculating the standard deviation (SD). If calculated the SD for each of the three dimensionless unknowns, eustasy is 0.216, water discharge is 0.269 and sediment supply is 0.090 (table 5.1). What the SD values indicates is that sediment supply is the more influent

Simulation	***Eustasy***	***Water Discharge***	***Sediment Supply***
#4	1.000	0.211	0.842
#7	0.790	0.421	0.948
#8	0.527	0.369	0.737
#19	0.579	0.842	0.895
Average	0.724	0.461	0.856
SD	0.216	0.269	0.090

Table 5.1: Dimensionless values of the amplitude of the *best fit simulation*. 0 represents no-amplitude and 1 the maximum amplitude of the oscillations.

unknown, followed by the eustasy and finally by the water discharge. Considering that the average SD values for all the 20 simulations is 0.311, it can be calculated by the means of the equation 5.1 that the sediment final distribution is forced by sediment supply (61.8%), followed by eustasy (26.5%) and finally the water discharge (11.7%).

$$X\% = 100\frac{SD_i}{\sum_{N=i}(\overline{SD}-SD_i)} \quad (5.1)$$

This equation is designed here to obtain percentages from the differences between the values for the four *BFSs* (SD_i) and all the values on the model ($\overline{SD}$). The percentages obtained and indicated here are only a reference, because there are not enough values to consider this data accurate. Nevertheless, there is a hierarquization of the three unknowns and differences among them are significant enough to trust the qualitative results.

Forcing mechanisms determined by the output parameters

To ensure a more trustful determination of the forcing origin, a secondary analysis can be done studying the output parameters. As there is more than one *BFS*, in order to simplify the analysis, it can be first determined which one is the most representative. To assess this, two arrays of curves have been analyzed; first there are the curves coming from the input data (figure 5.7), whose amplitude have been determined by the latin hypercube distribution (section 4.3.1, 3rd step). Also there have been analyzed some properties of the output in the control log position at the model (figure 4.18) (Garcés *et al*., 2014; Valero *et al*., in prep.). The output properties studied are the bathymetry, sedimentation rate, water flow and gravel+sand proportion (figure 5.8).

The process for calculating the most representative *BFS* assumes that the target simulation is the most similar to the average from the four simulations curves. So, from the values of the four *BFSs* curves, an average curve has been calculated. Then is calculated the error between each simulation and the averaged value to determine the most similar simulation to the average. From this calculation, the simulation #7 results the most similar to the average. Thus, this simulation will be studied as the most representative of the *BFS*. The calculations can be found on the digital suppl. data 3.

The inputted Milankovitch fluctuations (figure 5.7) are evaluated respect the oscillations found on different parameters of the control log (Garcés *et al*., 2014; Valero *et al*., in prep.). So, eustatic fluctuations are compared with the bathymetric response, sediment supply is compared with sedimentation rates and water discharge is compared with water flow. Additionally, the response of the gravel+sand parameter is also evaluated, as it has

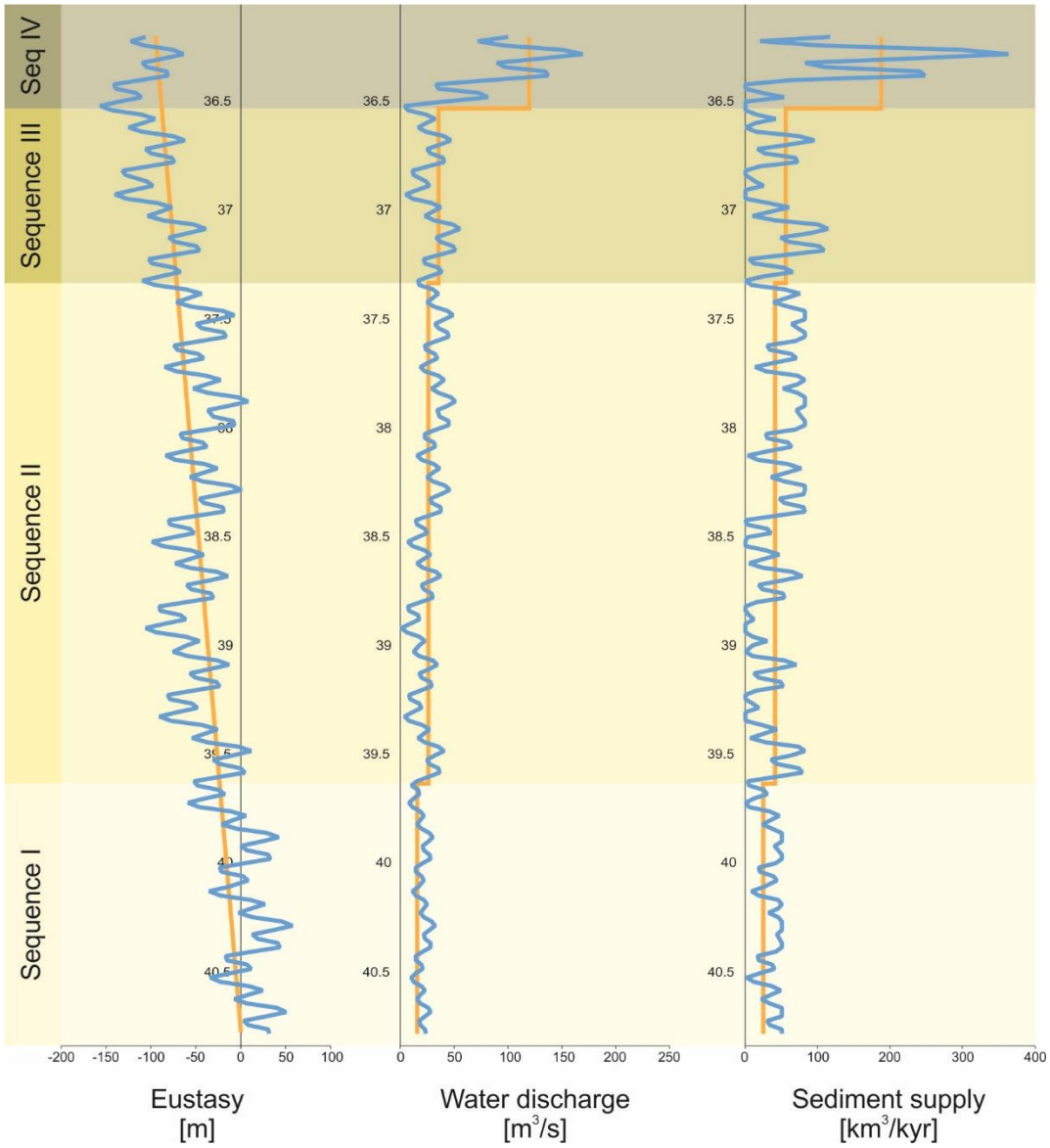

Figure 5.7: Curves of the input parameters for #7 simulation. Orange lines represent the average values calculated for the sediment supply and the water discharge and the general deepening upwards trend for the eustasy (see text for more details). Blue lines stand for the real input after corrected for the #7 Milankovitch cycles amplitude. For sediment supply and water discharge values are capped on 0, as they cannot be negative. Also are capped to the double of the average to maintain the average values. Vertical scale represents age in Ma. Sequences I to IV are the stratigraphic subdivision by Millan *et al*. (1994).

been stablished as the control parameter on the sensitivity analysis (section 4.3.1, figure 4.19).

Response of the simulation #7 on the inputted Milankovitch fluctuations (figure 5.8) shows a relative attenuation on the original input data on the gravel+sand, sedimentation rates and water flow. This attenuation reveals that those parameters are controlled mainly from the point at which sediment enter the model, as they are upstream

parameters. Bathymetry is not attenuated respect input as directly depends on the eustasy, that applies equally at all points of the model.

Bathymetry, but, is differentiated from the inputted eustatic fluctuations because eustasy shows a swallowing upwards trend that is not present on the bathymetric response, where actually there is a slightly deepening upwards trend. This is an intentional response of the simulation because the model does not compute sediment compaction and to correct this sediment compaction it has been introduced this deepening upwards trend to the inputted eustasy. Changes between the different sequences (Millan *et al*., 1994) do not represent strong differences on the bathymetric curves.

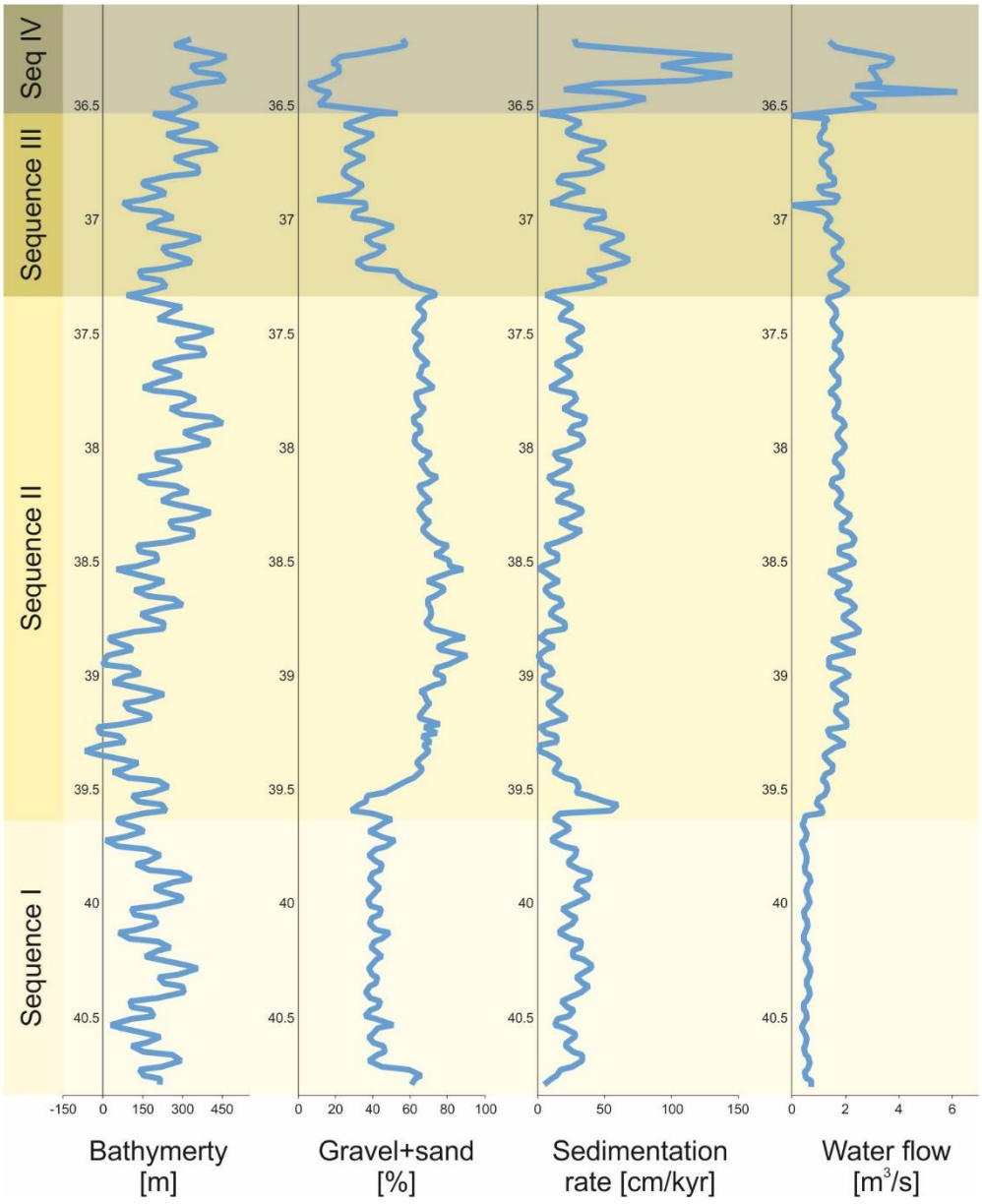

Figure 5.8: Curves of the output parameters (bathymetry, gravel+sand, sedimentation rate and water flow) along the control log position for #7 simulation.

Nevertheless, there are slight trend changes on Bathymetry that can be related with those sequence changes. Those changes are probably related to the response on the subsidence changes plus changes on the other unknowns. The inputted eustasy have a uniform progressively changing trend that does not depend on the sequence changes, but sediment supply and water discharge average values are different depending on the sequence (figure 5.7). Sediment supply and water discharge Milankovitch fluctuations are superimposed to the average values of those input parameters, as sediment supply is calculated from the volume between the Vidal-Royo *et al*. (2011) surfaces and water discharge is calculated in reference to the sediment supply (4.1 equation). Also, subsidence changes between the different sequences as consequence of the dependence of subsidence from the Vidal-Royo *et al*. (2011) surfaces.

Sedimentation rates are useful to compare the effect on the sediment supply variations to the final result. Sedimentation rates show the same oscillations than on the input, but those are attenuated by the distance from the input point. This attenuation is consequence of the distance from this input point and the log sampling, and is also consequence of the sediment 3D expansion through the basin. Sedimentation rates show strong changes when crossing the sequence Boundaries from Millan *et al*. (1994). Those changes are more significant than in the case of bathymetry, for the reasons exposed above. As there cannot be negative sediment supplies, the inputted trend is capped on the 0-sediment supply. Also the values are capped on the double of the average of the sediment supply, following the minimum and maximum determinant factors of a modulation equation (see the digital suppl. data 3 for more details). This limitation of values is done to keep the sedimentation average values respecting the calculated volumes on Vidal-Royo *et al*. (2011) model.

Water flow behaves very regular within all the sequences, except for the sequence IV, where it shows some strong peaks. These peaks were not that strong on the inputted data. Those peaks can be related to the influence of the sediment supply over this water flow parameter. Changes between sequences represent also changes on the water flow response, but those are not as significant as the sedimentation rates changes.

If compared the gravel+sand response with the other responses, it has a comparable behavior to the sedimentation rate. This is coherent with the driving mechanisms of the Milankovitch signal propagation primarily from the upstream and secondary from the eustasy defended above, as the sedimentation rate depends on the accommodation space of the basin and the available sediment. The main differences of the gravel+sand and the sedimentation rates are that they are inversely proportional. This indicates that

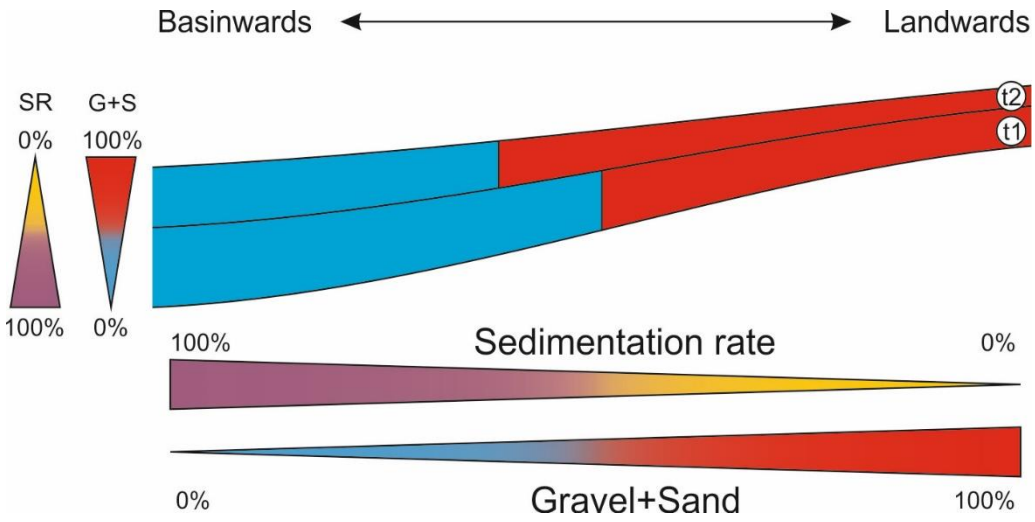

Figure 5.9: Scheme of the transition between the gravel+sand and the shale parameters on the Belsué model. This transition shows an inversely proportional relation between sedimentation rate and the percentage of the coarse fraction. As here it is studied the middle upstream part of the system, transgressive periods are related with higher sedimentation rates and lower percentage of gravel+sand sediments.

there is a higher proportion of shale when there are high values on sedimentation rate (figure 5.8). This is because we are looking at a small part of the system. On the middle upstream part, higher sedimentation rates are related with transgressive periods with less by-pass, retaining the passage from coarse to fine sediments in a landward position respect the regressive situation. As the inputted sediment supply changes, the gravel+sand – shale line moves back and forward to adapt to this situation (figure 5.9).

Tectonic subsidence role on the forcing mechanisms

Those qualitative results differ with the model proposed on Valero *et al*. (in prep.), where, it is demonstrated that sedimentation on the syncline depends on accommodation space shifts. The model here presented is strongly driven by the tectonic subsidence inputted. Removing the Milankovitch cyclicity, it is obtained a sediment distribution changing in the same way that tectonic subsidence (figure 5.10). If it is calculated on the figure 5.10 central position the A/SS ratio, it is clear that as there is a higher value, there is less grainsize and *vice versa* (table 5.2). The sediment supply values are the average values, from the 3D model (Vidal-Royo *et al*., 2011) and the subsidence values are calculated by the equation 5.2 on the control log position.

$$A/SS = \frac{(B_f - B_i) - T}{SS} \qquad (5.2)$$

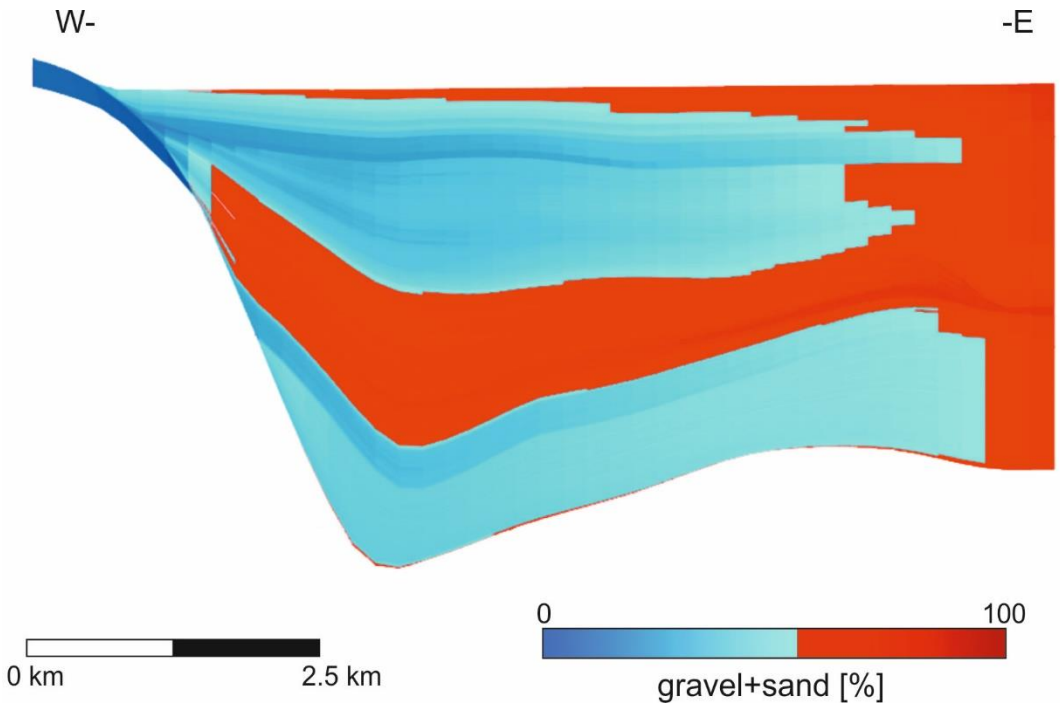

Figure 5.10: Representative section of a simulation with 0 amplitude on the input parameters, to show the subsidence effect over the model. Colors represent the coarse component of the sediment. Vertical scale 3 times the horizontal scale.

On equation 5.2, the A/SS is the accumulation / sediment supply for a given interval, SS is the sediment supply, B_f is final bathymetry, B_i is the initial bathymetry and T is the thickness.

Subsidence defines the accommodation space together with the eustatic changes. This fact may have dimed the final influence of the eustatic processes modeled, making that the accommodation space in the model mostly depends from subsidence. The direct consequence of lowering the role of eustasy is that sediment supply, controlled from the upstream, has more influence over the final result.

Reducing the influence of subsidence on this numerical model is complicated, as the sedimentary routes are strongly controlled by the position and growth of the

	Initial Bathymetry [m]	***Final Bathymetry [m]***	***Thickness [m]***	***A/SS ratio [m/km^3]***
Sequence IV	384	365	204	3.3
Sequence III	246	384	366	11.3
Sequence II	203	246	425	5.1
Sequence I	106	203	242	11.3

Table 5.2: A/SS relation on the Belsué model control log position when there is no Milankovitch oscillations induced on the model. Sequences of Millan *et al*. (1994)

synsedimentary Pico del Águila anticline (Millan *et al*., 1994). A possible reduction on the subsidence dependence of this model could be achieved by extending the model eastwards, until arriving to the area that is permanently emerged. This emerged part can help stabilizing the final sediment distribution by providing a reference coastline and decreasing the dependence of the model on the local tectonic subsidence.

5.3 Sediment routing systems on the Tremp-Jaca basin

The analysis of the General Flow Model (GFM) indicates that the *best fit simulation* is the #5 (table 4.10). Here, the results of this simulation are analyzed for first identify the sediment transport routes and then explain which are the conditioning factors to those routes. Finally, on the simulation is also discussed some other observable features, such as the sediment distribution and the geomorphological features.

5.3.1 Sediment routing analysis

To define the sedimentary routes, it has been analyzed the water flow and bathymetric evolution through space and time to stablish a direction and deduce the sediment routes for each chron (figure 5.11). The sediment routes are organized hierarchically on three levels in function of the reliability of each path. Thus, in the figure 5.11, primary routes are the ones with streams higher than 1200 m^3/s at some point of their length, the secondary routes are mainly controlled by currents between 1200 m^3/s and 300 m^3/s and the tertiary routes are the ones recognizable with streams of less than 300 m^3/s.

Detection of artifacts and misfits

All those routes have been compared with other parameters calculated in the model (*i.e*. subsidence, sedimentation rates and lithology) to find the possible flow artifacts and enhance the quality of the routing maps. Also the maps are compared with real paleocurrents for the same purpose. In the following paragraphs there is a discussion on the uncertain sedimentary routes found on the model.

The general trend observed in all of the maps shows that most of the sediment routing departs from the northeast and go to the west or northwest until it leaves the basin. This routing is coherent with the routing deduced from field data.

In the southernmost part of the C17r there is a primary route that goes from southeast to northwest that contrast with the routes observed on the C18n and C17n, where this route does not exist. Additionally, there are different northeast to southwest sediment routes that arrive to the problematic route in the middle lower half of the map (southwest). The area where take place this abrupt change of direction is a flat area (figure 5.12) with no

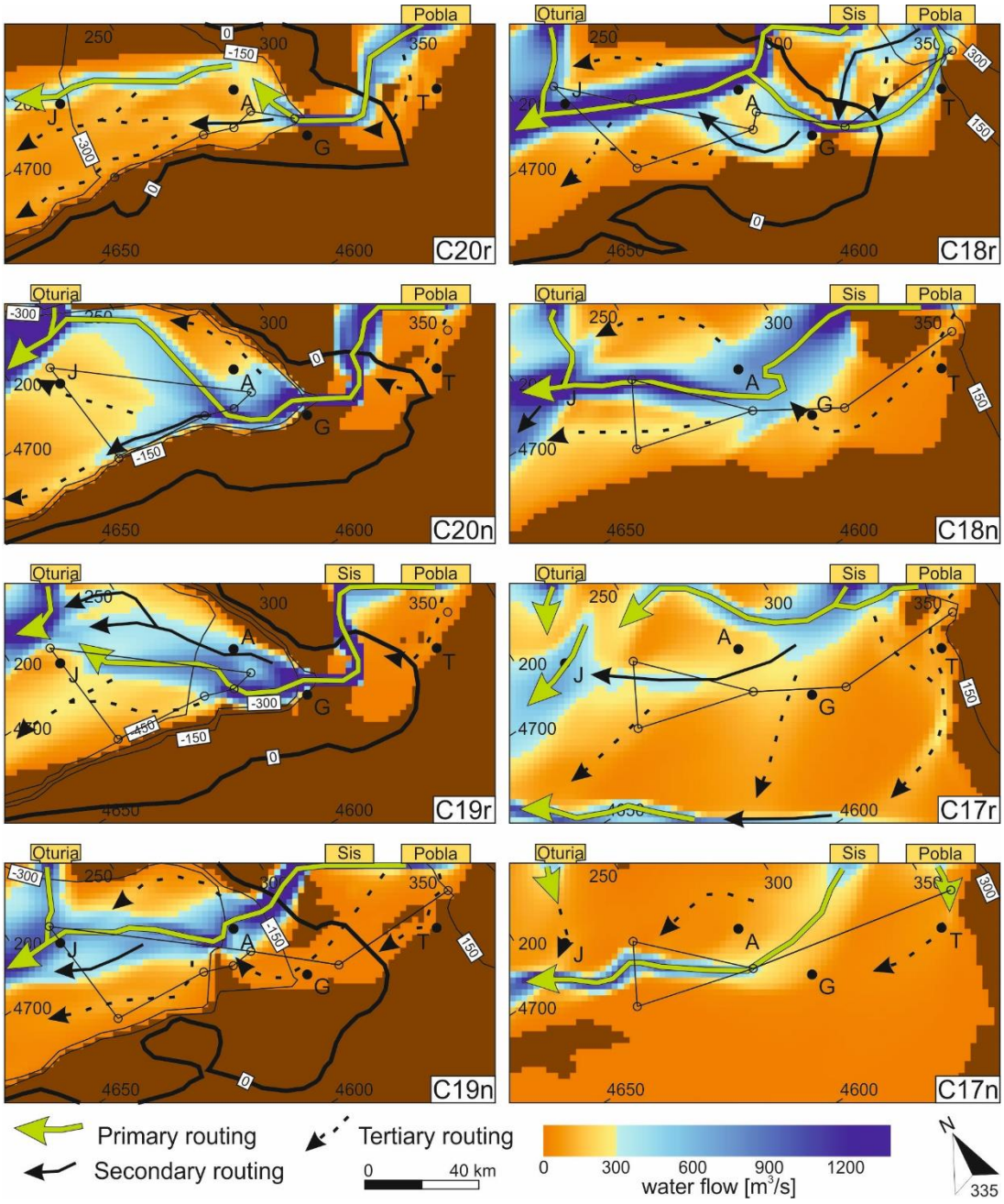

Figure 5.11: Water flow maps for each chron of the simulation #7 in the GFM. Over the map the different sediment routes are interpreted, hierarchizing them according their flow energy. Oturia, Sis and Pobla are the main sediment source points. Black lines are bathymetric isolines, coastline is represented by the thick 0 m line. Blank dots and the lines connecting them represent the position of the control logs. Coordinates are in km in the UTM reference system. The shortening related to thrust advance and clockwise synsedimentary rotation of the Ainsa Basin and External sierras structures has not been considered. J: Jaca, A: Ainsa, G: Graus, T: Tremp.

significant changes in subsidence (figure 5.13) or lithology (figure 5.14). Presumably, this route direction is consequence of the “wall effect” of the model boundaries. The configuration of the model made that the boundaries does not allow the sediment overflow, so the boundary acts as a wall that captures all the sediments. This condition

reorients the sedimentary routes to the basin exit, located northwestwards. Those south-east to north-west sedimentary routes have been discarded as they are the product of a model definition artifact.

The sediment routing is also tampered by the input data. This model has been constructed using the sedimentation rates calculated on this thesis, converted to volumes (Vinyoles *et al*., 2020; section 4.2.1 and figure 5.2). The data used is spatially situated on the present-day location, but this position changed during deposition as a consequence of the differential shortening associated to the Pyrenean thrusts (Muñoz, *et al*., 2013). This resulted on the progressive clockwise rotation of the central part of the studied area (Ainsa subbasin) whereas most of the Jaca and Tremp-Graus kept its original E-W trend. The consequence of this rotation is that the map expression of most of the sediment routes for the studied interval show a Z-shape with E-W trends in Tremp-Graus and Jaca and SSE-NN in between (Ainsa) (figures 5.2 and 5.15) (Vinyoles *et al*., 2020) As the input data is not palinspaticaly restored, the sediment routing should be forced to follow this atypical Z-shape route in the model. Thus, in the model we find a Z-shaped sediment routing coincident to the deduced in Vinyoles *et al*. (2020) however, the original shape of these routing systems was much more straight before deformation.

Forward modelling is based on processes, so sedimentation depends on the model geometry. This implies that if the geometry of the model is not the original geometry, processes cannot replicate the sedimentation conditions. Is this why the main route on the C20r, C20n, C19r and, probably, in the C18r follows a Z-shape, similar to the routing in figure 5.2 maps, changing its course to the north after passing Graus. Nevertheless, in the pivot point there is a minor route that follow the natural sediment distribution, continuing straight. This situation has been solved by eliminating the straight flow towards west and west-northwest on C20r, C20n and C19r and lowering the hierarchic level of this routing on C18r.

Finally, on the sediment input point the sediment routing tends to go in a southwest, to west and even northwest direction for the first *ca*. 30 km (figure 5.11, C20n to C19n and C19n to C17r). This routing is parallel, or almost parallel, to the boundary occupying only the first pixel. The measured paleocurrents in the input point on the literature indicate a roughly south direction (Vincent, 2001 and Barsó, 2007). So, the calculated average west-directed routing it is considered an artifact, that has been corrected by considering the tertiary or secondary current in a south direction as the main flow for the affected chrons (C20n to C18n) and the flow parallel to the boundary is not considered a real

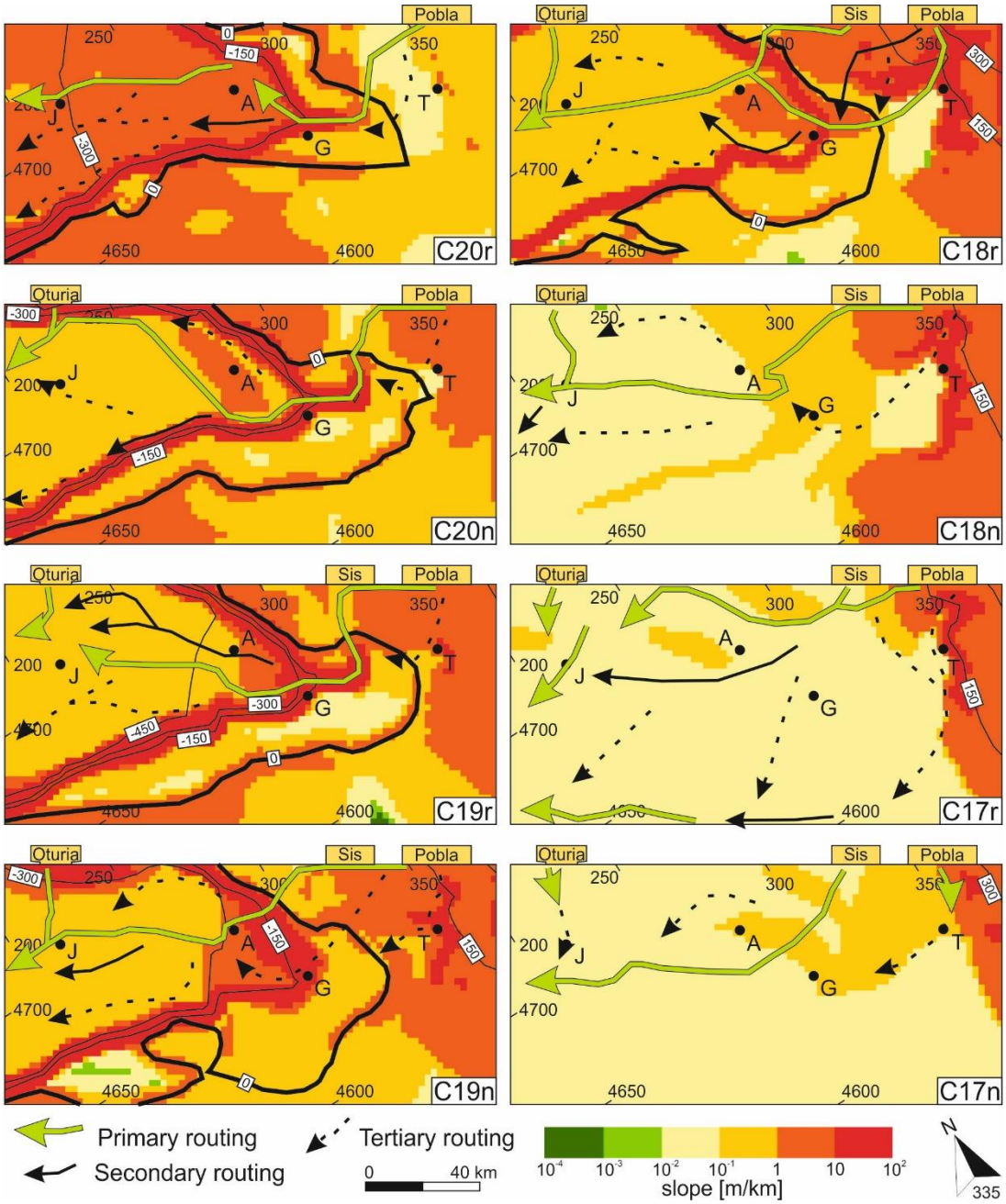

Figure 5.12: Slope maps for each chron of the simulation #7 in the GFM. Oturia, Sis and Pobla are the main sediment source points. Black lines are bathymetric isolines, coastline is represented by the thick 0 m line. Coordinates are in km in the UTM reference system. The shortening related to thrust advance and clockwise synsedimentary rotation of the Ainsa Basin and External sierras structures has not been considered. J: Jaca, A: Ainsa, G: Graus, T: Tremp.

sedimentary route. On the C17r the situation is ambiguous and has been left the original calculated route.

Factors influencing and defining the Sediment Routing System

With all those observations made, and the artifacts and misfits considered, the definitive flow model deduced from the simulation is on the figure 5.16. This model it has to be interpreted as the reconstruction of the sediment routing that could take place on the Pyrenees during the studied period. However, the routes indicated on those maps follow the present-day geography of the area after deformation and vertical axis rotation.

The sediment routes defined allows us to discuss about the determinant factors on the sediment routing for this model. Those factors are the slope, subsidence, marine/non-marine character of the depositional environment, and the lithological composition of the basement. Observations on those factors are made over the sedimentary routes on the figure 5.11 as the modeled flows follow the calculated routes and not the real routes.

In this model the sedimentary routes are first conditioned by the tectonic subsidence pattern and then are modulated by other parameters. The subsidence differences between two points are the most important determinant factor of the slope values of the basin surface. So, comparing the sediment routing with subsidence, the sediment routing roughly follows this subsidence pattern, from low to high subsidence areas and following a downslope direction (figure 5.12 and 5.13). But slope is not only determined by subsidence, as carbonate platform building and the stratigraphic architecture of the shelves and their depositional slopes generate the final slope distribution (figure 5.12). So, the combination of subsidence and the stratigraphic architecture builds the geometry of the basin and broadly determines the sediment routing.

The position of the routing in the previous chron also can condition the position of the new routing and its morphology. An example of this situation is the passage from the sediment routing system of C18r to C18n. In the eastern part of the simulation in the C18r there are two routes, one departing from Sis and the other departing from Pobla (figure 5.11, C18r). Those two routes merge together in the north of Ainsa. At the C18n, the Pobla routing is divided in two branches just from the input point. One routing directly merges with Sis entry point and only a tertiary routing follows the west direction, and later meeting the Sis routing between Ainsa and Graus (figure 5.11, C18n). Unless the Sis route is more predominant than the Pobla route, the merging takes place at almost the same point than in the C18r, when both routes where both had the same hierarchical condition.

The behavior of the flow in marine and non-marine settings is also different in the model as consequence of the mean slope changes (figure 5.12). Whereas in marine settings this flow has in average higher slopes, on non-marine environments the flow is usually

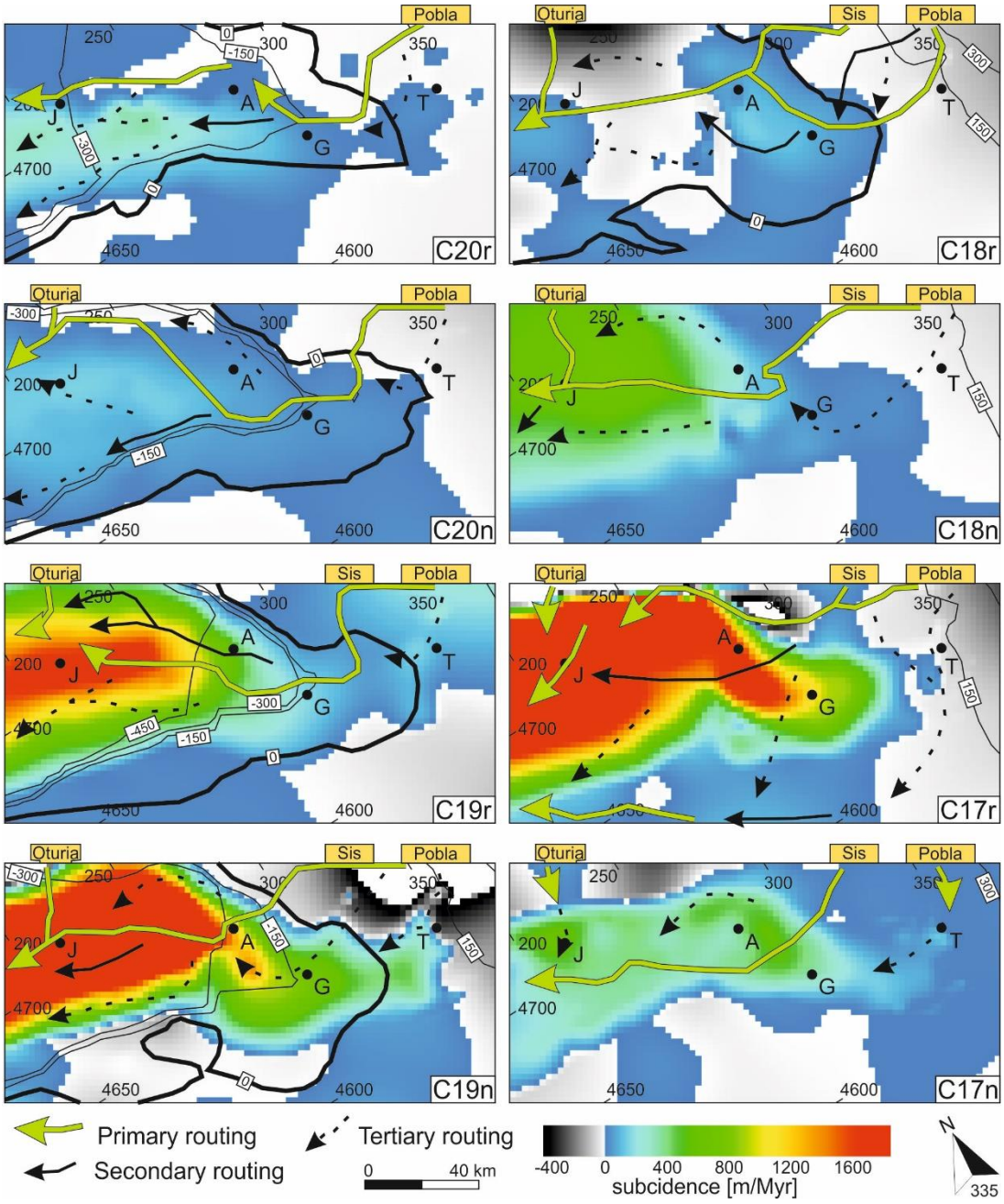

Figure 5.13: Subsidence maps for each chron of the simulation #7 in the GFM. Oturia, Sis and Pobla are the main sediment source points. Black lines are bathymetric isolines, coastline is represented by the thick 0 m line. Coordinates are in km in the UTM reference system. The shortening related to thrust advance and clockwise synsedimentary rotation of the Ainsa Basin and External sierras structures has not been considered. J: Jaca, A: Ainsa, G: Graus, T: Tremp.

in flatter areas. First, in marine settings there is a submarine slope related to the depositional shelf with an associated increased gradient and flow velocity. Furthermore, the basin floor in deeper areas is steeper than the delta plain. All those factors favor the development of faster flows in the submarine environment. This difference on the marine

and non-marine slope is forced by the diffusivity constants defined on the section 4.3.2 of this thesis (table 4.8).

If the sediment routings obtained from the model are compared with the paleocurrents on the literature (Puigdefàbregas, 1975; Vincent, 2001; Barsó, 2007; Arbués *et al*., 2011; Michael *et al*., 2014; Roigé *et al*., 2016; and unpublished data from the UB researchers), they show to be coherent in most of the cases (figure 5.16). The inconsistent paleocurrents are mainly on the onshore areas, probably as consequence of the impossibility of this model to capture the higher sinuosity of the non-marine routing for the model resolution. On C17r and C17n, the paleocurrents suggest that the main routing registered could have a southern path than the recorded on the model (figure 5.16).

On marine settings, one of the discrepant paleocurrent is located on the C20n, east of Ainsa. At that position there is a paleocurrent with a western direction when the calculated routing has a northern direction (figure 5.16, C20n). This paleocurrent direction was deduced from lithological proxies, but the field measured paleocurrent direction on the Ainsa location perfectly matches the model. Also is inconsistent the paleocurrent between Jaca and Ainsa at the C18r that has a southwestwards direction, perpendicular to the routing calculated (figure 5.16, C18r). This second discordant paleocurrent could be equivalent to the tertiary route found on the south, suggesting that the calculated routing has to be displaced to the north.

5.3.2 Sediment distribution

The sediment distribution of the simulation can be described from the SR and the lithology maps in figures 5.14 and 5.15.

Sedimentation rates distribution

The SR distribution allows to make a first classification from the erosion/sedimentation evolution along the different areas and time. For similar slope values, on the emerged areas the model tends to erode more than in the submerged part, where there is more sedimentation (figure 5.12 and 5.15). This situation follows the underfilled/overfilled accommodation model of sedimentation (Catuneanu, 2017). In all the chrons that sedimentation is marine and non-marine (C20r to C18r), the depocenter is located below the marine portion of the basin in all the cases. At the overfilled accommodation situations with only non-marine deposition (C18n to C17n), the depocenter is located on the northwesternmost part of the model, indicating that the real depocenter of the system is located basinwards of the *high confidence area* (figure 5.15).

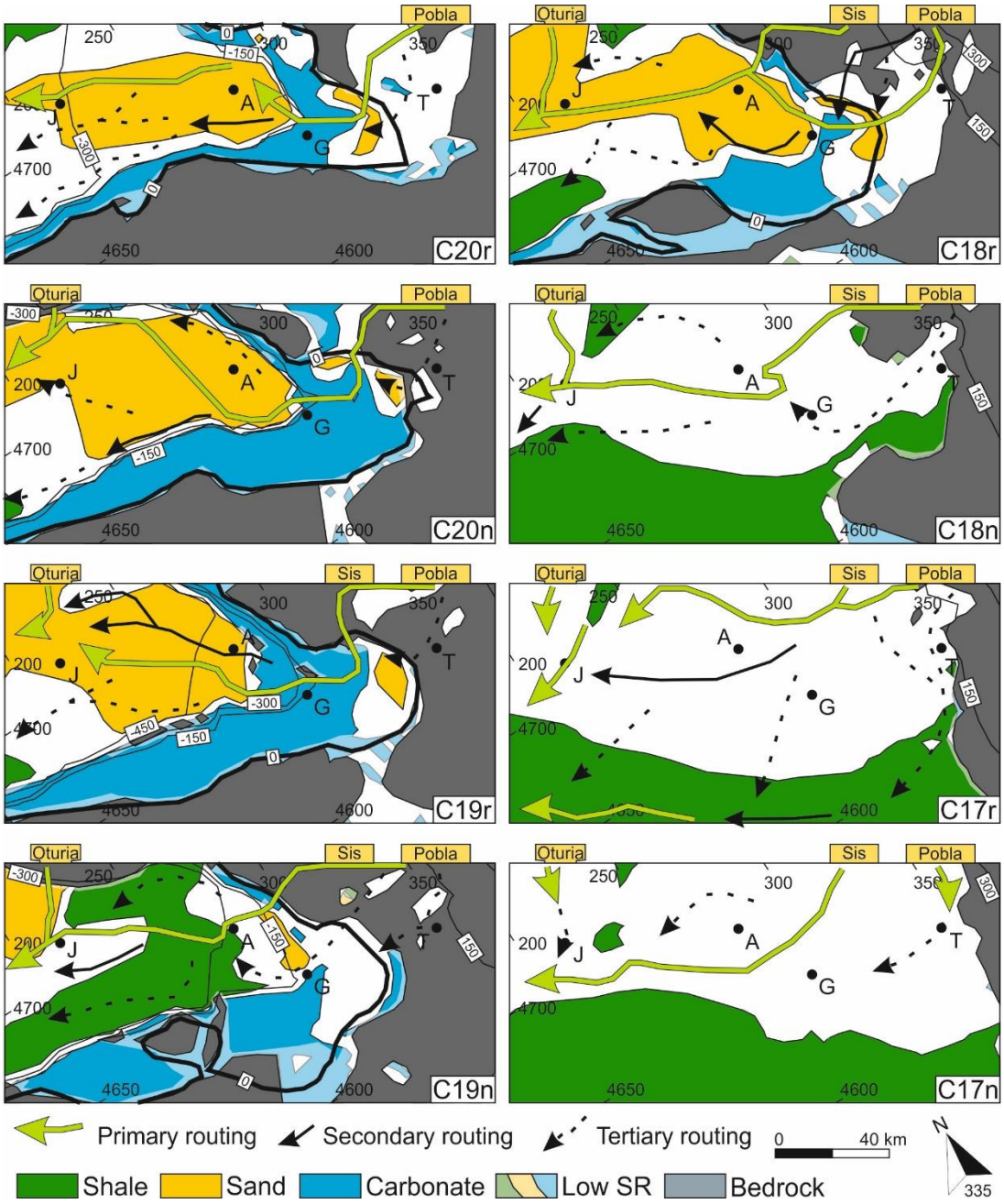

Figure 5.14: Lithological maps for each chron of the simulation #7 in the GFM. Those maps are interpreted from the sediment percentages extracted from the model. When the percentage of a sediment class is over the 60%, then it is interpreted with the correspondent color. When none of the sediment classes is over the 60%, the area is left blank. The sedimentation rates map has been considered to indicate low sedimentation and erosive areas. Oturia, Sis and Pobla are the main sediment source points. Black lines are bathymetric isolines, coastline is represented by the thick 0 m line. Coordinates are in km in the UTM reference system. The shortening related to thrust advance and clockwise synsedimentary rotation of the Ainsa Basin and External sierras structures has not been considered. J: Jaca, A: Ainsa, G: Graus, T: Tremp.

At the depocenters the predominant lithology is sand in all the cases. Figure 5.14 shows that the depocenters on the chrons C18n, C17r an C17n correspond to unknown lithologies (white areas on the map). Additionally, those chrons are on an overfilled

accommodation situation, so the real depocenter is located basinwards and may have a sandy composition in all the cases.

The passage from underfilled to overfilled accommodation situation has also consequences on the sediment accumulation on the basin. The southwestern area of the simulation was erosive during all the model until the non-marine sediments reach this position. SR changed from being an erosive area, to sediment more than 10 cm/kyr (figure 5.15). This situation may be related to the sediment retention by the model boundary.

On the underfilled accommodation area, depocenters are located on the basin floor, when it is present on the model (C20r to C18r). The C19n situation is an exception, because here the depocenter is displaced in a position between the coastline and the slope, filling the previous relief on that area. This is consequence of a transgression taking place on this area at that time. On the simulation maps, this transgression may not be that evident because it seems that the coastline is displaced to the sea, but there is also a displacement on the coastline to the south and is also relevant the differential subsidence on the depocenter and on the coastline area (figure 5.13). The increase on the SR registered is similar to the observed in Vinyoles *et al*. (2020) (figure 5.1).

In general, depocenters are close to the zones with more energetic water flows, with the exceptions of the C20n and the C19n. At these two stages the routings that arrive to the depocenters are not primary. This situation may suggest a mass transport deposit situation, with a huge displacement of sediments to the depocenter that does not involve a huge water displacement when the main flow passes away. This is an issue that should be addressed on the future by doing more experiments.

Sediment composition distribution

From the compositional point of view, this model only uses three different lithologies: sand, shale and carbonate. These three lithologies are expressed as percentages for each pixel. In the model, when one of the three components exceed the 60% of abundance its color is attributed to the pixel (figure 5.14). The areas with a no predominant sediment are left blank. Lithological maps (figure 5.14) have been corrected using the SR maps (figure 5.15), to delimitate the areas with erosion (dark grey) and the areas with SR lower than 7.5 cm/kyr (pale lithologic colors).

The distribution of the siliciclastic sediments is logical and respects the distribution found on the field in most of the cases. This distribution drastically changes on the passage from an underfilled accommodation setting to an overfilled setting. In an underfilled

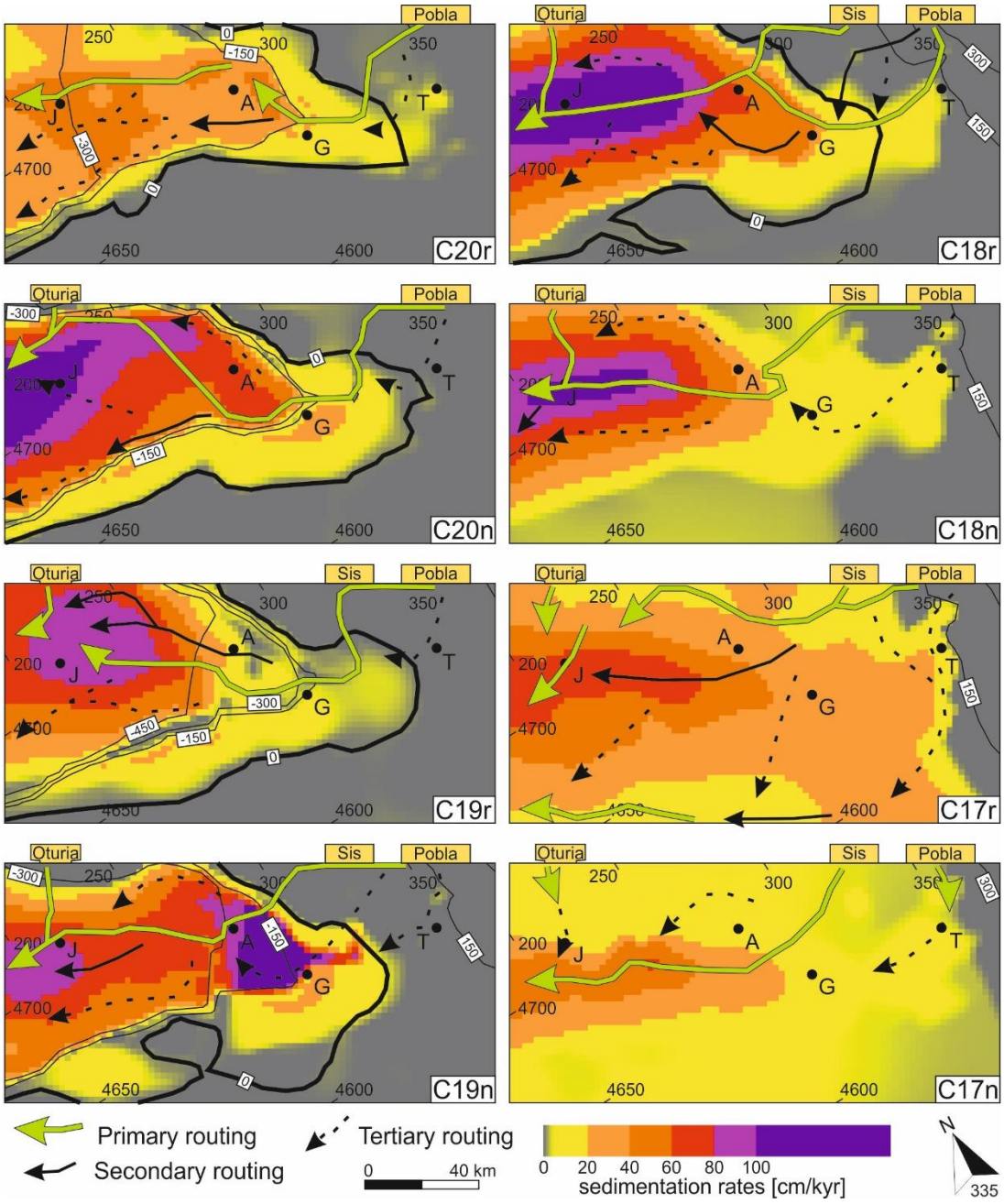

Figure 5.15: Sedimentation rate maps for each chron of the simulation #7 in the GFM. Oturia, Sis and Pobla are the main sediment source points. Black lines are bathymetric isolines, coastline is represented by the thick 0 m line. Coordinates are in km in the UTM reference system. The shortening related to thrust advance and clockwise synsedimentary rotation of the Ainsa Basin and External sierras structures has not been considered. J: Jaca, A: Ainsa, G: Graus, T: Tremp.

situation in regressive conditions there is a homogeneous distribution of the sand above the basin floor, from the depocenter to more marginal areas of the model. Shales are scarcely represented and are mainly present in low proportions, but not predominating. On the C19n transgression there is a retreat of the sand on the center zone to the two depocenters and in between both depocenters there is a spreading of shale. The

disconnection of the two depocenters fits with an out-of-grade situation, like the discussed on the section 5.1.4 of this manuscript (figure 5.17).

After the continentalization of the simulation, in the C18n, there are only areas with high predominance of shale, the other lithologies at the overfilled accommodation chrons are minority. Nevertheless, sand is still predominant over shale on the depocenters.

On the C17r there is the abnormal sedimentary route at the southeastern part of the model, discussed above. But if studied, this current has the particularity that being of more than 300 m^3/s and despite being in areas with SR close to 20 cm/kyr, there is only shale sedimentation, with no sand. In any of the other primary sedimentary routes there is not shale sedimentation. The only other exception is the C19n transgressive, for the out-of-grade configuration. This C17r primary route on the shale may be consequence of being part of a flat area (figure 5.12) and being composed by the addition of multiple tertiary sedimentary routes. Those tertiary routes arrive to this position with a low content of sand, an abruptly found the simulation boundary that acts as a wall, causing a rapid sedimentation of the sediment carried. As stated above, this current is consequence of a numerical artifact.

The Guara formation carbonate platforms are represented at the southwest part of this simulation. Those platforms are present from the initial steps of the model to the C19n. This chronology fits the datings on the area (Rodríguez-Pintó *et al*., 2012b; Silva-Casal, 2017). But to the center and northeast of the model there is an over-representation of carbonate platforms since they are not significant or present in that area. The spreading of those platforms on the model is a consequence of the sedimentary flux canalization on the simulation that takes place at the central region. As the model also was not dealing with wave action, there is nothing that can obliterate the carbonate production of the northern area in shallow marine areas not directly affected by the channeled flux.

5.3.3 Geomorphology

The geomorphological features of this model are the result of the combination of the subsidence (figure 5.13), the stratigraphic architecture (topset-foreset geometry…) and the depositional slope. Subsidence has been defined as an input parameter and conditions the available space and the overall geometry of the modeling box. Depositional slope directly depends on the diffusivity constants (summarized in table 4.8) applied to the model. Those have been set to reproduce a slope of 0.5 m/km in non-marine sedimentation and 15 m/km in marine sedimentation. The stratigraphic architecture is quite difficult to control on a forward stratigraphic model, as it depends on many other factors as carbonate platform building, sea level position, flow energy,

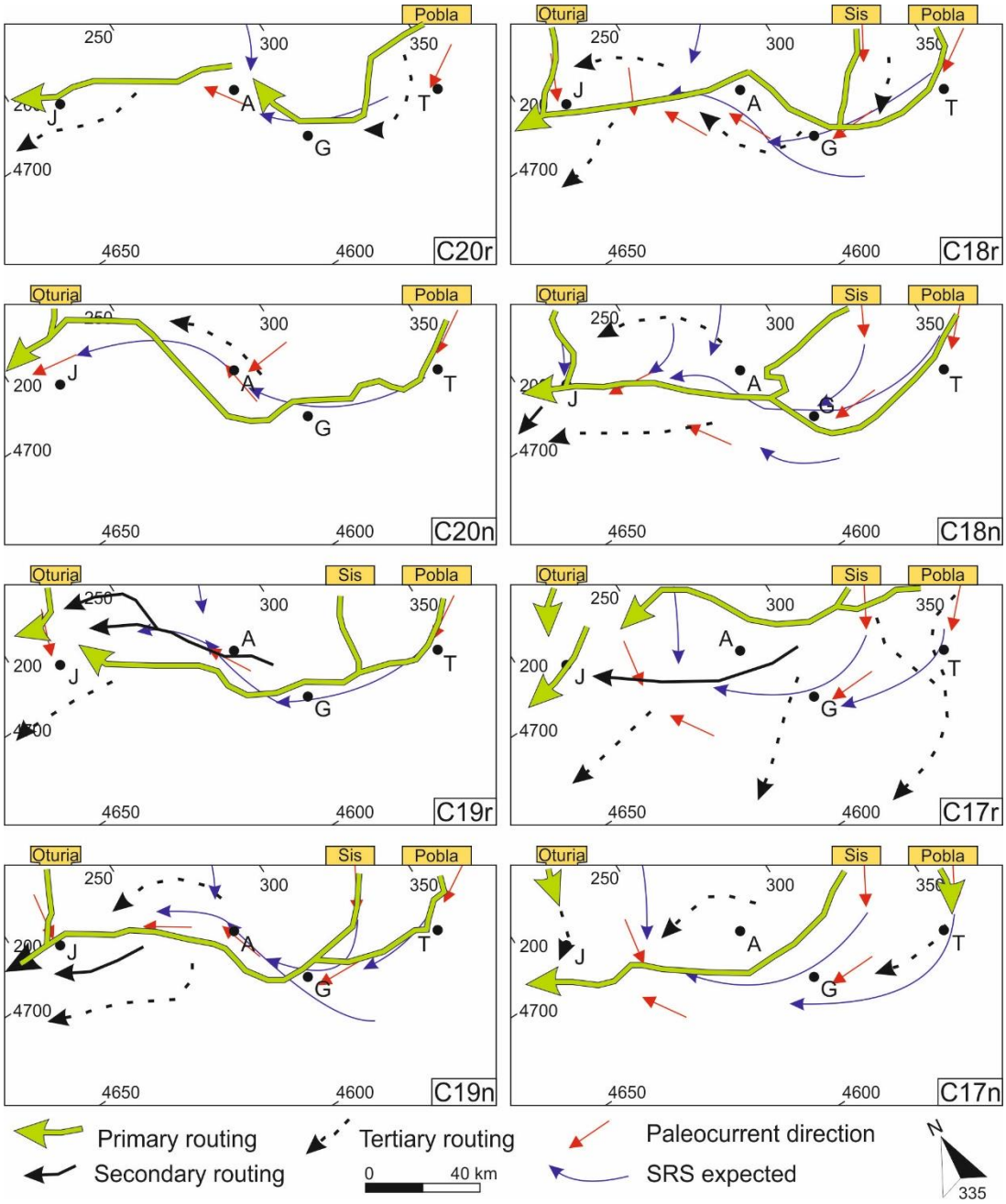

Figure 5.16: Sediment routing maps for each chron in the GFM. The sediment routes are extracted from the figure 5.11 and modified to correct the numerical artifacts (see text for more details). Oturia, Sis and Pobla are the main sediment source points. Black lines are bathymetric isolines, coastline is represented by the thick 0 m line. Coordinates are in km in the UTM reference system. The shortening related to thrust advance and clockwise synsedimentary rotation of the Ainsa Basin and External sierras structures has not been considered. Paleocurrent data from Puigdefàbregas (1975); Vincent (2001); Barsó (2007); Arbués *et al*. (2011); Michael *et al*. (2014); Roigé *et al*. (2016), and unpublished data from the UB researchers. Expected sediment routing systems are from the figure 5.2 (Vinyoles *et al*. 2020). J: Jaca, A: Ainsa, G: Graus, T: Tremp.

available sediments in the flow… This set of factors made geomorphology of the model difficult to control.

The marine sedimentation can be divided on three geomorphological areas on this model: the basin floor, the slope and the shelf.

The **basin floor** is the deeper part of the model, with maximum bathymetries ranging from *ca*. 480 m on C19r to *ca*. 130 m on C18r (figure 5.12). The average basin floor slope is between 10^{-1} and 1 m/km when it is in equilibrium. On C20r there is a higher slope on the basin floor (1 – 10 m/km) because it has not reached yet the equilibrium state of the model. During regressive periods, the basin floor sedimentation is dominated by sand (figure 5.14, C20r to C19r). On the transgressive period there is an increase of the shales (figure 5.14, C19n). The sedimentary routes on the basin floor tends to diversify and the stream loses part of the energy that shows upstream.

The **slope** is characterized for displaying the highest inclinations of the model. These range from 10m/km to more than 10^2 m/km, up to 3 orders of magnitude higher than the basin floor. Its average bathymetry is between 380 m and 10 m and the slope width is of *ca*. 9 km in average. On the slope of this simulation, a canyon is developed on the position where the primary flow crosses it (from C20r to the C19r) near the position of Graus. At that time on Graus, the non-marine Capella formation was being deposited (figure 5.5), whereas in the model there is submarine slope sedimentation. This happens because unless the coastline is well adjusted on a broad view, does not exactly reproduce the same trajectory than the observed on the field data. From a lithological perspective, the model in C20r and C20n shows a slope acting as a transition zone between the shelf, dominated by carbonatic deposition, and the basin floor, where sand is dominant. On C19r carbonates arrive to the slope and displaces the sand basinwards. But during the transgressive interval of C19n the carbonates retreat landwards, and the slope acts again as a transition zone between those carbonates and the shale. Sedimentary routes roughly follow a direction perpendicular to the slope, following the maximum dip. Sedimentary routes tend to group in less routes than upstream and form the aforementioned canyon from C20r to C19r.

Finally, the third geomorphologic area on the marine sedimentation is the **shelf**, a flat area adjacent to the coastline which includes the shallow marine sedimentation. The shelf inclination ranges from 1 m/km to 10^{-3} m/km and have a different width if measured on the northeastern part, that being the active deformation zone is narrower, and even not present. In the southwestern part, the width is *ca*. 20 km. In the model the sedimentation of the shelf area is dominated by carbonates, but there are minor sand concentrations near the coastline coinciding with some sedimentary routes, suggesting

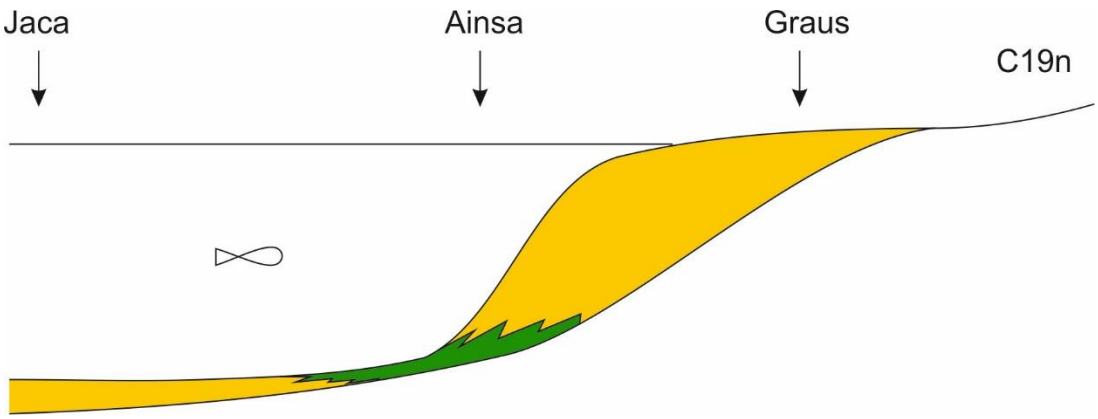

Figure 5.17: Scheme of the out-of-grade situation on the C19n transgressive, representing the sedimentation rates with thickness and the lithology with color.

the development of deltas. Sedimentary routes are very energetic at the shelf, with flows over 1200 m^3/s.

The non-marine sedimentation slopes are very variable, but mainly depend on the uplift of the areas. The higher slopes in the non-marine areas are correlated with the subsidence map (figures 5.12 and 5.13). There is a big dispersion on the slopes, ranging from 10^{-4} m/km to 10^{2} m/km, but the natural evolution at the areas where there is not an important tectonic slopes are between 10^{-2} m/km and 10^{-1} m/km. Deposition on the emerged areas depend on the distance from the coastline. From the C20r to the C18r the emerged land is relatively close to the non-marine part of the model and in the non-marine part there is mainly erosion. The only sedimentation that takes place is a mixture of siliciclastics. From C18n to C17n, the erosive areas are smaller and there is an area on the central part with a compositional mixture of siliciclastics and to the south there is an extension of shales.

From those observations it is highlighted that comparing the output maps (*i.e.* water flow, slope, lithology and sedimentation rates) with the subsidence map, subsidence creates the general trend that controls the sediment distribution. But this trend is then modulated by fluctuations in other parameters. For example, the important subsidence at C17r does not create more accommodation space, as observed on the SR and in the slope maps. Actually, there is a decrease of SR and slope from the previous situation. This can be explained by the efficiency on trapping sediment on the C18n and the short duration of the C17r chron (0.288 Myr).

Another relevant observation is the presence and the effect of the canyon located near Graus from C20r to C19r. As stated above, this canyon does not exist at that time on the geological record, as at this position was taking place non-marine sedimentation. Close

to the NW there were submarine canyons in the Ainsa basin. Unless its position is not correct, the distance between the expected position and the calculated position on Graus is coherent enough with the model resolution, especially taking into account that the whole model is of 466 km length.

Another interesting feature about this canyon is that gets silted at the same time of the Buil transgression, at the C19n. This infilling is highlighted on the SR maps, where an increase of the SR following the shape of the canyon can be observed. The infilling lithology is a mixture of siliciclastic and carbonatic components. This canyon was excavated in the carbonate platform on the area and is unconfined at the bottom of the slope, where there are no more carbonates.

5.4 General discussion on the research

This final section of the discussion includes general thoughts resulting from integrating all the parts of the thesis. First there are some reflections about the conditioning factors on the sediment routing, dividing them between the geometric-dependent factors and the climatic-dependent factors. Then there is a discussion about how the sedimentation rates behaves on the Tremp-Jaca basins and finally there are some thoughts about how can forward stratigraphic models help on understanding highly studied basins and other general ideas about the models done.

5.4.1 Conditioning factors on sediment routing

Sediment routing systems depend on many different factors. Here are summarized on two groups: the geometrical-dependent factors and the climatic-dependent factors.

Geometry

“Geometrical-dependent factors” is a wide category that includes the tectonic effects reflected on the basin deformation by compression/extension, rotation and subsidence, but also includes the subsidence effect due to the sediment load and the depositional geometry of the sediments.

On the studied locations it is highlighted that tectonics have a predominant role on the control of the basin geometry, since the Tremp-Jaca basin is on the southern foreland of the Pyrenees at the time that the orogeny was taking place. There are many publications studying the tectonic deformation of the Pyrenees globally (Seguret 1972; Teixell and Muñoz, 2000; Muñoz *et al*., 2013; Muñoz *et al*., 2018; among others) and the deformation related to local structures (Vidal-Royo *et al*., 2011; Mochales *et al*., 2016; Rodríguez-Salgado *et al*., 2020; Burrel, 2020; among others).

Those active tectonic structures resulted on a permanent deformation of the basin during the studied period, producing constant changes of the depozone distribution (Vinyoles *et al*., 2020) and making more challenging make models with a static grid. This active tectonic context adds a layer of complexity on the sediment routing determination, as in relatively short time lapses the geometry of the basin drastically change.

During the middle-upper Eocene, the Tremp-Jaca basin is under a compressive setting. So here we only can discuss how the compressive structures affect the sediment routing. First, this tectonic compressive setting progressively displaces the depozones basinwards (section 5.1.1 and Vinyoles *et al*., 2020). This displacement of the depozones produces the expansion of the basin area, moving the distal foredeep and forebulge far from the orogen, and also the incorporation of parts of the proximal foredeep to the wedge-top. This incorporation of the foredeep to the wedge-top carries associated a reduction of the sedimentation rates, as the depocenter is displaced to a new foredeep. On the GFM (section 5.3.2) it is observed that this displacement of the depocenter is accompanied by a translation of the routing system, as the sedimentary routes tend to be situated close to the depocenters.

Another characteristic from the routing systems with tectonics is its behavior on settings where there is vertical axis rotation. On the study area there is rotation during the sedimentation time due to the mechanical contrast of the Keuper unit (Muñoz *et al*., 2013). This rotation on the Ainsa basin is of 60° clockwise on the Lutetian (Muñoz *et al*., 2013) and 30° clockwise on the Priabonian, as calculated on the Olsón log of this thesis (figure 4.3). This has a direct consequence, rotating the paleocurrents as are preserved now at days. Those paleocurrents had a westwards orientation as part of a relative straight E-W sediment routing system but the post-sedimentary rotations forced the present day Z-shape geometry. This Z-shape can be clearly observed on the figure 5.2 and also on the figure 5.11, as they are calculated without considering a palinspatic restitution. But the maps coming from forward stratigraphic modeling also show that there is a sedimentary route that tends to follow a straight line to the west, ignoring the expected Z-shape geometry (figure 5.11). This route suggests the position that could adopt the mainstream if the map had been palinspatically corrected, as the model is based on processes and tends to reproduce the natural routing. Thus, after this modeling work, we consider that this issue has an important impact in the models and probably we should have uses palispastic restored maps for our purposes, However, this quickly changing tectonic environment is not easy to replicate with numerical modeling programs as Dionisos.

The local tectonics also modify the sediment routing by modifying the subsidence trends. This is observed in the multiple synsedimentary anticline growth in the basin. One example is the effect of the Pico del Águila anticline synsedimentary growth on the local subsidence on the Belsué model (figure 4.17). This subsidence conditions the sediment distribution by producing different transgressive-regressive cycles that then are modulated by other effects (section 5.2.1). Another example of this can be observed on the Boltaña anticline (figure 1.5), that conditions the sediment distribution, as observed on the sedimentation rates distribution (figure 5.1 and 5.2, from the C19r to the C18r).

Local tectonics also conditions the carbonate distribution. On both stratigraphic models done in this thesis there is a relevant control of the carbonate generation by the different anticlines and local tectonic highs on the area. In the case of the Belsué model, carbonates are only generated on the top of the Pico del Águila anticline, whereas on the GFM the carbonate production is located on the forebulge, at the southeastern margin of the basin, where there is no siliciclastic input. This situation happens mainly on the southern margin but there is also carbonate generation on the northern margin due to the channelization of the flow which prevents most of the shallow marine areas from clastic sedimentation.

The subsidence modification it is reflected on the displacement of the sedimentary routes to follow the maximum slope straight line towards the deepest point.

Sediment compaction also contributes to the total subsidence. Compaction is very variable along the sedimentary basins studied and has been considered when computing the sedimentation rates. As sediment compaction acts progressively and at the same time than the tectonic subsidence, it is difficult to appreciate its influence on the sediment routing. Nevertheless, on this work (section 5.1.5 and Vinyoles *et al*., 2020) it is described how the sedimentation rates on the overfilled Ainsa basin are higher than the expected due to the sedimentary weight. This increase on the sedimentation rates is directly related with the position of the primary routing system.

Finally, the last relevant geometrical conditioning factor is the stratigraphic architecture, as it is not the same if there is shelf progradation of shelf retrogradation. And also change the depositional slopes on the different areas.

Climate

“Climatic-dependent factors” include the direct climatic effects over the sea level (eustasy), changes on the sediment supply, volume of water eroding the surface and

other climatic factors that influence the biological productivity such as water temperature or salinity.

Sea level depending on climate are the variations produced by changes on the Earth insolation that modify the glacial/interglacial situations. Those sea level changes, together with the tectonic subsidence and the sediment compaction, define the available space on the underfilled part of the basin. This relative sea level effect is demonstrated to be less important than the tectonic subsidence effect on the Belsué model (section 5.2), but still determines the final T/R cyclicity.

In other kinds of basin eustatic variations can be more important than tectonic subsidence, as on passive basin margin or other settings where there are no significant tectonic movements. But this is not the case in the Pyrenees during the middle-upper Eocene, an active foreland basin.

Sea level changes modify the coastline position, and this is important for the determination of the overfilled and underfilled accommodation zones of the basin (Catuneanu, 2017). The overfilled accommodation areas have lower slopes than the underfilled and this is conditioning the path of the clastic sediment routing (section 5.3.3).

Another important factor controlled by the climate is the **sediment supply**. Unless this climatic control, there is also an important role of the tectonic uplift on the sediment supply. Tectonic uplift creates relieves that can be eroded. If there is not a relieve to erode, there is less sediment supply. The only sedimentary source would be the sediment coming from the sea level drops. Nevertheless, here it is considered that in a foreland basin there is always a relief providing sediments, but this relieve is eroded with variable intensity depending on the climate action on weathering and denudation.

Also, carbonate production can be considered within the sediment supply concept. This biochemical sediment production depends on water temperature, energy or salinity directly related to climate. This production and the climatic conditionings will depend also on the biological factor of carbonate generation. As on this study carbonate production is only used to create a more accurate geometry on the basin based on field observations, its production will be not evaluated. Nevertheless, if comparing sedimentation rates on shallow marine carbonate areas respect the siliciclastic areas, there is a far lower sedimentation rate on carbonate dominated environments (section 4.2.1; Vinyoles *et al*., 2020). This is the reason why on the forward stratigraphic models on this work it is introduced a conditioning factor than limits the carbonate production when there is a certain amount of sediment turbidity on the water.

The Belsué model directly evaluates the influence of the climatic-related controls as sediment supply, eustasy and water flow on the final sediment distribution. There it is demonstrated that from modeling the sediment supply cyclicity has an important role on the final sediment distribution (section 5.2.1).

Water flow is also evaluated on the Belsué model, being the less important parameter. But water flow also has been evaluated during the calibration of this model in a phase and anti-phase shape of the cycles, to see if there is a direct relationship between the water flow and the sediment supply or they are inversely proportional. The result is that water flow is directly proportional to the sediment supply, what makes sense because as more sediment do you input to the basin, more energy is needed to move it. But following Romans *et al*. (2016) (figure 1.3), most of the climatic processes happen in a shorter time scale than the time resolution used on this thesis. Those processes have a quick compensation time and cannot be evaluated. The only climatic processes that are within the resolution scale are the Milankovitch cycles, evaluated on the Belsué model for understanding the propagation of this signal from the downstream or from the upstream.

5.4.2 Sedimentation rates on the south Pyrenean foreland basins (from Vinyoles *et al*., 2020)

The broad view of the whole TJB is that over a period of about 10 Myr, continuous sedimentation led to a vertical aggradation ranging from 0.9 km (Southern Jaca) to 3.7 km (Northern Jaca). The subsidence required to sustain long-term accommodation in the basin resulted from the combined contribution of tectonic and sediment loads. Sea level rise and fall cycles with amplitudes of a few tens of meters (Miller *et al.*, 2005), had no significant influence at this scale of observation. The generalized regressive pattern resulted from an amount of clastic supply able to progressively fill the basin and evolve from a partially underfilled to an overfilled accommodation setting.

The initial basin topography for the Temp-Graus Basin was inherited from the Montsec-Peña Montañesa thrust sheet geometry (figures 4.10 and 5.2) emplaced during the Ypresian/lowermost Lutetian. The thrust emplacement generated a topographic high on top of the thrust sheet (Tremp-Graus basin / wedge-top depozone). Immediately adjacent (west) of the newly formed Tremp-Graus wedge-top basin was the Ainsa Basin and Northern Jaca Basin proximal foredeep depozone that extended southwards to the topographic high at the southern foreland basin margin (Southern Jaca Basin / distal foreland depozone). Thus, the trough that received most of the clastic sediments during the Lutetian (Ainsa-Jaca) had a steep gradient associated with the initial proximal foredeep situation of the Northern Jaca Basin (figures 5.2 and 5.4d). In the Northern Jaca

foredeep, deep marine sedimentary systems were fed from oversteepened out-of-grade margins. The depocenter extended toward the SE to include the Ainsa area, in spite of being progressively incorporated into the wedge-top.

A secondary shifting depocenter was associated with the progradation of the graded clastic shelf clinoforms parallel to the trough axis. This secondary depocenter was originally located on the wedge-top depozone (first in Tremp-Graus, and then in the Ainsa Basin) and migrated toward the foredeep at a slower rate than the deformation front, reaching the Northern Jaca area at the time it was already incorporated in the wedge-top depozone (Bartonian). The out-of-phase evolution of foreland depozones with respect to the prograding clastic shelf wedge has resulted in complex SR that are not diagnostic of a specific foreland setting.

From the evolution of SR, the distribution of facies belts, and the depocenter position, we distinguish two main stages of the TJB evolution: The Lutetian (C21n – C19n, from 47.8 to 41.2 Ma) and the Bartonian-Priabonian stages (C18r – C17n, from 41.2 to 37.0 Ma).

The Lutetian Stage was characterized by variable SR in a highly compartmentalized basin. From east to west, lower SR or erosion in the Tremp-Graus Basin (10 cm/kyr – >30 cm/kyr) shift to higher rates in the Ainsa Basin (4 cm/kyr – 68 cm/kyr), and to much higher rates in the Northern Jaca Basin (53 cm/kyr – 101 cm/kyr). During this stage, the Southern Jaca Basin started as a distal foreland depozone with low to moderate values (3 cm/kyr – 24 cm/kyr) and later (C19), was progressively incorporated into the foredeep with moderate to high SR (>23 cm/kyr – 50 cm/kyr) (figures 5.1 and 5.2d). The lowest SR are located in the eastern proximal Tremp-Graus area and the Southern Jaca Basin, associated with non-marine (wedge-top environment) and carbonate platform facies (forebulge environment), whereas the highest SR correspond to clastic turbidites and shelf foresets in Ainsa and Jaca. In the Northern Jaca basin, a persistent major depocenter accumulated a thick succession of deep marine sediments in the foredeep depozone under an important clastic input related to the out-of-grade situation of the shelf margin. In the Ainsa Basin, the initial wedge-top situation shows a well-developed wedge-like section, probably inherited from a prior foredeep formed during the emplacement of the Montsec thrust sheet earlier during Ypresian. High SR during the wedge-top stage can be associated with a period of tectonic transport over a thrust flat (figure 5.3) if regional subsidence due to basement thrusting to the north was not counterbalanced by local thrust sheet uplift.

At the beginning of the Bartonian Stage (41.2 Ma) the whole area was incorporated on top of the Gavarnie-Sierras Exteriores thrust sheet (figures 4.10 and 5.2e) as a wedge-top depozone. From east to west SR were low in Tremp-Graus Basin (4 cm/kyr – 13cm/kyr); shifting to moderate rates in the Ainsa Basin (21 cm/kyr – >29 cm/kyr); high rates in Northern Jaca Basin (>31 cm/kyr – 115 cm/kyr); and moderate values in the Southern Jaca Basin (10 cm/kyr – 26 cm/kyr). At this time, the northwestwards migration of the clastic shelf-related depocenter ended with its merging with the persistent depocenter located in the Northern Jaca Basin. This new scenario was characterized by a more uniform SR and the lack of tectonic barriers (*e.g.,* Boltaña and Balzes anticlines). The clastic transfer systems reached the Southern Jaca Basin producing a displacement of the carbonate platform toward the southwest (*e.g.,* Santo Domingo member, Silva-Casal *et al.*, 2019). During the Bartonian and Priabonian, synchronous thrusting occurs at the southern front (Sierras Exteriores) and in the north (Sierras Interiores). A wedge-like section typical of a foredeep developed due to the high subsidence of the northern sector, linked to its footwall position in relation to the northern thrusts and the load of basement-involving units in the axial zone.

As the TJB developed in a foreland basin system, tectonics had the primary role driving subsidence. The contribution of the sediment load to the total subsidence enhanced locally by a feedback process in which salt withdrawal from sediment-filled synclines migrated to adjacent anticlines (figure 5.6). The rising anticlines temporarily confined a part of the basin, producing a relative depocenter. This explains the relative high SR observed in the non-marine Escanilla formation of the Ainsa Basin.

5.4.3 Forward stratigraphic modeling on highly studied basins

Forward stratigraphic models simulate the depositional conditions from the processes that generate them. These types of models are useful to deal with the areas with high uncertainties, as with relatively few information can reproduce plausible scenarios. Nevertheless, those scenarios are indicative of the trends that rule the area, but do not predict precisely the conditions of the modeled area.

Here, forward stratigraphic models are tested on the well-known south Pyrenean foreland basins that where extensively studied since 1970s (writing the basin name between quotation marks on Google scholar returns 698 results). Testing the forward stratigraphic models on a deeply studied foreland basin is useful to understand the potential that this technology offers to reproduce the conditions during deposition time and to predict some non-measurable parameters, as the water flow in absolute numbers.

This extensive knowledge of the basin that is *a priori* an advantage, can become a problem if there is not a good simplification of the data. A frequent problem that can arise is to try to reproduce all the things with a great detail. Details usually come from specific minor features of the basin that are difficult to predict and non-homogeneous along the basin.

Furthermore, forward modeling with the diffusion equation has the problem to set the diffusivity constants, that is a theoretical value with no real equivalent. This diffusivity constant is a problem to calibrate when dealing with many variables. So, simplify the available data in a proper way is important to succeed on the model.

Also, for logical reasons, well exposed and studied structures and sections usually receive a higher attention than structures or sections that are not cropping out or even that have been eroded. This segmentation of the information is difficult to solve but has to be taken into account when dealing with data that do not fit on the model by inexplicable reasons, keeping in mind the Occam's razor principle. When dealing with an outlier section, maybe the model needs a simplification and maybe the outlier section is part of a less important structure o sedimentary feature and could be ignored.

So the importance on the model on a well-studied basin is not the result that outputs, but the parameters that have to be inputted to achieve this result.

In conclusion, forward stratigraphic models in a highly studied basin is an interesting tool to help thinking about the formation conditions and to guess what could be on the eroded and not-exposed areas in a broad way, but those models are not useful to strictly reproduce the buried geometries and sediment distribution, as there are more appropriate tools to do this, like the deterministic models.

General thoughts over the models done

On this thesis are presented two final models obtained after many iterations and trying different approaches, so the original strategy is significantly different than the presented results. For the Belsué model the initial configuration was a cylindrical fold progressively and uniformly growing with a single sediment input coming directly from the west. For the GFM, the first model was also a geometrical reproduction of the basin shape with a poor time control.

The final models are far more complex, and provide more significant results, but building those models has been on both cases more complicated than initially expected. Also there are still some unsolved problems as there are details that can be improved. There is a paradox in model: as more detailed are the models, more useful are, but less robust.

So, it is crucial to find a midpoint between the robustness and detail, so the model is useful and trustful.

One of the key simplifications on forward models is related to the sediment types. Complex interactions between many sediment types, exponentially increase the time for each run and produce many artifacts on the result. It also makes more difficult the interpretation of the results, as having many sediment types and making them difficult to be plot. To face this visualization problem, a script that adds the coarse components (gravel and sand) of the Belsué model has been written (digital suppl. data 2).

But the most complex sediment type to deal with have been the carbonates. Carbonate production has been conditioned to depth and to water turbidity (amount of sediment solved in the water flow). But those to conditionings were sometimes not respected and carbonate production develops where it was not expected.

The position of the anticlines and other structural or depositional geometries strongly conditions the carbonate generation. On the case of the Belsué model carbonate production is mostly located over the limb of the Pico del Águila anticline. On the field data there is no carbonate production at that position, but the carbonate production represents only the 0.48% of sediment volume from the total volume of the *high confidence area*. This is in a range similar to the 2.7% of carbonate thickness found on the control log (Garcés *et al*., 2014; Valero *et al*., in prep.).

Having all the carbonate production concentrated on the Anticline area means that the relief produced by the anticline growth is higher than the expected from the subsidence map inputted and can disrupt the sediment evacuation of the area, as only allows two points for sediment evacuation, one located to the north and another one to the south of the anticline. But this condition has not prevented obtaining successful results from the model.

On the case of the General Flow Model (GFM), there are two abnormal behaviors of the carbonates. On one hand there is the profusion of northern carbonate platforms and on the other hand there is the landwards penetration of marine carbonate platforms during the transgressive periods.

There are no direct evidences of big scale carbonate generation on the northern part of the Ainsa basin. Petrological provenance studies (Michael *et al*., 2014; Roigé *et al*., 2016) does not show significant carbonatic components from a north direction that suggest the presence of significant carbonate platforms at that position. However, in Garcés *et al*. (2020) a northern carbonate platform is deduced for Lutetian times related

to the submarine high in the northern basin margin away from the main clastic routing system and based on some local resedimented carbonate-rich facies with northeastern provenance in Ainsa area. The presence of those overrepresented carbonates on the model is not a problem on the flow computation, because they are relatively thin strata.

During the Buil transgression (C19n) there is the generation of carbonate platforms in the Ainsa basin (Mateu-Vicens *et al*., 2012; Grasseau, 2016). Those can be observed on the figure 5.14, where carbonate generated between Graus and Tremp. Those carbonates of the model are not on the exact equivalent field position, but the model shows that there is carbonate generation southeastwards than in the previous chrons. This expansion of the carbonate generation area is equivalent to the situation that can be found on the field.

Finally, there is the “z-shape problem” on the GFM. This problem arises from the hard data used to run the model, that came partially from the field. On the field there is deformation of the geometry by tectonic effects during the deposition of the studied period (middle-upper Eocene) and this deformation continues after this time. This abnormal shape produces a distortion on the sedimentary paths (see section 5.3.1a). For a forward stratigraphic model would have been more appropriate to use the deposition time and not the present day geometry. This implies an important restitution and simplification work. And this process also would have to be applied to the SR original maps to made a reliable comparison.

Unless the models do not perfectly reproduce the nature, they are precise enough to help in making predictions on the considered issues and even can give hints in additional topics.

6 CONCLUSIONS

Reviewing the Ainsa and Jaca basins age model for the middle and upper Eocene has led to a reinterpretation of the sedimentation rate distributions in the Tremp-Jaca basin, which has implications on the interpretation of depocenter displacement on the Southern Pyrenees. These data have been used to run forward stratigraphic models, providing elements of discussion for wider stratigraphic concepts.

6.1 Age model

An improved age model has been proposed after reviewing the magnetostratigraphic sections from previous studies. Two new sections were sampled at a resolution higher than earlier works, leading to a significant refinement and increased robustness of the age model. First, the upper part of the Escanilla formation in the Olsón section (Ainsa basin) (figure 4.4), has yielded an older age than previously proposed, ranging from chron C18r to C17n. Second, the Pamplona marls, the Belsué-Atarés formation, and the Santa Orosia formation, in the proximal part of the Jaca basin, have been sampled along the Yebra de Basa section (figure 4.8), yielding an age range from chrons C18r to C17n, again an age older than the suggested in previous works.

The two new sections have been integrated with the existing magnetostratigraphic data in order to build a coherent chronostratigraphic framework of the Tremp-Jaca basin. Basin wide integrations of all magnetostratigraphic timelines has led to a reinterpretation of the correlation of the Esera section (Bentham, 1992), a reinterpretation required to fit the facies distribution.

6.2 Sedimentation rates evolution in space and time

The backstripping of selected sections along two transects (N-profile and S-profile, figure 4.10) has allowed to calculate decompacted sedimentation rates that have been extrapolated along the basin. The long-term sedimentation rates range from 8.9 cm/kyr to 96.3 cm/kyr, but on the short term there is a higher variability.

Sedimentation rates observed at the different the depozones have been analyzed. Overall, higher sedimentation rates are observed on the foredeep, compared to forebulge and the wedge top depozones. Nevertheless, on 1 Myr time-scale, a high variability of factors controlling sedimentation rates is observed. First, there is the control of the depositional prism geometry on the transgressive and regressive periods. During the regressive periods, the depocenter is located on the clinoforms (foresets) of the

prograding shelf, whereas during the transgressive periods, the depocenter is located on a topset position.

During the middle-upper Eocene there is a migration of the deformation front towards the south and west of the foreland basin system, and as a result the Tremp-Jaca basin is progressively incorporated to the wedge-top. However, this migration is not found related with a depocenter migration, since the thin-skin tectonics on the deformation front do not create subsidence variations comparable to the one created by the stack of multiple thicker units on the hinterland. For this reason, in some areas the differentiation among depozones is difficult, resulting in very narrow, even absent foredeep in between a highly subsiding wedge top and the forebulge.

Sediment load also has a role on the subsidence of wedge-top units. The substantial accumulation of deep marine sediments in the Jaca basin on the lower Eocene provides high subsidence. In the Ainsa basin the high sedimentation rates period is partly related with sedimentary loading on top the Keuper salts on the Lutetian-Bartonian. This load produced the migration of the Keuper salts towards the core of the adjacent active Mediano and Boltaña anticlines, favoring their growth and enhancing the clastic sediment trapping in the associated Buil syncline.

6.3 Models on the Tremp-Jaca basin

The data provided by the age model and sedimentation rates have been merged with data from previous studies in order to produce two forward stratigraphic models. The Belsué model contributes to the understanding of the Milankovitch cyclicity in a context of deltaic sedimentation on a highly subsiding area. This model shows that cyclicity controlling the transgressive/regressive high-frequency cycles of the Belsué-Atarés delta are predominantly originated upstream (sediment supply), while there is secondary contribution that generates downstream (base level).

The general flow model shows that the clastic sediment routing on the Tremp-Jaca basin can be closely replicated using the sedimentation rates calculated and a basic bathymetric model built with data from the literature. This model highlights the role of subsidence on overall sediment distribution. In a more detailed view, the model suggests additional parameters controlling the sediment accumulation and the depocenter position, such as depositional slope, clinoform shape or the position of the main flow. Depocenter location is generally close to this main flow, except for cases related to mass transport deposits. In addition, the sedimentation is also determined by the underfilled/overfilled accommodation of the basin, showing higher sedimentation rates in

underfilled areas where more space is available. Finally, the model suggests a possible development of carbonate platforms at the north.

References

Alexander, C.R., DeMaster, D.J., Nittrouer, C.A., (1991). Sediment accumulation in a modern epicontinental-shelf setting: The Yellow Sea. *Marine Geology*, *98*, 51–72.

Allen, P.A., Crampton S.L., Sinclair H.D. (1991). The inception and early evolution of the north alpine foreland basin, Switzerland. *Basin Research*, *3*, 143–163.

Angevine, C. L., Heller, P. L., and Paola, C. (1992). *Quantitative sedimentary basin modeling*. Universitat de Barcelona.

Arbués, P., Butillé, M., López-Blanco, M., Marzo, M., Monleón, O., Muñoz, J. A., and Serra-Kiel, J. (2011). Exploring the relationships between deepwater and shallow-marine deposits in the Aínsa piggy-back basin fill (Eocene, South- Pyrenean Foreland Basin). *Post-Meeting Field Trips Guidebook, 28th IAS Meeting*, 199–240.

Bally, A. W. (1984). *Structural styles and the evolution of sedimentary basins.* AAPG Short Course.

Barnolas, A, Larrasoaña, J.C., Pujalte, V., Schmitz, B., Sierro, F.J., Mata, M.P., van den Berg, B.C.J., Pérez-Asensio, J.N., Salazar, A., Salvany, J.M., Ledesma, S., García-Castellanos, D., Civis, J. and Cunha, P. (2019). Alpine Foreland Basins. In: Quesada and Oliveira (eds.) *The geology of Iberia: A geodynamic approach*, *4*, 7-59.

Barsó, D. (2007). *Análisis de la procedencia de los conglomerados sinorogénicos de La Pobla de Segur (Lérida) y su relación con la evolución Tectónica de los Pirineos centro-meridionales durante el Eocenomedio-Oligoceno.* PhD thesis. Universitat de Barcelona. 209 pp.

Beaumont, C., Muñoz, J.A., Hamilton, J., Fullsack, P. (2000). Factors controlling the Alpine evolution of the central Pyrenees inferred from a comparison of observations and geodynamical models. *Journal of Geophysical Research* 105: https://doi.org/10.1029/1999JB900390.

Beamud, E. (2013). *Paleomagnetism and Thermochronology in Tertiary Syntectonic Sediments of the South-Central Pyrenees : Chronostratigraphy , Kinematic and Exhumation Constraints.* PhD thesis. Universitat de Barcelona. 250 pp.

Beamud, E., Garcés, M., Cabrera, L., Muñoz, J. A., and Almar, Y. (2003). A new middle to late Eocene continental chronostratigraphy from NE Spain. *Earth and Planetary Science Letters, 216*(4), 501–514. https://doi.org/10.1016/S0012-821X(03)00539-9

Beamud, E., Muñoz, J. A., Fitgerald, P.G., Baldwin, S. L., Garcés, M., Cabrera, L., and Metcalf, J. R. (2011). Magnetostratigraphy and detrital apatite fission track thermochronology in syntectonic conglomerates: constraints on the exhumation of the South-Central Pyrenees. *Basin Research*, *23*, 309-331. https://doi.org/10.1111/j.1365-2117.2010.00492.x

Bentham, P. A. (1992). *The tectono-stratigraphic development of the western oblique ramp of the South-Central Pyrenean Thrust System, Northern Spain*. PhD thesis. University of Southern California.

Bentham, P. A., and Burbank, D. W. (1996). Chronology of Eocene foreland basin evolution along the western oblique margin of the South-Central Pyrenees. In P. F. Friend and C. J. Dabrio (Eds.), *Tertiary Basins of Spain: The Stratigraphic Record of Crustal Kinematics* (pp. 144–152). New York: Cambridge University Press.

Bentham, P. A., Burbank, D.W. and Puigdefàbregas, C. (1992). Temporal and spatial controls on the alluvial architecture of an axial drainage system: late Eocene Escanilla Formation, southern Pyrenean foreland basin, Spain. *Basin Research*, *4*, 335-352.

Bhagat, R.P. 2019. *Agglomeration of Iron Ores.* CRC Press

Boya, S. (2018). *El sistema deltaico de la Arenisca de Sabiñánigo y la continentalización de la cuenca de Jaca.* Universitat Autònoma de Barcelona PhD thesis, 207 p.

Burrel, L. (2020). Salt tectonics in the Central Southern Pyrenees: Integrated tectonostratigraphic and numerical modelling study. Universitat Autònoma de Barcelona PhD thesis, 181 p.

Butler, R.F., 1992. *Paleomagnetism: Magnetic domains to geologic terranes.* Blackwell Science Inc.

Callot, P., Odonne, F., Debroas, E. J., Maillard, A., Dhont, D., Basile, C. and Hoareau, G. (2009). Three-dimensional architecture of submarine slide surfaces and associated soft-sediment deformation in the Lutetian Sobrarbe deltaic complex (Ainsa, Spanish Pyrenees). *Sedimentology*, *56*, 1226–1249.

Cámara, P., and Klimowitz, J. (1985). Interpretación Geodinámica de la vertiente centro-occidental surpirenaica (Cuencas de Jaca - Tremp). *Estudios Geologicos*, 41, 391–404. https://doi.org/10.3989/egeol.85415-6720

Cande, S.C. and Kent, D.V. (1995). Revised calibration of the geomagnetic polarity timescale for the Late Cretaceous and Cenozoic. *Journal of geophysical research*, *100*(B4), 6093-6095.

Cant, D. J., and Stockmal, G. S. (1989). The Alberta foreland basin: relationship between stratigraphy and Cordilleran terrane-accretion events. *Canadian Journal of Earth Sciences, 26*(10), 1964–1975. https://doi.org/10.1139/e89-166

Carvajal, C. and Steel, R. (2012). Source-to-sink sediment volumes within a tectono-stratigraphic model for a Laramide shelf-to-deep-water basin: methods and results. In: Busby and Azor (eds.) *Tectonics of Sedimentary Basins: Recent Advances*. Blackwell Publishing

Castelltort, S., Guillocheau, F., Robin, C., Rouby, D., Nalpas, T., Lafont, F., Eschard, R., (2003). Fold control on the stratigraphic record: a quantified sequence stratigraphic study of the Pico

del Aguila anticline in the south-western Pyrenees (Spain). *Basin Research. 15*, 527–551. https://doi.org/10.1046/j.1365-2117.2003.00218.x.

Castelltort, S., Honegger, L., Adatte, T., Clark, J. D., Puigdefàbregas, C., Spangenberg, J. E., … Fildani, A. (2017). Detecting eustatic and tectonic signals with carbon isotopes in deep-marine strata, Eocene Ainsa Basin, Spanish Pyrenees. *Geology*, *45*(8), 707–710. https://doi.org/10.1130/G39068.1

Catuneanu, O. (2006). *Principles of Sequence Stratigraphy*. Elsevier, 386 p.

Catuneanu, O., (2017). Sequence Stratigraphy: Guidelines for a Standard Methodology. In: Michael Montenari (Ed.) *Stratigraphy & Timescales*, *2*, 2-57. Elsevier. https://doi.org/10.1016/bs.sats.2017.07.003

Coll, X., Gómez-Gras, D., Roigé, M. and Mestres, N. (2017). Heavy-mineral assemblages as a provenance indicator in the Jaca basin (Middle-Late Eocene, southern Pyrenees). *Geogaceta, 61*: 159-162

Cox, A., Doell, R.R. and Dalrymple, G.B. (1964). Reversals of the Earth's magnetic field. *Science*, *144*, 1537-1543.

Cox, A. and Hart, R.B., 1986. *Plate tectonics: How it works*. Blackwell Scientific Publications. https://doi.org/10.1177/030913338701100415

Dahle, K., Flesja, K., Talbot, M.R., and Dreyer, T. (1997), Correlation of fluvial deposits by the use of Sm-Nd isotope analysis and mapping of sedimentary architecture in the Escanilla Formation (Ainsa Basin, Spain) and the Statfjord Formation (Norwegian North Sea). *Abstracts: Sixth International Conference on Fluvial Sedimentology, Cape Town, South Africa*, p. 46.

DeCelles, P. G., and Giles, K. A. (1996). Foreland basin systems. *Basin Research*, *8*(2), 105–123. https://doi.org/10.1046/j.1365-2117.1996.01491.x

de Federico, A. (1981). *La sedimentación de talud en el sector occidental de la Cuenca Paleógena de Aínsa*. Barcelona: Universitat Autònoma de Barcelona. Publicaciones de Geología 12.

Donselaar, M. E., and Nio, S. D. (1982). An Eocene Tidal Inlet Washover Type Barrier-Island Complex in the South Pyrenean marginal Basin, Spain. *Geologie En Mijnbouw,* 343–353.

Dorobek, S. (1995). Synorogenic carbonate platforms and reefs in foreland basins: controls on stratigraphic evolution and platform/reef morphology. In: *Stratigraphic Evolution of Foreland Basins. SEPM Special Publication*, *52*, 128-147. https://doi.org/10.2110/pec.95.52.0127

Dreyer, T., Corregidor, J., Arbués, P., and Puigdefàbregas, C. (1999). Architecture of the tectonically influenced Sobrarbe deltaic complex in the Ainsa Basin, northern Spain. *Sedimentary Geology*, *127*(3–4), 127–169. https://doi.org/10.1016/S0037-0738(99)00056-1

Einsele, G. (2000). *Sedimentary Basins: Evolution, Facies, and Sediment Budget*. Springer Science & Business Media, 792 pp.

Erdos, Z.; Huismans, R.S.; van der Beek, P. (2019). Control of increased sedimentation on orogenic fold-and-thrust belt structure – insights into the evolution of the Western Alps. *Solid Earth*, *10*, 391–404. https://doi.org/10.5194/se-10-391-2019

Fernández-Bellón, O. (2004). *Reconstruction of geological structures in 3D. An example from the Southern Pyrenees*. PhD thesis. Universitat de Barcelona, 321p.

Fisher, R.A., 1924. On a distribution yielding the error functions of several well known statistics. Proceedings of the International Congress of Mathematics. Toronto 2: 805-813.

Garcés, M., 2014. Magnetostratigraphic dating. In: *Encyclopedia of Scientific Dating Methods*. Springer Science. https://doi.org/10.1007/978-94-007-6326-5_115-1

Garcés, M., López-Blanco, M., Valero, L., Beamud, E., Pueyo-Morer, E., and Rodríguez-Pintó, A. (2014). Testing orbital forcing in the Eocene deltaic sequences of the South-Pyrenean Foreland Basins. European Geosciences Union General Assembly. Viena.

Garcés, M. and Beamud, E., 2020. Geochronology: Magnetostratigraphic Dating. In: *Reference Module in Earth Systems and Environmental Sciences*. Elsevier. https://doi.org/10.1016/B978-0-12-409548-9.12386-3

Garcés, M., López-Blanco, M., Valero, L., Beamud, E., Oliva, B., Vinyoles, A., Arbués, P., Cabello, P., and Cabrera, L. (2020). Sedimentary trends, shifts and breaks across the South-Pyrenean Foreland System. *Marine and Petoleum Geology*. *113*. https://doi.org/10.1016/j.marpetgeo.2019.104105

Garrido-Mejias, A. (1968). Sobre la estratigrafia de los conglomerados de Campanué (Santa Liestra) y formaciones superiores del Eoceno (extremo occidental de la cuenca de Tremp-Graus, Pirineo Central, provincia de Huesca). *Acta Geológica Hispánica*, *3*(2), 39–43.

Ge, H., Jackson, M. P. A., and Vendeville, B.C. (1997). Kinematics and dynamics of salt tectonics driven by progradation. *AAPG Bulletin*, *81*(3), 398-423.

Glatzmaier, G.A. and Roberts, P.H., 1995. A three dimensional self-consistent computer simulation of a geomagnetic field reversal. *Nature,* 377: 203–209.

Gradstein, F. M., Ogg, J. G., Schmitz, M. D., and Ogg, G. M., 2012. *The Geological Time Scale.* Amsterdam: Elsevier.

Granjeon, D. and Joseph, P., 1999. Concepts and applications of a 3-D multiple lithology diffusive model in stratigraphic modeling. *SEPM special publication* 62

Grasseau, N. (2016). *Architecture, dynamique et modélisation sismique synthétique d'un système fluvio-deltaïque syntectonique*. PhD thesis. Université Bordeaux Montaigne, Universitat de Barcelona.

Grasseau, N., Grélaud, C., López-Blanco, M., and Razin, P. (2019). Forward seismic modeling as a guide improving detailed seismic interpretation of deltaic systems: Example of the Eocene Sobrarbe delta outcrop (South-Pyrenean foreland basin, Spain), as a reference to the analogous subsurface Albian-Cenomanian Torok-Nanushuk Delta of the Colville Basin (NPRA, USA). *Marine and Petroleum Geology*, *100*, 225–245. https://doi.org/10.1016/j.marpetgeo.2018.11.010

Hogan, P. J., and Burbank, D. W. (1996). Evolution of the Jaca piggyback basin and emergence of the External Sierra, southern Pyrenees. In P. F. Friend and C. J. Dabrio (Eds.), *Tertiary Basins of Spain: The Stratigraphic Record of Crustal Kinematics* (pp. 153–160). New York: Cambridge University Press.

Holl, J. E., and Anastasio, D. J. (1993). Paleomagnetically derived folding rates, southern Pyrenees, Spain. *Geology*, *21*, 271–274. https://doi.org/10.1130/0091-7613(1993)021<0271:PDFRSP>2.3.CO;2

Homewood, P., Allen, P. A., and Williams, G. D. (1986). Dynamics of the Molasse Basin of western Switzerland. In *Foreland Basins: International Association of Sedimentologists Special Publication 8* (pp. 199–217). https://doi.org/10.1002/9781444303810.ch10

Huyghe, D., Castelltort, S., Mouthereau, F., Serra-Kiel, J., Filleaudeau, P. Y., Emmanuel, L., Berther, B., Renard, M. (2012). Large scale facies change in the middle Eocene South-Pyrenean foreland basin: The role of tectonics and prelude to Cenozoic ice-ages. *Sedimentary Geology*, *253-254*, 25-46. https://doi.org/10.1016/j.sedgeo.2012.01.004

Johnson, N. M., and McGee, V. E. (1983). Magnetic polarity stratigraphy: Stochastic Properties of Data, Sampling Problems, and the Evaluation of Interpretations. *Journal of Geophysical Research, 88*(B2), 1213–1221. https://doi.org/10.1029/JB088iB02p01213

Kodama, K. P., Anastasio, D. J., Newton, M. L., Parés, J. M., and Hinnov, L. A. (2010). High-resolution rock magnetic cyclostratigraphy in an Eocene flysch, Spanish Pyrenees. *Geochemistry, Geophysics, Geosystems*, 11, Q0AA07. https://doi.org/10.1029/2010GC003069

Kruit, C., Brouwer, J. and Ealey, P. (1972). A deep-water sand fan in the Eocene Bay of Biscay. *Nature Phys. Sci.*, *240*, 59-61.

Kuehl, S.A., DeMaster, D.J., Nittrouer, C.A., (1986). Nature of sediment accumulation on the Amazon continental shelf. *Continental Shelf Research*, *6*, 209–336.

Labaume, P., Meresse, F., Jolivet, M., Teixell, A. and Lahfid, A. (2016). Tectonothermal history of an exhumed thrust-sheet-top basin: An example from the south Pyrenean thrust belt, *Tectonics*, *35*, 1280–1313. https://doi.org/10.1002/2016TC004192.

Labaume, P., Mutti, E. and Seguret, M. (1987). Megaturbidites: A depositional model from the Eocene of the SW-Pyrenean Foreland Basin, Spain. *Geo-Marine letters*, *7*, 91-101. https://doi.org/10.1007/BF02237988

Labaume, P. and Teixell, A. (2018). 3D structure of subsurface thrusts in the eastern Jaca Basin, southern Pyrenees. *Geologica Acta*, *14*(4), 477-498. https://doi.org/10.1344/GeologicaActa2018.16.4.9

Labourdette, R. (2011). Stratigraphy and static connectivity of braided fluvial deposits of the lower Escanilla Formation, south central Pyrenees, Spain. *AAPG Bulletin*, *95*(4), 585–617. https://doi.org/10.1306/08181009203

Lide, DR (ed.). CRC Handbook of Chemistry and Physics. 81st Edition. CRC Press LLC, Boca Raton: FL 2000, p. 4-66

Maesano, F.E.; D'Ambrogi, C. (2015). Coupling sedimentation and tectonic control: Pleistocene evolution of the central Po Basin. *Italian journal of Geosciences*, *135*(3), 394-407. https://doi.org/10.3301/IJG.2015.17

Mangin, J. P. (1959-60). Le Nummulitique sud-Pyrénéen à l'Ouest de l'Aragon. *Pirineos*, 51–58, 1–631.

Martinsen, O.J., Sømme, T.O., Thurmond, J.B., Helland-Hansen, W. and Lunt, I. (2010). Source-to-sink systems on passive margins: theory and practice with an example from the Norwegian continental margin. In: Vining and Pickering (eds) *Petroleum geology: from mature basins to new frontiers.* 913-920. https://doi.org/10.1144/0070913.

Mateu-Vicens, G., Pomar, L. and Ferràndez-Cañadell, C. (2012). Nummulitic banks in the upper Lutetian 'Buil level', Ainsa Basin, South Central Pyrenean Zone: the impact of internal waves. *Sedimentology*, *59*, 527-552. https://doi.org/10.1111/j.1365-3091.2011.01263.x

McIntosh, R.P. (2009a). Apparatus for researches in mountain structure. Pencil side view. *Henry Mowbray Cadell archives, BGS*, P612780

McIntosh, R.P. (2009b). Experimental Researches in Mountain Structure. Notebook recording the results of H.M. Cadell's famous mountain building experiments*. Henry Mowbray Cadell archives, BGS*, P612832

Merrill, R.T., McElhinny, M.W. and McFadden, P.L., 1998. *The magnetic field of the earth: paleomagnetism, the core, and the deep mantle*. Academic Press.

Miall, A. D. (1995). Collision-Related Foreland Basins. In: Busby, C. J. and Ingersoll, R. V. (eds.), *Tectonics of Sedimentary Basins*. Blackwell Science. 393–424.

Michael, N.A., Whittaker, A.C., Carter, A. and Allen, P.A. (2014). Volumetric budget and grain-size fractionation of a geological sediment routing system: Eocene Escanilla Formation, south-central Pyrenees. *GSA Bulletin*, *126*(3/4), 585-599. https://doi.org/10.1130/B30954.1

Millan, H., Aurell, M., and Melendez, A. (1994). Synchronous detachment folds and coeval sedimentation in the Prepyrenean External Sierras (Spain): a case study for a tectonic origin of sequences and systems tracts. *Sedimentology*, *41*(5), 1001–1024. https://doi.org/10.1111/j.1365-3091.1994.tb01437.x

Mochales, T., Barnolas, A., Pueyo, E. L., Serra-Kiel, J., Casas, A. M., Samsó, J. M., … Sanjuán, J. (2012). Chronostratigraphy of the Boltaña anticline and the Ainsa Basin (southern Pyrenees). *GSA Bulletin*, *124*(7–8), 1229–1250. https://doi.org/10.1130/B30418.1

Mochales, T., Pueyo, E.L., Casas, A.M. and Barnolas, A. (2016). Restoring paleomagnetic data in complex superposed folding settings: The Boltaña anticline (Southern Pyrenees). *Tectonophysics*, *671*, 281-298. https://doi.org/10.1016/j.tecto.2016.01.008

Montes, M. J. (2009). Estratigrafía del Eoceno-Oligoceno de la Cuenca de Jaca. Sinclinorio del Guarga. *Coleccion de Estudios Altoaragoneses*, *59*, 1-355.

Moody, J. D., Pyles, D. R., Clark, J. D., and Bouroullec, R. (2012). Quantitative outcrop characterization of an analog to weakly confined submarine channel systems: Morillo 1 member, Ainsa Basin, Spain. *AAPG Bulletin*, *96*(10), 1813–1841. https://doi.org/10.1306/01061211072

Moss, J. (2005). *Tectonic controls on Eocene deltaic architecture, Jaca basin, Spanish Pyrenees*. PhD. Durham University. 351pp.

Muller, R.A., 2002. Avalanches at the core-mantle boundary. *Geophysical Research Letters*. 29(19):1935. https://doi.org/10.1029/2002GL015938

Muñoz, J. A., Beamud, E., Fernández, O., Arbués, P., Dinarès-Turell, J., and Poblet, J. (2013). The Ainsa Fold and thrust oblique zone of the central Pyrenees: Kinematics of a curved contractional system from paleomagnetic and structural data. *Tectonics*, *32*(5), 1142–1175. https://doi.org/10.1002/tect.20070

Muñoz, J.A., Mencos, J., Roca, E., Carrera, N., Gratacós, O., Ferrer, O. and Fernández, O. (2018). The structure of the South-Central-Pyrenean fold and thrust belt as constrained by subsurface data. *Geologica Acta*, *16*(4), 439–460. https://doi.org/10.1344/GeologicaActa2018.16.4.7

Mutti, E. (1992). *Turbidite sandstones*. AGIP / Instituto di Geologia, Università di Parma. 275 p.

Mutti, E., Luterbacher, H. P., Ferrer, J., and Rossell, J. (1972). Schema stratigrafico e lineamenti di facies del Paleogene marino della zona centrale sudpirenaica tra Tremp (Catalogna) e Pamplona (Navarra). *Mem. Soc. Geol. Ital*., *11*(3), 391–416.

Mutti, E. and Normark, W.R. (1987). Comparing examples of modern and ancient turbidite systems: problems and concepts. In: Legget, J.R. and Zuffa, G.G. (eds.). *Marine Clastic Sedimentology: Concepts And Case Studies*. G. Graham and Trotman, London, 1-37.

Mutti, E. and Normark, W.R. (1991). An integrated approach to the study of turbidite systems. In: Weimer, P. and Link, H. (eds.), *Seismic Facies And Sedimentary Processes Of Submarine Fans And Turbidite Systems.* Springer, New York, 75-106.

Mutti, E., Remacha, E., Sgavetti, M., Rosell, J., Valloni, R. and Zamorano, M. (1985). Stratigraphy and facies characteristics of the Eocene Hecho Group turbidite systems, south-central Pyrenees. In: Milà, M. D. and Rosell, J., eds., 6th *European IAS Regional Meeting Excursion Guidebook: Lleida, Institut d'Estudis Ilerdencs*. 519–576.

Nijman, W., and Nio, S. D. (1975). The Eocene Montañana delta. In: Rosell, J.and Puigdefàbregas, C. (eds.), *Sedimentary evolution of the Paleogene South Pyrenean Basin. IAS 9th International Congress*. Nice.

Odonne, F., Callot, P., Debroas, E.-J., Sempere, T., Hoareau, G., and Maillard, A. (2011). Soft-sediment deformation from submarine sliding: Favourable conditions and triggering mechanisms in examples from the Eocene Sobrarbe delta (Ainsa, Spanish Pyrenees) and the mid-Cretaceous Ayabacas Formation (Andes of Peru). *Sedimentary Geology*, *235*(3–4), 234–248. https://doi.org/10.1016/j.sedgeo.2010.09.013

Oms, O., Dinarès-Turell, J., and Remacha, E. (2003). Magnetic stratigraphy from deep clastic turbidites: An example from the Eocene Hecho group (Southern Pyrenees). *Studia Geophysica et Geodaetica*, 47(2), 275–288. https://doi.org/10.1023/A:1023719607521

Ortiz, A., Guillocheau, F., Lasseur, E., Briais, J., Robin, C., Serrano, O., and Fillon, C. (2020). Sediment routing system and sink preservation during the post-orogenic evolution of a retro-foreland basin: The case example of the North Pyrenean (Aquitaine, Bay of Biscay) Basins. *Marine and Petroleum Geology*, *112*, 104085. https://doi.org/10.1016/j.marpetgeo.2019.104085

Patruno, S. and Helland-Hansen, W. (2018). Clinoforms and clinoform systems: Review and dynamic classification scheme for shorelines, subaqueous deltas, shelf edges and continental margins. *Earth-Science Reviews*, *185*, 202–233.

Patton, T. L. and O'Connor, S. J. (1988). Cretaceous flexural history of northern Oman Mountain foredeep, United Arab Emirates. *AAPG Bulletin*, *72*(7), 797-807.

Pickering, K. T., and Corregidor, J. (2005). Mass-Transport Complexes (MTCs) and Tectonic Control on Basin-Floor Submarine Fans, Middle Eocene, South Spanish Pyrenees. *Journal of Sedimentary Research*, *75*, 761–783. https://doi.org/10.2110/jsr.2005.062

Poblet, J. and Hardy, S. (1995). Reverse modelling of detachment folds; application to the Pico del Aguila anticline in the South Central Pyrenees (Spain). *Journal of Structural Geology*, *17*, 1707–1724.

Poblet, J., Muñoz, J.A., Travé, A and Serra-Kiel, J. (1998). Quantifying the kinematics of detachment folds using three-dimensional geometry: Application to the Mediano anticline (Pyrenees, Spain). *Geological Society of America Bulletin*, *110*, 111-125. https://doi.org/10.1130/0016-7606(1998)110<0111:QTKODF>2.3.CO;2

Puigdefàbregas, C. (1975). *La sedimentación molásica en la cuenca de Jaca. Monografías del Instituto de Estudios Pirenaicos*, 104. PhD thesis. Universitat de Barcelona. 188 pp.

Puigdefàbregas, C., Muñoz, J. A., and Verges, J. (1992). Trusting and foreland basin evolution in the southern Pyrenees. In: M. K. R. (ed.), *Thrust Tectonics*. Dordrecht: Springer. 247–254. https://doi.org/10.1007/978-94-011-3066-0_22

Remacha, E., Arbués, P., and Carreras, M. (1987). Precisiones sobre los limites de la secuencia deposicional de Jaca. Evolución de las facies desde la base de la secuencia hasta el techo de la arenisca de Sabiñánigo. *Boletin Geologico y Minero*, *98*, 40-48.

Rodríguez-Pintó, A., Pueyo, E. L., Barnolas, A., Samsó, J. M., Pocoví, A., Gil-Peña, I., … Serra-Kiel, J. (2012a). Lutetian magnetostratigraphy in the Santa Marina section (Balzes anticline, Southwestern Pyrenees). *Geo-Temas*, 13, 1184–1187.

Rodríguez-Pintó, A., Pueyo, E. L., Serra-Kiel, J., Barnolas, A., Samsó, J. M., and Pocoví, A. (2013). The Upper Ypresian and Lutetian in San Pelegrín section (Southwestern Pyrenean Basin): Magnetostratigraphy and larger foraminifera correlation. *Palaeogeography, Palaeoclimatology, Palaeoecology*, 370, 13-29. https://doi.org/10.1016/j.palaeo.2012.10.029

Rodríguez-Pintó, A., Pueyo, E. L., Serra-Kiel, J., Samsó, J. M., Barnolas, A., and Pocoví, A. (2012b). Lutetian magnetostratigraphic calibration of larger foraminifera zonation (SBZ) in the Southern Pyrenees : The Isuela section. *Palaeogeography, Palaeoclimatology, Palaeoecology*, 333–334, 107–120. https://doi.org/10.1016/j.palaeo.2012.03.012

Rodríguez-Pintó, A., Pueyo, E., Calvín, P., Sánchez, E., Ramajo, J., Casas, A., Ramón, M., and Pocoví, A. (2016). Rotational kinematics of a curved fold: The Balzes anticline (Southern Pyrenees). *Tectonophysics*, *677–678*, 171–189. https://doi.org/10.1016/j.tecto.2016.02.049

Rodríguez-Salgado, P.; Falivene, O.; Frascati, A.; Arbués, P.; Monleon, O.; Butille, M.; Cabello, P.; Lopez-Blanco, M.; Poppelreiter, M.C. (2020). Stratigraphic forward models of the Sobrarbe Deltaic Complex (Ainsa Basin, NE Spain): controls on stratigraphic architecture. In: Grotsch, J. (ed.), *EAGE Special Volume on Digital Geology*, 71-90.

Roigé, M., Gómez-Gras, D., Remacha, E., Daza, R., and Boya, S. (2016). Tectonic control on sediment sources in the Jaca basin (Middle and Upper Eocene of the South-Central

Pyrenees). *Comptes Rendus Geoscience, 348*(3–4), 236–245. https://doi.org/10.1016/j.crte.2015.10.005

Roigé, M. (2018). *Procedència i evolució dels sistemes sedimentaris de la conca de Jaca (conca d'avantpaís Sudpirinenca): Interacció entre diverses àrees font en un context tectònic actiu.* Universitat Autònoma de Barcelona PhD thesis. 315p.

Romans, B. W., Castelltort, S., Covault, J. A., Fildani, A., and Walsh, J. P. (2016). Environmental signal propagation in sedimentary systems across timescales. *Earth-Science Reviews*, *153*, 7–29. https://doi.org/10.1016/j.earscirev.2015.07.012

Ross, W.C., Halliwell, B.A., May, J.A., Watts, D.E. and Syvitsky. (1994). Slope readjustment: A new model for the development of submarine fans and aprons. *Geology*, *22*, 511-514.

Santolaria, P., Casas-Sainz, A.M., Soto, R. and Casas, A., (2016). Gravity modelling to assess salt tectonics in the western end of the South Pyrenean Central Unit. *Journal of the Geological Society*, *174*, 269–288. https://doi.org/10.1144/jgs2016-027

Schumm, S.A. (1977). *The fluvial system*. Wiley. New York

Seguret, M. (1972). *Étude tectonique des nappes et séries décollées de la partie centrale du versant sud des Pyrénées – caractère synsédimentaire, rôle de la compression et de la gravité* (Série géol). Montpellier: Publication de l'U.S.T.L.: Serie Géologie Structurale.

Silva-Casal, R. (2017). *Las plataformas carbonatadas del Eoceno medio de la cuenca de Jaca-Pamplona (Formación Guara, Sierras Exteriores): análisis estratigráfico integral y evolución sedimentaria*. Universidad de Zaragoza PhD thesis. 345 p.

Soler-Sampere, M., and Puigdefàbregas, C. (1970). Líneas generales de la geología del Alto Aragón Occidental. *Pirineos*, 96, 5–19.

Sømme, T.O., Helland-Hansen, W., Martinsen, O.J. and Thurmond, J.B. (2009). Relationships between morphological and sedimentological parameters in source-to-sink systems: a basis for predicting semi-quantitative characteristics in subsurface systems. *Basin Research*, *21*: 361-387. https://doi.org/10.1111/j.1365-2117.2009.00397.x

Soto, R., Casas, A. M., Sorti, F. and Faccenna, C. (2002). Role of lateral thickness variations on the development of oblique structures at the western end of the South Pyrenean Central Unit. *Tectonophysics*, *350*, 215–235.

Tauxe, L. (1998). *Paleomagnetic principles and practice*. Kluwer Academic

Tauxe, L. and Gallet, Y. (1991). A jackknive for magnetostratigraphy. *Geophysical research letters*, 18(9), 1783-1786.

Teixell, A. and Muñoz, J.A. (2000). Evolución tectono-sediementaria Pirineo meridional durante el terciario: Una síntesis basada en la transversal del río Noguera Ribagorçana. *Revista de la Sociedad Geológica de España*, *13*(2), 251–264.

Vacherat, A., Mouthereay, F., Pik, R., Huyghe, D., Paquette, J.L., Christophoul, F., Loget, N. and Tibari, B. (2017). Rift-to-collision sediment routing in the Pyrenees: A synthesis from sedimentological, geochronological and kinematic constrains. *Earth-Science Rev.*, *172*, 43-74. https://doi.org/10.1016/j.earscirev.2017.07.004

Valero, L., Vinyoles, A., López-Blanco, M., Beamud, E., Pueyo-Morer, E., Rodríguez-Pintó, A., Castelltort, S. and Garcés, M. (in prep.) Orbital origin of the stratigraphic sequences in South-Pyrenean syn-kinematic sediments.

van Lunsen, H. A. (1970). *Geology of the Ara-Cinca region, Spanish Pyrenees, Province of Huesca*. Utrecht State University.

Vidal-Royo, O., Cardozo, N., Muñoz, J.A., Hardy, S. and Maerten, L. (2011). Multiple mechanism driving detachment folding as deduced from 3D reconstruction and geomechanical restoration: the Pico del Águila anticline (External Sierras, Southern Pyrenees). *Basin Research*, 23:1-19. https://doi.org/10.1111/j.1365-2117.2011.00525.x

Vincent, S. (2001) The Sis palaeovalley: a record of proximal fuvial sedimentation and drainage basin development in response to Pyrenean mountain building. *Sedimentology*, *48*, 1235-1276.

Vinyoles, A., López-Blanco, M., Garcés, M., Arbués, P., Valero, L., Beamud, E., Oliva-Urcia, B. and Cabello, P. (2020), 10 Myr evolution of sedimentation rates in a deep marine to non-marine foreland basin system: tectonic and sedimentary controls (Eocene, Tremp-Jaca Basin, Southern Pyrenees, NE Spain). *Basin Research* Accepted Author Manuscript. https://doi.org/10.1111/bre.12481

Walsh, J.P., Nittrouer, C.A., Palinkas, C.M., Ogston, A.S., Sternberg, R.W. and Brunskill, G.J. (2004). Clinoform mechanics in the Gulf of Papua, New Guinea. *Continental Shelf Research*, *24*, 2487–2510.

Wuellner, D.E., Lehtonen, L.R., James, W.C. (1986). Sedimentary-tectonic development of the Marathon and Val Verde basins, West Texas, USA: a Permo-Carboniferous migrating foredeep. In: Allen P.A., Homewood, P. (Eds*.) Foreland Basins. IAS Special Publication*, *8*, 347-368.

Zijderveld, J.D.A., 1967. AC demagnetization of rocks: Analysis of results. In: Collinson, Creer and Runcorn (eds.) *Methods in Paleomagnetism*, 254–286.

Zoetemeijer, R., Desegaulx, P., Cloetingh, S., Roure, F., and Moretti, I. (1990). Lithospheric Dynamics and Tectonic-Stratigraphic Evolution of the Ebro Basin*. Journal of Geophysical Research*, *95* (B3), 2701–2711. https://doi.org/10.1029/JB095iB03p02701